

THESIS FOR THE DEGREE OF DOCTOR OF PHILOSOPHY

---

# Functional polymer brush coatings for nanoscale devices

JOHN ANDERSSON

Department of Chemistry and Chemical Engineering  
Division of Applied chemistry  
CHALMERS UNIVERSITY OF TECHNOLOGY  
Gothenburg, Sweden, 2022

# Functional polymer brush coatings for nanoscale devices

JOHN ANDERSSON

Copyright © 2022 JOHN ANDERSSON

Doktorsavhandlingar vid Chalmers tekniska högskola

Ny serie: 5213

ISSN 0346-718X

ISBN 978-91-7905-747-3

Department of Chemistry and Chemical Engineering

Chalmers University of Technology

SE-412 96 Gothenburg, Sweden

Phone: +46 (0)31 772 1000

[www.chalmers.se](http://www.chalmers.se)

Cover image: Artistic representation of a biofunctional polymer brush coated nanopore array with active gating of biomolecules.

Printed by Chalmers Digitaltryck

Gothenburg, Sweden, November 2022

# Functional polymer brush coatings for nanoscale devices

JOHN ANDERSSON

Chemistry and Chemical Engineering

Chalmers University of Technology

---

## Abstract

Nanobiotechnology is an interdisciplinary field that has garnered considerable attention for offering exciting new opportunities of studying and manipulating biomolecules at the nanoscale. This prospect bears large potential benefits in the field of medicine and the whole life science sector in general. Fabrication of different nanostructure devices that can handle liquids at the scale of biomolecules, such as nanochannels or nanopores, provide a good basis within nanobiotechnology. However, the materials of nanostructures tend to not interact with complex biomolecules in ways that are sufficiently specific or controlled. This issue can be avoided by functionalising the surface of nanostructures with different organic coatings, and polymer brushes have shown a diverse range of functionality in this regard. This thesis summarises efforts towards designing functional polymer brush coatings for nanoscale devices. Surface sensitive techniques are used to characterise the grafting of dense poly(ethylene glycol) brushes to various noble metals and silicon dioxide. The new functionalisation protocol for polymer brushes on silicon dioxide provides excellent biofunctionality and is demonstrated to be compatible with two different nanostructures. The specific hydrogen-bond mediated interaction between a poly(ethylene glycol) brush and poly(methacrylic acid) in solution at low pH is shown to make the polymer brush reversibly stimuli-responsive. Preliminary results further demonstrate how this interaction can be controlled electrochemically and indicates its suitability as a macromolecular gating mechanism for nanosized openings. Finally, characterisation and fabrication of plasmonic nanopore arrays with separately functionalisable compartments using electron beam lithography techniques is presented.

**Keywords:** Nanobiotechnology, polymer brush, poly(ethylene glycol), pH responsive, silatranes, interpolymer complex, electrochemistry, nanopores, functional materials, macromolecular gating.



# List of Publications

This thesis is based on the following appended papers and manuscripts:

## Paper 1:

*Surface plasmon resonance sensing with thin films of palladium and platinum – quantitative and real-time analysis*

**John Andersson**, Justas Svirelis, Gustav Ferrand-Drake del Castillo, Takumi Sannomiya, and Andreas Dahlin  
Physical Chemistry Chemical Physics, 2022, 24, 4588-4594.

## Paper 2:

*Polymer Brushes on Silica Nanostructures Prepared by Aminopropylsilatrane Click Chemistry: Superior Antifouling and Biofunctionality*

**John Andersson**, Julia Järlebark, Sriram Kesarimangalam, Andreas Schaefer, Rebekah Hailes, Chonnipa Palasingh, Chun-Jen Huang, Fredrik Westerlund, and Andreas Dahlin  
Manuscript in writing

## Paper 3:

*Control of polymer brush morphology, rheology and protein repulsion by hydrogen bond complexation*

**John Andersson**, Gustav Ferrand-Drake del Castillo, Pierluigi Bilotto, Fredrik Höök, and Andreas Dahlin  
Langmuir, 2021, 37, 16, 4943–4952.

## Paper 4:

*Optical properties of plasmonic nanopore arrays prepared by electron beam and colloidal lithography*

Bitu Malekian, Kunli Xiong, Evan S. H. Kang, **John Andersson**, Gustav Emilsson, Marcus Rommel, Takumi Sannomiya, Magnus P. Jonsson, and Andreas Dahlin  
Nanoscale Advances, 2019, 1, 4282-4289

## **Contribution report**

### **Paper 1:**

Performed SPR measurements on Pd and developed the analysis method. Co-authored the manuscript.

### **Paper 2:**

Performed the SPR, QCM-D and contact angle experiments and analysis. Prepared samples for XPS measurements. Participated in AFM measurements and analysed the results. Prepared solutions and guided experiments in the microfluidic nanochannel device and performed the image analysis. Wrote a first draft of the manuscript and co-authored the final version.

### **Paper 3:**

Performed all experiments and analysis, except for: sample preparations, measurements and analysis of the SFA experiment. Co-authored the manuscript.

### **Paper 4:**

Performed part of the nanopore membrane fabrication and development (photolithography, KOH etching, e-beam resist coating and lift-off). Continued development post-publication for all involved steps.

## Papers not included in this thesis

*Enzyme-free optical DNA mapping of the human genome using competitive binding*  
Vilhelm Müller, Albertas Dvirnas, **John Andersson**, Vandana Singh, Sriram KK, Pegah Johansson, Yuval Ebenstein, Tobias Ambjörnsson and Fredrik Westerlund  
Nucleic Acids Research, 2019, 47, 15, 89

*Tuning the Thermoresponsive Behavior of Surface-Attached PNIPAM Networks: Varying the Crosslinker Content in SI-ATRP*  
Sophia Thiele, **John Andersson**, Andreas Dahlin, and Rebekah L. N. Hailes  
Langmuir, 2021, 37, 11, 3391–3398

*A designer FG-Nup that reconstitutes the selective transport barrier of the nuclear pore complex*  
Alessio Fragasso, Hendrik W. de Vries, **John Andersson**, Eli O. van der Sluis, Erik van der Giessen, Andreas Dahlin, Patrick R. Onck, and Cees Dekker  
Nature Communications, 2021, 12, 2010

*Simultaneous, Single-Particle Measurements of Size and Loading Give Insights into the Structure of Drug-Delivery Nanoparticles*  
Albert Kamanzi, Yifei Gu, Radin Tahvildari, Zachary Friedenberger, Xingqi Zhu, Romain Berti, Marty Kurylowicz, Dominik Witzigmann, Jayesh A. Kulkarni, Jerry Leung, **John Andersson**, Andreas Dahlin, Fredrik Höök, Mark Sutton, Pieter R. Cullis, and Sabrina Leslie  
ACS Nano, 2021, 15, 12, 19244–19255

*Accurate Correction of the “Bulk Response” in Surface Plasmon Resonance Sensing Provides New Insights on Interactions Involving Lysozyme and Poly(ethylene glycol)*  
Justas Svirelis, **John Andersson**, Anna Stradner, and Andreas Dahlin  
ACS Sensors, 2022, 7, 4, 1175–1182

*Transport receptor occupancy in nuclear pore complex mimics*  
Alessio Fragasso, Hendrik W. de Vries, **John Andersson**, Eli O. van der Sluis, Erik van der Giessen, Patrick R. Onck, and Cees Dekker  
Nano Research, 2022

*Pore performance: artificial nanoscale constructs that mimic the biomolecular transport of the nuclear pore complex*

**John Andersson**, Justas Svirelis, Jesper Medin, Julia Järlebark, Rebekah Hailes, and Andreas Dahlin

Nanoscale advances, 2022

*Stable Trapping of Multiple Proteins at Physiological Conditions Using Nanoscale Chambers with Macromolecular Gates*

Justas Svirelis, Zeynep Adali, Gustav Emilsson, **John Andersson**, Jesper Medin, Radhika Vattikunta, Krzysztof Kolman, Oliver Olsson, Yusuke Sakiyama, Roderick Y. H. Lim, and Andreas Dahlin

Manuscript to be submitted





---

## Preface

---

What makes something alive? Despite our intuitive feeling for identifying the living from the dead, when trying to get to the bottom of this question we tend to find that a good answer eludes us. However, from observations of all kinds of living beings and biological systems, we generally seem to find that they are inherently complex. The complexity of biological processes can even be observed at many different length scales, and interestingly, there may be an emergent pattern to it if viewed from a broader perspective.

On a macroscopic scale, we find living beings capable of acting independently as individuals, while similarities in the behaviour and physical restraints for certain groups of individuals result in what we refer to as species. In turn, the general trends and interplay between different species make up complex biological ecosystems, which themselves evolve over large time periods. We also understand that these ecosystems often are fragile, because they can come crashing down like the tower in a game of Jenga if too many critical blocks (or species in this case) that support it are removed. Foreseeing exactly which removed species will be the final straw and what (or "who") may cause it to disappear is also incredible hard to predict. Thus, before we know more about all the components that make up an ecosystem and how they may interact, the safest strategy to avoid causing its catastrophic collapse is simply to not "play the game" and avoid interfering with it as much as possible. Thus, the death of an ecosystem in many ways play out in a similar fashion to the death of living beings after suffering irreparable damage to critical organs.

Zooming in on the world around us using microscopes has allowed us to opened our eyes to the microscopic realm and discovered that it is filled with biological activity. We could now see that, if you look very closely, there are entirely new types of microscopic organisms living right under our noses (not only figuratively), and in fact, we are ourselves nothing more but collections of microscopic *cells*. Our cells are capable of performing actions and often navigate around in their environment as individuals. Most of the time however, they work together with each other and with friendly microorganisms in symbiosis to provide and protect a mutually beneficial environment in which they may prosper and proliferate. Essentially, we "macroorganisms" are all ecosystems in the perspective of a cell in the microscopic world, and just like a macroscopic biological ecosystem we need to be properly maintained, or we die. However, our cells are not the smallest biological components. In a very similar way to

our different parts, our organs, so do cells have tiny *organelles* that provide them with all the functions they need to stay alive. Now we are left with the obvious question: What about the organelles, what are they made of?

Unfortunately, we have now reached the end of what can be seen with a conventional microscope and instead entered the confusing realm of nanoscience. At the nanoscale, things starts to blur a bit, as we are getting close to the unimaginably small atoms and molecules that make up all the matter in the universe, both "living" and dead. While we can still often recognise familiar patterns and behaviours in the slightly larger nanosized objects, they sometimes also inherit the strange and unfamiliar quantum properties of atoms and molecules. At the nanoscale we find a collection of particular types of polymeric *biomolecules*, such as DNA, RNA and proteins. These biomolecules are themselves made up from seemingly dead ordinary matter like carbon, nitrogen, oxygen and some other elements, but that somehow come together in an emergent chemistry forming all the necessary components that make something come to life. Exactly how this works is still up to speculation at this point, but the underlying principle is clearly complex, similarly to what we have seen in the ecosystems of the biological macro- and microscales.

If we analyse some of these biomolecules further – focusing on proteins in particular – we get a further sense of where the complexity at the nanoscale comes from. Proteins make up some of the structural materials of cells, serve as building blocks for biological machines that perform highly specific tasks, catalyse various biochemical reactions and processes, and carry signals and messages between different cells. All of this functionality originates from the three-dimensional structure of the proteins and their characteristic distribution of different biochemical "residues" containing various functional chemical groups. The protein structure is determined from 20 individual molecular building blocks, *amino acids*, connected in specific sequences into long polymeric chains. The sequence of amino acids dictate how a protein folds into its characteristic three dimensional shape in a given environment, which in turn determines what physical and chemical properties it will obtain. As of writing, there are currently more than 227 M unique protein sequence entries in the UniProt database[1] (which increased by roughly 30 M in the last 2 years). These are isolated from many different organisms, out of which less than 0.1 % have an experimentally determined three-dimensional structure[2].

Already now the reader could imagine that all of this complexity and indicative lack of information make it difficult to figure out how it all ultimately comes together into cells and microorganisms. However, as if this was not enough, a proteins structure is generally influenced by external factors and the surrounding environment. Furthermore, when performing their functions they may even dynamically change their structure temporarily. Essentially, individual proteins can occupy different *states* at different energy levels, that dynamically affect their structure, function and behaviour (as if the protein is in a certain "mood"). Conventional methods of studying proteins mainly observe them in their most common low energy ground state (when they sit and do nothing), but there is an increasing need for new methods that can study proteins in their less common and short-lived excited states. Some evidence even suggest such higher energy states are related to many proteins' function[3]. For the same reason, an increasing number of researchers now also turn their attention towards *single-molecule studies* to be able to resolve individual proteins in their different dynamic intermediary states, rare sub-populations and varying reaction pathways[4]. Indeed, the importance of understanding the behaviour of biomolecules at the nanoscale is highlighted by the negative effects they have on organisms even up to the macroscopic scale when they "misbehave", i.e. where dysfunctional proteins often lead to serious diseases[5], [6].

Interestingly, we seem to find an almost fractally repeating pattern of complexity in biological processes at any length scale we turn to. Biomolecule behaviour at the nanoscale essentially reflect the complex organisation of macro- and microscale ecosystems from individuals to their group behaviour, making all three scales seemingly interconnected. It is my belief that if we want to understand biological life and what it really means to be alive on a fundamental scientific level, we need to keep a wide and open perspective on what these concepts might entail and make sure to consider all their related avenues. While we are still very far from a complete picture on biological processes at the macro- and microscale, it is clear that we need to push our understanding further about the elemental biological components at the nanoscale to fully answer such big questions. However, to be able to do so we are in need of new advanced technological developments. This thesis work dips into the realm of nanoscience and present some technological developments that may eventually contribute to our understanding of biomolecules on the smallest of scales.

By combining surface coatings and nanostructures in the right way, parts of the foundation for new tools and methodologies of interacting with nanosized biomolecules are laid. Ultimately, this has the potential to contribute to fundamental biological knowledge and open up new possibilities for novel medical applications along the way.

## **Acknowledgements**

I would like to thank my supervisor, Andreas, for all his support and for letting me loose in the world of academia. I have learned great things and many new skills that I will always keep with me. I would also like to thank all the great colleagues of my group and at the division for helpful discussions, great lunches and the fun times in and out of the lab! My thanks also to all collaborators at other departments here at Chalmers and over in Vienna and Delft. Thank you to all friends and family for the great support, as well as my cats Stina and Siri for their fluffy distractions. And last, but not least, thank you Linnea for making me a greater person with all your good advice and love!

All the best,  
John, November 2022, Sandsbacka



---

# Contents

---

<b>Abstract</b>	<b>i</b>
<b>List of Papers</b>	<b>iii</b>
Contribution report . . . . .	iv
Papers not included in this thesis . . . . .	v
<b>Preface</b>	<b>xiii</b>
Acknowledgements . . . . .	xiii
<b>1 Introduction</b>	<b>1</b>
<b>2 Background</b>	<b>9</b>
2.1 Polymers in solution . . . . .	10
2.2 Surface grafted polymers and polymer brushes . . . . .	12
2.2.1 Grafting strategies . . . . .	14
2.3 Poly(ethylene glycol) (PEG) . . . . .	15
2.4 Poly(methacrylic acid) (PMAA) . . . . .	16
2.5 Hydrogen-bonded interpolymer complexation . . . . .	19

2.6	Electrochemistry . . . . .	20
2.6.1	Electrochemistry in nanoscience . . . . .	21
<b>3</b>	<b>Characterisation techniques</b>	<b>23</b>
3.1	Surface plasmon resonance . . . . .	24
3.1.1	Quantitative interpretation of the SPR response . . . . .	28
3.1.2	Fresnel modelling of SPR measurements . . . . .	29
3.1.3	Non-interacting probe method . . . . .	34
3.2	Quartz crystal microbalance with dissipation monitoring . . . . .	38
3.2.1	Voigt model for viscoelastic layers . . . . .	41
3.3	Extinction spectroscopy of plasmonic nanoholes . . . . .	44
<b>4</b>	<b>Functional surface coatings</b>	<b>49</b>
4.1	Surface cleaning and preparation . . . . .	50
4.2	Coating noble metals . . . . .	51
4.2.1	SPR characterisation of palladium and platinum coatings	52
4.2.2	PEG brushes on palladium and platinum . . . . .	53
4.3	Coating silicon dioxide . . . . .	54
4.3.1	Surface amination using 3-aminopropylsilatrane . . . . .	55
4.3.2	PEG brushes on silicon dioxide . . . . .	58
4.4	The pH responsive PEG-PMAA system . . . . .	65
4.5	Unpublished work: Electrochemically controlled PEG brush ac- tuation . . . . .	69
<b>5</b>	<b>Nanobiotechnological devices</b>	<b>77</b>
5.1	Plasmonic nanopore arrays . . . . .	78
5.2	Functionalisation of nanostructures . . . . .	82
5.2.1	PEG grafting to nanochannels and nanopores . . . . .	82
5.2.2	Unpublished work: Macromolecular gating with PEG- PMAA interactions . . . . .	87
<b>6</b>	<b>Concluding remarks and future outlook</b>	<b>91</b>
	<b>References</b>	<b>95</b>



# CHAPTER 1

---

Introduction

---

The interdisciplinary field of nanobiotechnology – where designs of physical nanosized objects, structures and materials made using nanotechnology are applied to the world of molecular biology – is gathering a lot of interest because of its promise to produce tools that interact with biomolecules at their own size scale[1] and its high potential for novel medical applications[2], [3]. One reason that makes nanobiotechnology particularly interesting for the life science sector is related to the great amount of potential that comes with miniaturisation. The drive towards miniaturisation of electronics (specifically the transistor) using micro- and nanofabrication techniques, resulted in an unimaginable wealth of technological development that have completely reshaped much of modern civilisation and still continues to this day. Computers that used to take up a full room and required expert technicians to operate now fit in your pocket, offer several orders of magnitude better performance and is capable of things nobody could ever imagine at the time computers were initially developed. Effective miniaturisation of conventional biolab bench-scale processes could increase their turn-over rates and automation potential and allow us to create novel medical devices. Such devices could perform automated diagnostics, drug development and personalised treatment with minimal input and costs, while also providing faster and more reliable results[2], [4], [5].

The miniaturisation of lab processes is often referred to as "lab-on-a-chip", which is a technology based in the field of *microfluidics* – the manipulation of liquids in microscopic channels and reservoirs connected together as a network and able to perform various operations on an injected sample. The nature of this small size scale raise the need to reinvent components that perform functions equivalent to more familiar macroscopic machines, simply because the same working principles of such components cannot be applied. Some examples of common types of microfluidic components include: mixers, separators, reactors, detectors, and more[6]. However, new kind of information can be accessed and utilised because of the additional size dependent properties that emerge. Two examples are the predominantly laminar flow properties of fluids flowing in narrow microchannels that offer precise control of solvents and their solutes[5], and the increased surface-to-volume ratio can be utilised to make use of otherwise weak interactions and effects to a larger degree. Lab-on-a-chip devices based solely on microfluidics can be used in the miniaturisation of conventional biomolecule ensemble studies. Still, only through integrating additional nanobiotechnologies will we be able to access more detailed

---

and important information for the manipulation and behaviour of individual biomolecules at the nanoscale[4]. This also means we again should expect the need to find new design principles for components relevant for *nanofluidics* and how these are to be integrated with powerful optoelectronic measurement techniques and lab-on-a-chip devices.

To produce new tools needed for gaining access to novel biomolecular insights we need to turn to nanotechnology. There are essentially two design approaches to produce nanomaterials, nanoobjects and nanostructures; the top-down approach starting from bulky materials where deposition, lithography and etching are used to give the material nanoscale properties; or the bottom-up approach where nanoscopic features are "grown" using self-assembly of smaller atomic or molecular components (the way biology does things). Both approaches have their own pros and cons and can be used to create a wide range of nanobiotechnological systems and applications [7]. The top-down approach is more suitable (with less difficulty) for making connections from the macro- and microscopic scales to the nanoscale, while the bottom-up approach is more suitable at making connections from the molecular and atomic scales to the nanoscale. Nanosize biomolecules interact with things at or below the nanoscale and we wish to translate these interactions up to the macroscale without losing resolution. Thus, a generally more applicable and more complete nanobiotechnology approach is arguably more likely to include design features from both top-down and bottom-up approaches.

Nanochannels and nanopores fabricated in solid state materials are two examples of top-down fabricated nanostructures. Both nanochannels and nanopores provide geometries that are able to physically confine a few or single molecules in extremely small volumes. This asserts a basis for a higher degree of control over their observation or manipulation. Additionally, nanochannels and nanopores allow us to compartmentalise biomolecules to more closely replicate the crowded cellular environment where they are found naturally[8]. Nanochannels have been very useful in studying single DNA molecules with fluorescence microscopy techniques, as nanochannels with the right dimensions spontaneously stretch out the DNA to enable direct visualisation of genomic information[9]. Solid state nanopores have been found useful as sensors for monitoring single molecule translocation of DNA or proteins using ionic current fluctuations, or by incorporating additional plasmonic metal structures

capable of optical detection. This has directly provided tools for the sequencing single DNA molecules[10]. The nanoscale dimensions for both structures can be defined using ultra high-resolution patterning techniques. The more commonly used techniques include: electron-beam lithography (EBL), which create patterns in a deposited resist film acting as mask for subsequent etching steps; or focused ion beam milling (FIB), which can directly carve the channels or pores into the substrate surface[9], [11]. Nanopores can also be fabricated by many other means:[11], including e.g. controlled dielectric breakdown of the substrate material, laser pulling the tips of glass or quartz pipettes, or making patterns with adsorbed nanoparticles in colloidal lithography[12]. Nanochannels have the additional requirement of sealing the developed channels by bonding a second material as a sealing lid, where different approaches are available depending on the choice of substrate material[9]. Regardless of geometry, the surface wettability inside the structures needs to be very high towards aqueous solutions (i.e. they should be hydrophilic). This is commonly achieved by choosing a substrate material that contain, or can gain, an outer polar coating from for example hydroxyl groups ( $-OH$ ) or charged chemical species.

A general issue for studying proteins using devices made from solid state materials is related to how they interact with biomolecules. The propensity of proteins to adsorb and stick to solid material surfaces in a non-specific manner when exposed to samples containing proteins can quickly become a critical issue limiting the usefulness of a nanoscale device for many biomolecule applications[13]. Furthermore, it is not necessarily enough to have the tools, they also have to be "gentle" enough as to not adversely affect the states of the molecules as they are studied. Otherwise we may misinterpret their function as a result. Essentially, if the protein is in the wrong "mood" it may not provide relevant answers to our questions. Thus, we put a demand on the tools we use, as described by the following quote from my previous work[14]: "Therefore, one may think of our end goal as to avoid the analogous situation of interrogating a chained biomolecule with a sharp stick in a torture chamber, and instead create a biomolecular living room where the molecule can sit back and feel at home while it's politely asked a few questions over a cup of tea." Achieving this idealised picture in reality likely requires a much better understanding (than we currently possess) of biomolecular interactions and the naturally crowded world of biomolecules[8]. However, utilising synthetic "soft"

---

polymer materials or lipids that can replicate the same type of multivalent weak interactions and functional groups found in biomolecules and cellular environments is probably a good step in the right direction.

To remedy the biomolecule interaction problems of solid state nanostructures we can attempt to modify or add functionality to their surface properties by adding surface coatings. This is achievable via functionalisation chemistry in a bottom-up self-assembly approach[13]. Self-assembled monolayers (SAM) and their surface engineering applications form a basis for this concept. Typical examples of SAMs consists of various linear and short organothiol or organosilanes that have been surface tethered in one end and packed densely next to each other on a surface[15]. Different surface properties are then achieved depending on the chemistry of the oligomer chains that make up the SAM. SAMs have also been extensively studied for their use as *antifouling* surface coatings that resist non-specific protein adsorption, where short thiol terminated poly(ethylene glycol) (PEG) oligomers became the staple early on within the field[16], [17]. In more recent times, focus within the field of antifouling coatings has shifted more towards longer surface tethered polymeric chains, which if packed densely enough extend away from the surface forming what is known as a *polymer brush*. For polymer brushes, alternatives to PEG also have garnered a lot of interest[18].

Polymer brushes are highly hydrated surface coatings of wide interest for liquid applications, owing to their physical properties and chemical variability that provide an extensive range of functionality to material surfaces. The physical properties of polymer brushes are in many ways interconnected with the chemistry of the polymer chains. Monomer size, monomer volume, polymer chain length, chain flexibility, chain branching and chain surface grafting density play a central role in determining brush properties such as morphology, density distribution, height and viscoelasticity. However, the intra- and intermolecular interactions between chains, solvent and solutes also have a large impact on the brush properties and depend on the presence of different functional groups along the polymer chain. As a result, many kinds of polymer brushes are *stimuli-responsive* materials, i.e. they reversibly change their properties as a response to changes in various environmental and chemical factors[19]. This effect can be utilised to create "smart" nanomaterials that perform certain functions while changing their properties after being

triggered by a specific stimuli. Harnessing such functionality is of high interest for nanobiotechnology applications since it can be used to modulate the materials interaction with biomolecules at the nanoscale.

The work summarised in this thesis is aimed towards developing biofunctional PEG polymer brush coatings readily applicable to nanobiotechnological devices involving proteins, with a specific application focus towards nanopores. It is mainly based on the following previous research from my research group: cloud-point grafting of strongly stretched protein repelling PEG brushes on gold[20], how the same brushes also form a barrier that blocks translocation of proteins through nanopores[21], how anti-PEG antibodies can then "open" the PEG barrier via molecular recognition to let proteins through[22], and the fabrication of biosensing plasmonic nanoholes in a solid fused silica substrate[23] or silicon nitride membranes[24] using colloidal lithography. New research contributions covered by this thesis are based on the following four scientific papers:

**Paper 1** demonstrates that the inherent surface plasmon resonance signal of palladium and platinum in the Kretschmann configuration is sufficiently strong to study PEG brush grafting and antifouling ability. Palladium and platinum have important applications in organocatalysis and electrochemistry, two areas which are of interest for nanobiotechnological lab-on-a-chip devices with medical applications.

**Paper 2** presents a methodology to covalently functionalise silicon dioxide with densely grafted PEG polymer brushes that match the performance of similar brushes on metals. The functionalisation scheme is found to be well suited for two types of solid state nanostructures, which make this approach particularly promising for the nanobiotechnology field.

**Paper 3** investigates a pH-reversible change in PEG polymer brush properties and protein interactions when introducing poly(methacrylic acid) (PMAA) in solution below and above pH 5. The reversible polymer brush height changes has potential to be used in biofunctional surface coatings for proteins stable at a pH above 4-5.

**Paper 4** describes the fabrication and optical characteristics of plasmonic biosensing nanopore arrays in membranes with separately functionalisable

---

openings and interiors and long-ordered patterns defined by EBL. The long-order patterned pores are also compared to short-ordered nanopore membranes with an improved colloidal lithography fabrication approach. This paves the way to study protein translocation behaviour of functional coatings in nanopore membranes and is a step forward in the development of single nanopores with separately functionalisable openings and interiors.

Additionally, preliminary results are presented on the potential of utilising the PEG-PMAA interaction as a macromolecular gating system for nanopores (section 5.2.2) and controlling the PEG-PMAA interaction electrochemically in neutral pH (section 4.5).



# CHAPTER 2

---

## Background

---

*The following chapter is largely based on modified excerpts from my licentiate thesis work[14].*

## 2.1 Polymers in solution

Firstly, the topic of polymers is vast and there is a wide variety of types of polymers that possess an equally vast range of properties. Here we restrict ourselves to what can be considered linear polymers dissolved in solution, where the volume fraction of polymer is much less than that of the solvent molecules themselves. Since fully simulating the interactions and behaviours of all polymers in a solvent breaks down to a many-body problem, a less challenging approach is to look at an approximated system with less degrees of freedom.

A great deal of activity within this field occurred around the mid 20th century, which eventually ended up leading to a nobel prize in chemistry 1974 to Paul J. Flory for what is now known as the Flory theory of polymer chains. In his mean-field theory, a polymer chain in solution can be considered as an entropic spring, where the more stretched a polymer chain is, the more it will try to contract in order to increase its entropy and minimize its free energy[25], [26]. Due to each monomer occupying a certain volume, there must simultaneously exist a balancing force which prevent the polymer and its monomers to overlap. The balancing force acts radially outwards from the center-of-mass, resulting in a polymer "coil" (see Figure 2.1). This balancing force can be thought of in terms of osmotic pressure or entropic forces. The monomer volume which cannot be occupied by anything else give rise to what is known as the exclusion volume.

Flory also recognised that the properties of the solvent will play a role in the effective volume occupied by the polymer chain. Therefore, his formulation includes what happens when solvent interactions with the polymer can be considered favourable or unfavourable. The total Gibb's free energy for a polymer coil in solution including the conformational entropy, excluded volume and solvent interaction terms can be written as[27]:

$$G(r) = \frac{3k_B T r^2}{2abN} + \frac{k_B T v N^2}{r^3} [1 - \chi] + C \quad (2.1)$$

where  $r$  is the radius of the polymer coil,  $k_B$  is Boltzmann's constant,  $T$  is

temperature,  $N$  is the number of monomer units (degree of polymerization),  $a$  is the monomer size,  $b$  is the Kuhn length (effectively a measure of chain stiffness),  $v$  is the exclusion volume,  $C$  is a constant and  $\chi$  is the dimensionless solvency parameter, which can be expressed as:

$$\chi = \frac{z}{2k_B T} [2\epsilon_{ps} - \epsilon_{ss} - \epsilon_{pp}] \quad (2.2)$$

where  $z$  is the number of contact points,  $\epsilon_{ps}$ ,  $\epsilon_{ss}$ ,  $\epsilon_{pp}$  are the interaction energies of the polymer-solvent, solvent-solvent and polymer-polymer interactions respectively. Note that the interaction energies are in the form of energy barriers, where favourable interactions decrease the energy "cost" ( $\downarrow \epsilon$ ). It is also worth mentioning that finding accurate values for the physical polymer chain parameters  $a, b, v$  and especially the interaction energies (which depend on environmental conditions such as temperature, ionic strength, pH etc.) is no trivial task. Because it is difficult to determine the solvency parameter  $\chi$  in practice, it is commonly factored into the excluded volume parameter  $v$ , which then becomes dependent on solvent properties.

If we minimize the free energy with respect to  $r$  by taking the derivative equal to 0, we can find the most probable polymer coil size:

$$\frac{\partial G}{\partial r} = \frac{3k_B T r}{abN} - \frac{3k_B T v N^2}{r^4} [1 - \chi] = 0 \quad (2.3)$$

$$r = (abv[1 - \chi])^{1/5} N^{3/5} \quad (2.4)$$

Note that the coil size scales most strongly with the degree of polymerization (and thus with the average molecular weight of the polymer chains), but still the monomer geometry, chain stiffness and solvent interactions play an important role.

As can be seen in equation 2.2 and 2.4, higher polymer-solvent interaction will tend to stretch out the polymer coil, while the opposite is true for strong solvent-solvent or polymer-polymer interactions. For conditions where  $\chi \rightarrow 1$ , the solvent interaction counteracts the excluded volume effect and the polymer will behave just like an ideal chain exhibiting a random walk behaviour.

The polymer coil size will in this case instead scale on the order of  $N^{1/2}$ . Solvents that meet these conditions are usually referred to as "theta solvents" in the literature. If  $\chi > 1$ , the description above breaks down (imaginary coil radius!), which can be interpreted as the excluded volume being overpowered from unfavourable solvent interactions, leading to the polymer forming globules and phase separate from solution (see Figure 2.1). Assuming a globule then takes up a volume of  $V = Na^3$ , this should then give polymer sizes scaling on the order of  $aN^{1/3}$ , since the size of the globule cannot be much larger than the volume occupied by the physical size of all monomers.

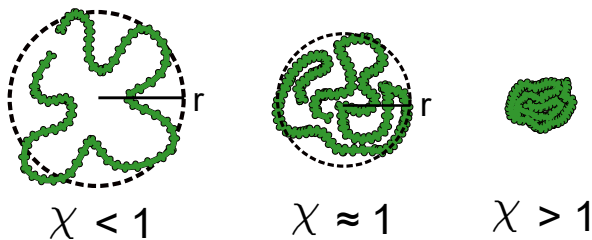


**Figure 2.1:** Polymer coils in a good, theta and bad solvent depicted from left to right.

## 2.2 Surface grafted polymers and polymer brushes

When one end of a polymer is attached to a surface and the rest of its chain remains free in solution, we can expect its coil to adopt a hemispherical "mushroom" shape bounded by the surface[28] (Figure 2.2a), where the polymer height  $h$  from the surface is roughly the same as its coil size  $r$  when free in the solvent. However, if the number of chains per area unit  $\Gamma$  (also known as the grafting density) of the chains is sufficiently high, the polymers can be forced to stretch out into a "polymer brush" configuration ( $h > r$ ) in order to avoid overlapping their coils[29]. In Figure 2.2b the polymer brush case is depicted in comparison with the mushroom case using the average grafting distance  $D = \Gamma^{-1/2}$ .

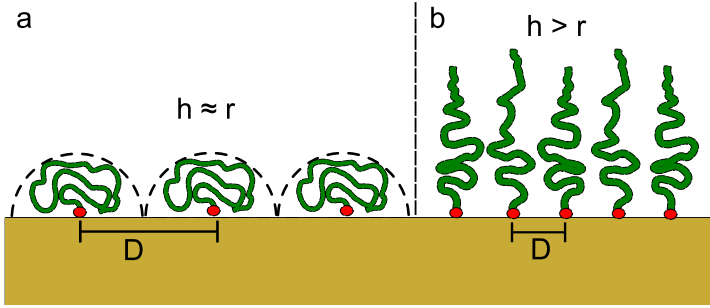


**Figure 2.2:** Polymers grafted to a surface adopting: **a** the mushroom configuration, or **b** the brush configuration.

To theoretically describe a polymer brush layer, we can adopt the same way of thinking as in the Flory theory, but replace the coil size  $r$  with the coil height  $h$ . Each polymer chain will then occupy a volume of  $h/\Gamma$  instead of  $r^3$  as was the case in equation 2.1. The free energy as a function of height can then be written as:[20], [27], [29]

$$G(h) = \frac{3k_BTh^2}{2abN} + \frac{k_BTv\Gamma N^2}{h} [1 - \chi] + C \quad (2.5)$$

If we then assume a very good solvent where  $\chi = 0$  for simplicity, and solve for  $h$  by taking the derivative = 0, we arrive at the polymer brush height:

$$H = \left[ \frac{abv\Gamma}{3} \right]^{1/3} N \quad (2.6)$$

We can then see how the polymer brush height  $H$  scales linearly with the degree of polymerisation and depends weakly on the grafting density. However, this description is only valid for strongly stretched brushes. Furthermore, the model assumes a constant monomer concentration within the brush volume, but it can be shown that the monomer concentration is more likely to adopt a parabolic density profile with respect to distance from the surface[29], [30] as depicted in Figure 2.3.

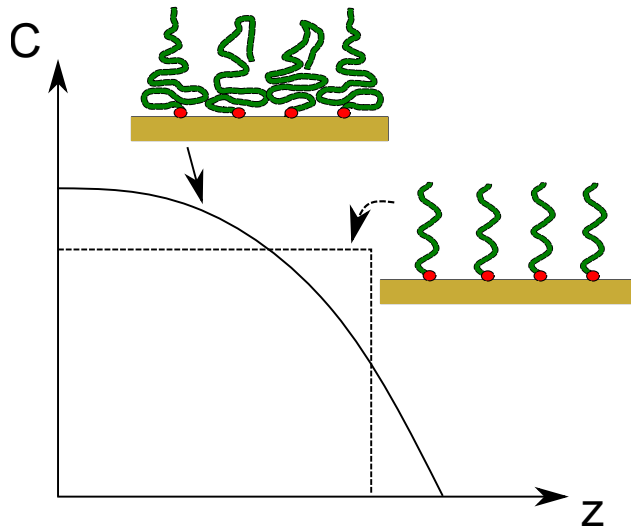


**Figure 2.3:** The monomer concentration  $C$  as a function of distance  $z$  from the surface. The dashed line represents the assumption of a strongly stretched brush (Alexander - de Gennes brush) while the solid line instead represents a parabolic monomer distribution.

### 2.2.1 Grafting strategies

In order to graft polymers with one end attached to the surface, the end-terminus of the polymer need a functional group that can bind directly to the surface atoms, or to a corresponding functional group that has been previously attached to the surface. There are essentially two different approaches to achieve this. The first involves attaching already existing polymer chains with a functional group to the surface covalently or by adsorption, known as "grafting-to". This approach tends to be simple and doesn't require any particular expertise from the user. The other approach instead involves functionalising the surface with an initiator group from which the polymer can grow directly in a polymerisation reaction, known as "grafting-from". Because of the small space taken up by the initiator molecule, grafting-from can achieve higher grafting densities and polymer brush heights compared to grafting-to. Additionally, since the grafting-from chains are grown continuously over time,

it is possible to control the height of a formed polymer brush layer by selecting a certain polymerisation time. On the other hand, accurate quantification of the grafting density becomes difficult in the grafting-from approach. The main reason is that there is currently no good way of directly and non-destructively quantify the degree of polymerisation or average molecular weight of polymer chains grafted to a surface[31].

In this work, a grafting-to cloud point approach[20] was used to form highly stretched PEG polymer brushes from thiolated PEG. The method relies on grafting the PEG dissolved at the solubility limit of a very kosmotropic salt (0.9 M  $\text{Na}_2\text{SO}_4$ ), which competes with the PEG for surrounding water interactions. This effectively turns the solution into a theta solvent for PEG and minimizes the polymer coil size at the limit of phase separation. The thiol end-group on the PEG is still able to form bonds with Au surfaces. Once the PEG has bound to the gold surface the solvent can be switched to regular water or a suitable buffer solution. As a result, the attached chains stretch away from the surface and form a polymer brush as to lower their free energy in the new PEG-favourable solvent conditions. The main advantage with this particular cloud-point approach is that it can form dense covalently attached PEG brushes using conditions that are not destructive to most materials.

## 2.3 Poly(ethylene glycol) (PEG)

PEG is a linear hydrophilic neutral polymer with the chemical formula  $C_{2n}H_{4n+2}O_{n+1}$  and a molecular structure pictured in Figure 2.4a. The most notable applications for PEG is within biomedicine and biotechnology, where due to its non-toxicity and increased circulatory life-time of PEG-covered proteins and nanoparticles has become an integral part in various drug delivery systems[32], [33]. The increased circulation time of PEG-covered particles comes in large part from the PEG chain's ability to resist non-specific protein interactions, thus delaying targeting mechanisms of the immune system. Previous studies have also shown that PEG displays excellent protein-repelling properties when grafted densely to surfaces in the form of a polymer brush[20] and may even block entry of proteins in nanosized apertures despite consisting mostly of water[21].

The exact mechanism behind the protein repelling ability of PEG and similar polymers is still debated. However, common properties of PEG and other polymers with similar repelling properties include high hydrophilicity, neutral charge and presence of hydrogen bond acceptors without donor groups[34]. The classical explanation for the high hydrophilicity of PEG relates to the gauche configuration of the PEG-backbone (Figure 2.4b) and its favourable orientation for hydrogen bonding with water. However, a more recent study points toward the increased electronegativity of the oxygen atoms in the backbone playing a more important role in formation of strong hydrogen bonds[35].

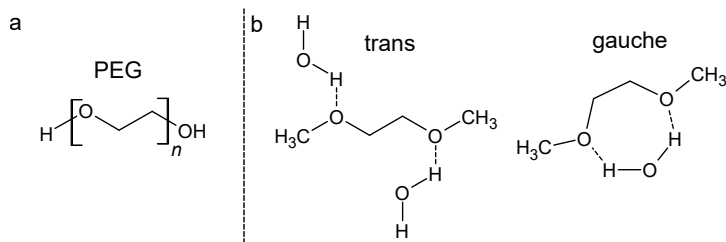


**Figure 2.4:** **a** Molecular structure of PEG. **b** Trans and gauche configurations of PEG backbone and their hydrogen bonding interaction with water molecules.

## 2.4 Poly(methacrylic acid) (PMAA)

PMAA is a linear polyacid with the chemical formula  $C_{4n}H_{6n}O_{2n}$  and structure as depicted in Figure 2.5. Polyacids are polymers that carry acidic groups along their polymeric backbone, which in PMAA's case is a carboxylic acid group located on every monomer. The carboxylic acid group further classifies PMAA as a weak polyelectrolyte, because the acid dissociation of the carboxylic acid group into a carboxylate group  $-\text{COO}^-$  is reversible with a dependence on solution pH. However, ionizing monomer groups along the polymer chain leads to additional free energy costs compared to the monomer by itself due to the electrostatic repulsion between neighbouring charges[36]. This means the acid dissociation constant  $K_a$  of PMAA will vary with the degree of ionisation.

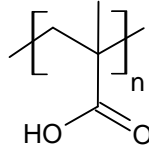


**Figure 2.5:** Molecular structure of PMAA.

The acid dissociation constant of a polyacid in solution is given by the relation[37]:

$$pK_a = pH + \log_{10} \left( \frac{1 - \alpha}{\alpha} \right) = pK_0 + A\alpha^{1/3} \quad (2.7)$$

where  $\alpha$  is the degree of ionization,  $K_0$  is the intrinsic dissociation constant at the limit of  $\alpha \rightarrow 0$  (the first monomer unit to dissociate) and  $A$  is a constant depending on temperature, ionic strength and the overall PMAA monomer concentration. The  $pK_a$  and  $\alpha$  at given conditions and PMAA concentration can be found from titration curves using a strong acid or base.  $pK_0$  and  $A$  can then be found from the linear regression of  $pK_a$  and  $\alpha^{1/3}$  [38]. For PMAA, equation 2.7 seems to be valid up to  $\alpha \approx 0.2$  which corresponds to an estimated upper pH limit of 5.3 at close to physiological conditions with  $pK_0 = 4.28$  and  $A \approx 2.64$ [37]. Thus, it is also possible to calculate e.g. the number of protonated monomer groups  $n_H$  of PMAA at a pH below 5.2, where  $n_H$  can be solved numerically from the adapted version of equation 2.7:

$$pH = 4.28 + \log_{10} \left( \frac{N}{n_H} - 1 \right) + 2.64 \left( 1 - \frac{n_H}{N} \right)^{1/3} \quad (2.8)$$

where  $N$  is the degree of polymerisation. Figure 2.6 gives the numerical solution to  $n_H$  in equation 2.8 for PMAA at physiological salt conditions (and slightly above and below).

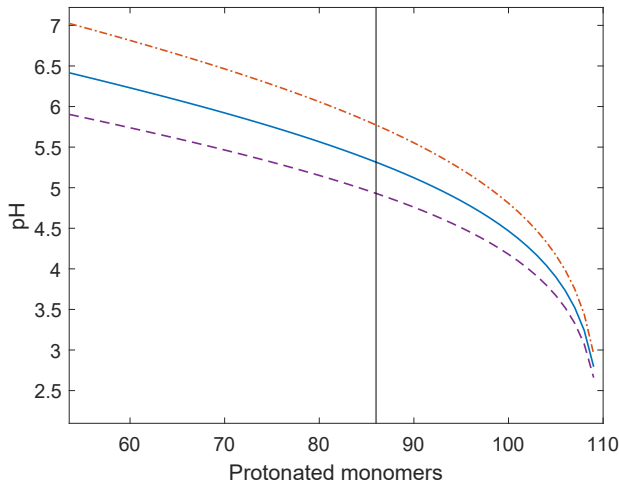


**Figure 2.6:** Number of protonated monomer groups  $n_H$  as a function of solution pH for PMAA with  $N = 110$ . The blue solid line corresponds to physiological salt conditions (150 mM) ( $A = 2.64$ ), while the violet dashed line corresponds to above 150 mM salts ( $A = 2.0$ ) and the orange dashed line to below 150 mM salts ( $A = 3.4$ ). The model can be considered valid for the number of monomer groups above that indicated by the black vertical line.

A charged polyelectrolyte tends to have a significantly swelled polymer coil in solution compared to the corresponding uncharged polymer chain (such as a weak polyelectrolyte at low pH where  $\alpha \rightarrow 0$ ). This is due to two effects[39]. An increasing number of repulsive charges along the polyelectrolyte chain will cause intra-polymer repulsion and effectively lead to an increase in the chain stiffness  $b$ . As we can see from equation 2.1 this decreases the chains conformational entropy. To counter the excess free energy, the polymer will increase its coil size until it reaches an equilibrium. In addition to this, coulombic charges will more strongly attract polar molecules such as water. Thus, in aqueous solutions the polymer-solvent interactions will increase and cause an additional swelling of the polymer coil to lower the excluded volume term in equation 2.1. Furthermore, the presence of counter-ions in solution will effectively screen the charged monomer groups and their contribution to the intra-polymer repulsion along the polyelectrolyte chain. In some cases

this means an increase in ionic strength of the solution will shrink the size of a polyelectrolyte coil. However, if the interacting counter-ions have a larger hydration shell than the monomer charges of the polyelectrolyte, swelling of the coil can occur instead.

## 2.5 Hydrogen-bonded interpolymer complexation

For mixtures of polymers with monomer units containing suitable hydrogen bonding donor and acceptor groups, interpolymer complexes have been observed to form in solution as a function of solution pH[38], [40]–[45]. The phenomenon seems to occur between weak polyelectrolytes containing carboxylic acid groups and non-ionic polymers containing hydrogen bond acceptor groups (such as alcohols, ethers, acrylics, lactamates, sachharides etc.)[40].

Notably, the formation of the complexes only start below a certain critical  $\text{pH}_{crit}$ , above which no interaction occurs and the polymers are able to co-exist freely in solution. The formation is also completely reversible if solution pH is changed back to above  $\text{pH}_{crit}$  after complexes have already been formed. Several factors have been found to influence the acquired  $\text{pH}_{crit}$  for a given pair of complexing polymers. Environmental conditions such as temperature and salt concentration have a clear effect, but also the properties of the polymers themselves matter, such as polymer concentration, degree of ionisation and polymer molecular weight. Studies of interpolymer complexes formed between PEG and PMAA or PEG and poly(acrylic acid) (PAA) have also revealed that hydrophobic interactions can further stabilise the complex[43]. It was found that the PEG-PMAA interactions become even stronger at increased temperature (when hydrogen bonding effectively decrease in strength[46]), while the same effect is much less pronounced for PEG-PAA interactions. Aside from studies of interpolymer complexes in solution, the interpolymer complexation concept have also been studied as a system of constructing bottom-up layer-by-layer films [40], [47].

The properties of the PEG-PMAA interpolymer complex is of particular interest for the work presented in **Paper 3**. It has been found to form at a 1:1 monomer ratio and start forming around  $\alpha < 0.1$ -0.12 for PMAA[45],

[48], which corresponds to a  $\text{pH}_{crit}$  of about 4.5-4.8 at physiological conditions according to the model in Figure 2.6. Small angle neutron scattering measurements of the chain interactions of PEG-PMAA complexes at low pH found that the chains "zip together" and that the complex display an increased density compared to either of the chains free in solution[48].

## 2.6 Electrochemistry

Atoms and molecules may undergo chemical change as a result of gaining or losing electrons. In "conventional" chemistry, chemical reactions happen when different chemical species directly interact as they meet, which open up for new more energetically favourable states for the loosely bound valance electrons of one of the species. If conditions are right, this leads to a high probability that the electron(s) transfer between the species and chemical change happens as a result. In electrochemistry, two or more conductive solid electrodes inserted into a conductive medium (an electrolyte) make up an electrochemical cell that can transfer and build up charge between the electrodes. The three-electrode setup together with a *potentiostat* (a feedback-driven voltage control device) is commonly used for performing accurate electrochemistry experiments. The three electrodes are: the *working electrode*, to which the desired potential is applied and where the reaction of interest takes place; the *counter electrode*, where the opposing potential is applied; and the *reference electrode*, which is chemically inert and used for setting accurate potentials even as reactions at the other two electrodes happen.

When a positive or negative electrical potential is applied over the working electrode from the potentiostat, the energy level (Fermi level) of electrons at the electrode surface is decreased or increased respectively[49]. This effect can be utilised to tune and drive electron transfer (and thus chemical change) between chemical species in the electrolyte and the atoms in the electrode interface in either direction in reduction-oxidation (redox) reactions. At equilibrium conditions and unity activation of the chemical species, the balancing relationship between chemical and electrical energy can be described using the Nernst equation[49]:

$$E = E^0 + \frac{RT}{nF} \ln \left( \frac{C_O}{C_R} \right) \quad (2.9)$$

which relates the electrical potential,  $E$ , to the concentration of the chemical species that lost electrons (were oxidized),  $C_O$ , and to those that gained electrons (were reduced),  $C_R$ . Here  $E^0$  is the standard electrode potential characteristic for the reaction of interest relative to the used reference electrode,  $R$  is the gas constant,  $T$  is the temperature,  $n$  is the number of involved electrons and  $F$  is the Faraday constant. However, there are also many other practicalities affecting the outcome of electrochemistry experiments, including: pressure, electrode variables (material, surface area, geometry, surface condition), mass transport conditions (diffusion, convection, hindering surface adsorbates) and solvent variables (polarisability, ionic strength, pH)[49].

### 2.6.1 Electrochemistry in nanoscience

While electrochemistry has seen a lot of use historically in both industrial and research sectors alike[49], it is also gathering new interest in the fields of nanotechnology and nanoscience[50]. For example, electrochemical technologies can be used to fabricate and characterise micro- and nanorobots with broad applications in engineering, biomedicine and environmental technologies[51]. Electrochemistry has also entered the field of single-molecule studies, detecting single molecules and characterising their electrochemical reactions[52] or developing electrochemical transistors for future molecular computers[53]. There is also interest in the possibilities of miniaturised sensors based on combinations of electrochemical and refractometric sensing principles with enhanced sensor functionality and unique advantages as a result[54].

For this thesis work, one particularly relevant electrochemical nanotechnology is the increasing use of electrochemical biosensors that study biocatalyzed electron transfer reactions from biomolecules such as enzymes and antibodies[55]. As with most types of biosensors, non-specific adsorption of biomolecules is a major challenge that needs to be addressed and long-chained polymer brushes have shown a lot of promise in this regard also for electrochemical biosensing applications[55]. Another particularly relevant application here is the use

of proton generating electrochemical reactions for spatially localised pH control[56]. This principle has also been applied to polyelectrolyte brushes to selectively capture and release proteins on demand[57]. Here it is investigated further in section 4.5 as a means of electrochemically controlling the PEG-PMAA intercomplexing interaction described in **Paper 3** and section 4.4.

# CHAPTER 3

---

## Characterisation techniques

---

*The following chapter is largely based on modified excerpts from my licentiate thesis work[14].*

### 3.1 Surface plasmon resonance

Surface plasmon resonance (SPR) is a sensitive optical (refractometric) label-free technique that can detect nanoscopic changes continuously, such as a few ng/cm<sup>2</sup> of molecules adsorbing in the immediate vicinity of a sensor surface. Most SPR instruments are set up with flow cells with an inlet and outlet. This not only allows for measurements at dry conditions, but also enable to study real-time changes at liquid conditions while injecting different samples. Additionally, depending on the instrument setup, some SPR instruments can simultaneously measure the refractive index of the bulk medium above the sensor surface.

The SPR technique is based on a phenomenon which occurs in thin films of certain metals, such as gold or silver (or other materials with similar properties), that can form so called surface plasmons. Surface plasmons are surface bound oscillating waves of electrons moving in a collective manner. They form only given certain conditions and propagate along the interface of the thin metal film and a dielectric (insulating) medium. Maxwell's equations for electromagnetic radiation can be used to derive a description of the propagation and the necessary conditions required for a surface plasmon. Restricting to two dimensions, the result describes two wave vectors, one propagating in the x-direction along the surface boundary of the metal and one in the z-direction away from the surface boundary (see Figure 3.1). Since the z-component wave vector  $k_{z,sp}$  can be described in terms of the x-component  $k_{x,sp}$ , we end up with the following dispersion relation[58], [59]:

$$k_{x,sp} = \left(\frac{\omega}{c}\right)^2 \sqrt{\frac{\epsilon_1 \epsilon_m}{\epsilon_1 + \epsilon_m}} \quad (3.1)$$

where  $\lambda$  is wavelength,  $\epsilon_m = Re(\epsilon(\omega)) + iIm(\epsilon(\omega))$  is the frequency dependent complex dielectric constant of the metal film and  $\epsilon_1$  is the dielectric constant for the dielectric medium in contact with the metal surface. The dielectric constant is related to the complex refractive index  $\tilde{n}(\omega) = n(\omega) + i\kappa(\omega) = \sqrt{\epsilon(\omega)}$  of a given medium, where the refractive index  $n = Re(\tilde{n})$  describes the speed of light in the medium as a fraction of light speed in vacuum. The extinction coefficient  $\kappa = Im(\tilde{n})$  describes the degree of absorption of light in

the medium.

Since the surface plasmon also extends in the z-direction, it has an associated electric field  $E_z$  extending away from the surface plane into both surrounding media, as depicted in Figure 3.1. A common way to denote the extent of the electric field decay is to use the decay length  $\delta(\lambda)$ , which is defined as the distance from the surface where the field strength has decayed by  $1/e$ . For the dielectric medium  $\epsilon_1$  the decay is given as:

$$\delta_1(\lambda) = \frac{\lambda_p}{2\pi} \sqrt{\frac{\text{Re}(\epsilon_m) + \epsilon_1}{\epsilon_1^2}} \quad (3.2)$$

where  $\lambda_p$  is the plasmon wavelength. It is important to note that  $\delta_1/2$  in general depends on the *effective* dielectric constant above the metal surface. This means that it there effectively exists a different decay length in each layer.

In order for light to convert into surface plasmons, an impinging photon must be able to match the plasmon wave vector according to:

$$k_{ph} = \left(\frac{\omega}{c}\right)^2 \sqrt{\epsilon} = k_{sp} \quad (3.3)$$

Since the momentum of light from a beam travelling in air with  $n = \epsilon = 1$  will always be insufficient in order to satisfy the plasmon condition described in equation 3.1, the missing momentum has to come from somewhere else. The most common ways to achieve this are by using a grating or attenuated total reflection (ATR) coupler, the principle behind the latter of which will be described here. In the Kretschmann configuration depicted in Figure 3.1, an incident monochromatic p-polarized light beam is directed through an optically denser medium, such as glass prism, that is in direct contact with a thin metal film connected to an opposing less optically dense dielectric medium ( $\epsilon_1 < \epsilon_2$  in Figure 3.1).

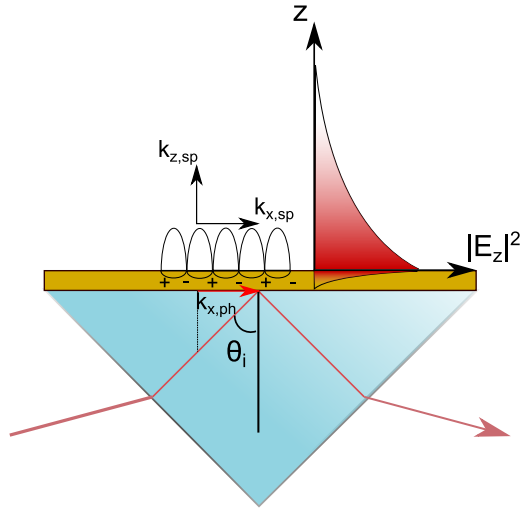


**Figure 3.1:** Surface plasmon excitation using the Kretschmann-Raether configuration.

As the light beam is reflected from the metal/prism interface above the critical angle of total internal reflection  $\theta_{TIR}$ , a projected x-component of the incoming photon propagates with a wave vector  $k_{ph}$  along the interface. The propagating wave component has an associated electric field extending perpendicular to the surface plane that is continuous (also through the metal) into the dielectric on the other side, known as the evanescent field. The evanescent field allows the impinging photon to initiate surface plasmons at the metal/dielectric interface. At a certain incidence angle  $\theta_i$ , the wave vector  $k_{ph}$  is matched with  $k_{sp}$ , resulting in a sharp loss in reflected light intensity ( $I_R$ ) as a majority of the incoming light is absorbed by the metal through the evanescent field and transformed into surface plasmons. The absorbed energy from the light is then eventually given off as heat. Figure 3.2 shows where the resonance angle  $\theta_{SPR}$  and total internal reflection angle  $\theta_{TIR}$  is found in an angular reflectivity spectrum obtained using the Kretschmann configuration.

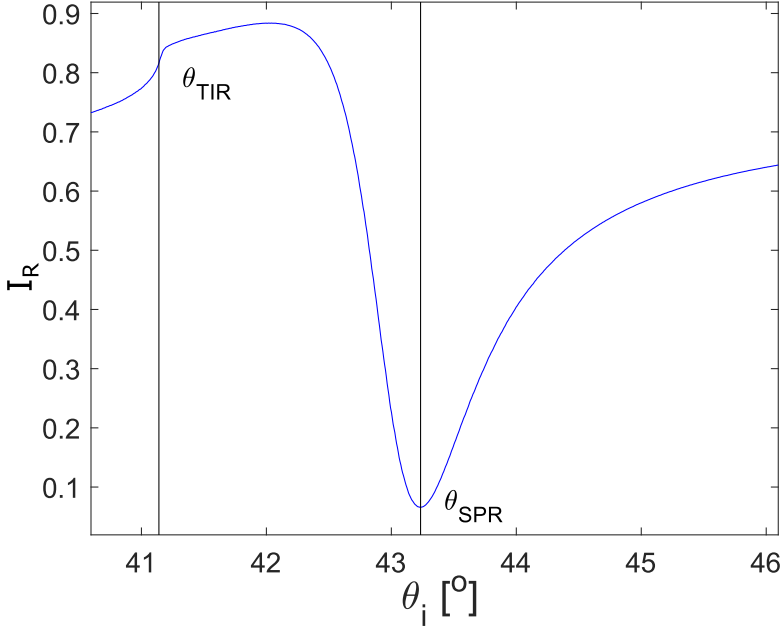


**Figure 3.2:** Surface plasmon resonance angular reflectivity spectrum for a  $\lambda = 670$  nm light source reflecting in the Kretschmann configuration off of a 50 nm gold film exposed in air. Vertical lines are drawn at the  $\theta_{TIR}$  and  $\theta_{SPR}$  angles.

The high sensitivity of the SPR technique originates from the dielectric constant dependence (and by extension refractive index) of the surface plasmons. Even small differences in the average refractive index within the plasmon electric field above the metal surface will significantly alter the  $\theta_{SPR}$  required to match the plasmon wave vector  $k_{x,sp}$ . Selecting different wavelengths of the incoming light means different resonance conditions for the surface plasmon will be fulfilled. Thus, as implied from equation 3.2, longer wavelengths will sense further away from the surface compared to shorter wavelengths. Long wavelengths together with smaller angles enable studies of relatively thick films. However, due to the larger probing volume of longer wavelengths, the sensitivity will also decrease[60]. In practice, this means that the lowest possible wavelength is usually desired.

### 3.1.1 Quantitative interpretation of the SPR response

Translating the angular response  $\Delta\theta_{SPR}$  of a measured process in SPR requires an understanding of the properties of both the instrument and the investigated material. The relationship between the angular response  $\Delta\theta_{SPR}$  and the corresponding change in refractive index units at the surface is[61]:

$$\Delta n_S = \frac{\Delta\theta_{SPR}}{S_{SPR} \left(1 - e^{\frac{-2d}{\delta(\lambda)}}\right)} \quad (3.4)$$

where  $S_{SPR}$  is an instrument specific sensitivity constant,  $d$  is the thickness of the layer within which the change is occurring and  $\delta(\lambda)$  is the decay length as given in equation 3.2. As can be seen in the exponential factor, unless  $d$  is known or occurs within a large thickness where  $d \gg \delta$  (corresponding to a bulk change), it is difficult to calculate accurate refractive index changes of the surface layer without any assumptions of the layer thickness [61]. If the SPR instrument is able to measure  $\Delta\theta_{TIR}$ , this will have an additional sensitivity constant  $S_{TIR}$ , which is included in the relation of the bulk refractive index change given as:

$$\Delta n_b = \frac{\Delta\theta_{TIR}}{S_{TIR}} \quad (3.5)$$

For example, for an e-beam evaporated gold film in the MP-SPR Bionavis Naali 220A gives:  $S_{SPR} = 116$  deg/RIU,  $S_{TIR} = 74$  deg/RIU and a decay length roughly equal to  $\delta(\lambda) = 226$  nm at a wavelength of 670 nm in water[62].

An important parameter for surface binding of dissolved adsorbents, such as proteins or polymers, is the refractive index increment with concentration,  $\partial n/\partial C$ . It is possible to determine this from the  $\Delta\theta_{TIR}$  of an SPR measurement by injecting a series of known concentrations of the adsorbant and perform a linear regression between the respective  $\Delta n_{bulk}$  and  $C$ , where  $\partial n/\partial C$  is the slope of the fitted line. For PEG,  $\partial n/\partial C = 0.1337$  RIU cm<sup>3</sup>/g and for PMAA at pH 4.5 and physiological salt conditions  $\partial n/\partial C = 0.1577$  RIU cm<sup>3</sup>/g. The average generally accepted value for proteins is 0.182 RIU

cm<sup>3</sup>/g[63].

The mass surface coverage  $m_S$  can be calculated (usually in ng/cm<sup>2</sup>) from  $\Delta\theta_{SPR}$  and estimates of  $d$  according to the general relation:

$$m_S = \frac{d\Delta\theta_{SPR}}{\frac{\partial n}{\partial C} S_{SPR} \left(1 - e^{-\frac{2d}{\delta(\lambda)}}\right)} \quad (3.6)$$

However, at the limit of  $d \rightarrow 0$  when  $d \ll \delta$ , it can be shown[20] that the surface coverage can be approximated as:

$$m_S = \frac{\delta\Delta\theta_{SPR}}{2\frac{\partial n}{\partial C} S_{SPR}} \quad (3.7)$$

### 3.1.2 Fresnel modelling of SPR measurements

The thickness and refractive index of an adlayer can also be extracted from SPR measurements without depending on estimates of the decay length  $\delta$ . The full angular reflectivity spectrum can instead be modelled using the Fresnel equations. In simple terms, the Fresnel equations describe how incoming light waves interact with different materials by either propagating through them, reflecting off of them or being absorbed or scattered by them. Their formulation comes from Maxwell's equations of electromagnetism, which means that they end up within a framework that also includes conditions for the description of surface plasmons. In essence, the Fresnel equations provide Fresnel coefficients which describe the amplitude of the light wave (in terms of the electric field vector  $|E|^2$ ) that is reflected ( $F_r$ ), transmitted ( $F_t$ ) and absorbed/scattered ( $F_a$ ) as fractions between 0 and 1[60]. However, the intensity of light is a more practically interesting quantity for SPR applications as it directly relates to  $I_R$  measured by a detector. Such intensity-based Fresnel coefficients follow as:

$$F_R = |F_r|^2 \quad (3.8)$$

$$F_T = \frac{Re(n_2 \cos(\theta_t))}{Re(n_1 \cos(\theta_i))} |F_t|^2 \quad (3.9)$$

$$F_A = 1 - F_R - F_T \quad (3.10)$$

where  $F_A$  describes the absorbed intensity,  $F_R$  describes reflected intensity and  $F_T$  describes the transmitted intensity,  $n_1$  and  $n_2$  are the refractive index of the medium occupied by the incoming and outgoing light respectively,  $\theta_i$  is the incident angle and  $\theta_t$  is the transmission angle.

For the application of surface plasmons, we are only interested in describing the p-polarised light component (for which the electric field components are perpendicular to the surface) of the reflection and transmission intensity based Fresnel coefficients  $F_{Rp}$  and  $F_{Tp}$ . Consider the simple case of a thin layer of thickness  $d$ , sandwiched between two media extending to "infinity" in opposite directions, illustrated in Figure 3.3.

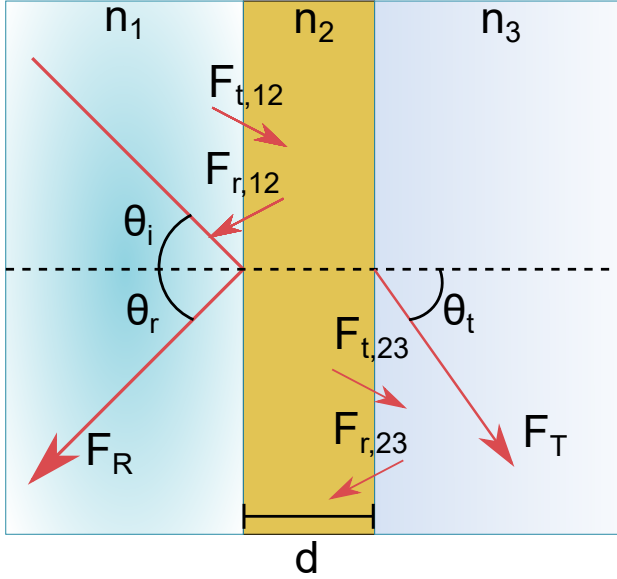


**Figure 3.3:** Light propagating through a thin film sandwiched between two semi-infinitely extending media. In general, the summed up intensity of reflected and transmitted light ( $F_R$  and  $F_T$ ) can be described by the amount of light reflected and transmitted at each material interface.

For this case, the Fresnel coefficients  $F_{rp}$  and  $F_{tp}$  can be described according to:

$$F_{rp} = \frac{F_{r,12} + F_{r,23}e^{i2k_0dn_2 \cos(\theta_2)}}{1 + F_{r,12}F_{r,23}e^{i2k_0dn_2 \cos(\theta_2)}} \quad (3.11)$$

and

$$F_{tp} = \frac{F_{t,12}F_{t,23}e^{ik_0dn_2 \cos(\theta_2)}}{1 + F_{r,12}F_{r,23}e^{i2k_0dn_2 \cos(\theta_2)}} \quad (3.12)$$

$d$  is the layer thickness,  $\theta_2$  is the angle of transmitted light in layer 2 of Figure 3.3,  $k_0 = \frac{2\pi i}{\lambda_0}$  where  $\lambda_0$  is the wavelength of the light. The exponential factor in equations 3.11 and 3.12 accounts for the interference that occurs between reflected and transmitted light within each layer.

For more complicated multi-layered systems, the transfer-matrix-method[60] can be employed for any number of intermediate layers  $j$  and medium  $m$ :

$$\Phi = \prod_{j=2}^{m-1} \left( \frac{1}{F_{t[j-1]j}} \begin{bmatrix} 1 & F_{r[j-1]j} \\ F_{r[j-1]j} & 1 \end{bmatrix} \times \begin{bmatrix} e^{-ik_0 d_j n_j \cos(\theta_j)} & 0 \\ 0 & e^{ik_0 d_j n_j \cos(\theta_j)} \end{bmatrix} \right) \times \frac{1}{F_{t,[m-1]m}} \begin{bmatrix} 1 & F_{r,[m-1]m} \\ F_{r,[m-1]m} & 1 \end{bmatrix} \quad (3.13)$$

where the general relation for finding the transmission angle between neighbouring layers of a multilayered system is:

$$\theta_{j+1} = \operatorname{Re} \left( \arcsin \left( \frac{n_j}{n_{j+1}} \sin(\theta_j) \right) \right) - i \left| \operatorname{Im} \left( \arcsin \left( \frac{n_j}{n_{j+1}} \sin(\theta_j) \right) \right) \right|$$

The final coefficients for the reflection and transmission are found as:

$$F_{rp} = \frac{\Phi(2, 1)}{\Phi(1, 1)}, F_{tp} = \frac{1}{\Phi(1, 1)} \quad (3.14)$$

Finally, equations 3.8 and 3.9 are used to translate the amplitude based Fresnel coefficients in equation 3.14 into the reflected or transmitted light intensity Fresnel coefficients equivalent to the light intensity measured by a detector.

In summary, if both the refractive indices and thicknesses of all layers are known but for one, the final unknown parameter can be determined from Fresnel model fits of the angular reflectivity spectrum around the  $\theta_{SPR}$  sensitive region. However, as long as background matching (e.g. fitting measurements of an empty sensor) is performed on a sample prior to applying an adlayer of interest, the resulting parameters of all other layers do not need to be physically accurate. The reason why either the refractive index or the thickness of an adlayer needs to be known to determine the other is because of their convolution, i.e. they contribute to the SPR response in a very similar way. In the case of dry protein or polymer layers in air, the refractive index of their bulk counterparts can be considered a good approximation. This means

their thickness can be determined very accurately, so long as the layer can be considered homogeneous in three dimensions. If the density  $\rho$  and molecular weight  $M$  of the protein or polymer is known, the surface grafting density  $\Gamma$  can be determined according to:

$$\Gamma = \frac{\rho d N_A}{M} \quad (3.15)$$

where  $N_A$  is Avogadro's constant.

Fresnel modelling can work also in liquid media. Since the effective refractive index of the bulk medium  $n_b$  can vary significantly with the presence and concentration of particulates or macromolecules, it will often become necessary to precisely determine  $n_b$  for every measurement in order to get an accurate model. Snell's law of refraction,  $n_1 \sin(\theta_i) = n_2 \sin(\theta_t)$ , can be used for this purpose. It describes at what angle light is transmitted from one medium to another as it crosses the boundary between the two. However, when incoming light propagating from a medium of higher refractive index to that of lower refractive index above a critical incidence angle  $\theta_c$  no physical solution exists. Light is instead reflected from the surface at an angle according to the law of reflection  $\theta_r = \theta_i$ . The critical angle denotes the start of the total internal reflection condition and this is the same  $\theta_{TIR}$  that is measured in SPR. Thus, the average refractive index of the bulk medium  $n_b < n_p$  can be calculated from an angular reflectivity spectra containing the  $\theta_{TIR}$  according to:

$$n_b = n_p \sin(\theta_{TIR}) \quad (3.16)$$

However, for many types of adlayers the modelling results in liquid can become physically inaccurate, as solvent interactions can contribute to swelling and vertical heterogeneity. This means that the effective refractive index for that layer becomes a function of distance from the surface (such as the parabolic density profile of polymer brushes discussed in section 2.2) and often very hard to predict.

### 3.1.3 Non-interacting probe method

When we do not know either the refractive index or the thickness of the investigated adlayer, direct Fresnel modelling run into accuracy problems as discussed in section 3.1.2. A solution to this problem termed as the "Non-interacting probe method" has been presented in the work of Schoch *et al.* 2013[64]. The height of protein repelling PEG brushes on an SPR sensor could be determined from "physically probing" the brush with proteins that were repelled by the brush layer. The authors use a formalism where the vertical difference in sensitivity in the form of the decay length (equation 3.2) can be deduced using a reference PEG layer of lower molecular weight and a known thickness. However, since the decay length is also a function of refractive index of the adlayer, this approach could only produce sufficiently accurate results for adlayers within a refractive index range of 1.35-1.4, based on the choice of reference layer by the authors. The general principle behind the non-interacting probe method is illustrated in Figure 3.4.

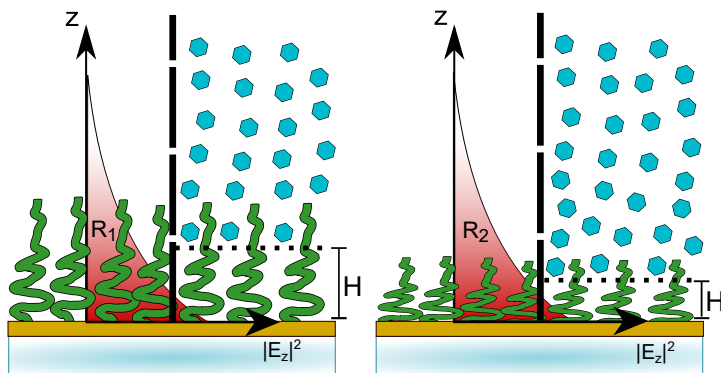


**Figure 3.4:** Illustration of the non-interacting probe method. The SPR response from a system containing, e.g. a polymer brush layer, with and without the presence of a non-interacting probe, can be used to extract an exclusion height above which the probe is repelled. This is possible due to the variation in sensitivity with distance originating from the decaying evanescent field. Thus, a shorter brush generates a larger SPR response compared to a taller brush during probe injection, since the probes are able to occupy a larger portion of the decay length ( $R_2 > R_1$ ).

An improved version of the non-interacting probe method was presented by Emilsson and Schoch *et al.* 2017, where the decay length limitation could be avoided all together. The approach is based on performing separate Fresnel modelling for angular reflectivity spectra of the adlayer both with and without the presence of the probe molecule. The only difference between these two states will essentially be the  $n_{bulk}$  contribution. By applying the model to a range of plausible refractive indices for both states (with and without probe), a corresponding range of possible exclusion heights can be extracted for both states. If the pairs of  $[H, n]$  for both states are plotted together, the unique solution to the exclusion height and corresponding refractive index of the adlayer will present itself graphically as an intersect of the two curves (see Figure 3.5 c). This approach can be thought of in similar terms as the algebraic problem of solving for two unknown variables using two related equations with different (but known) constants.

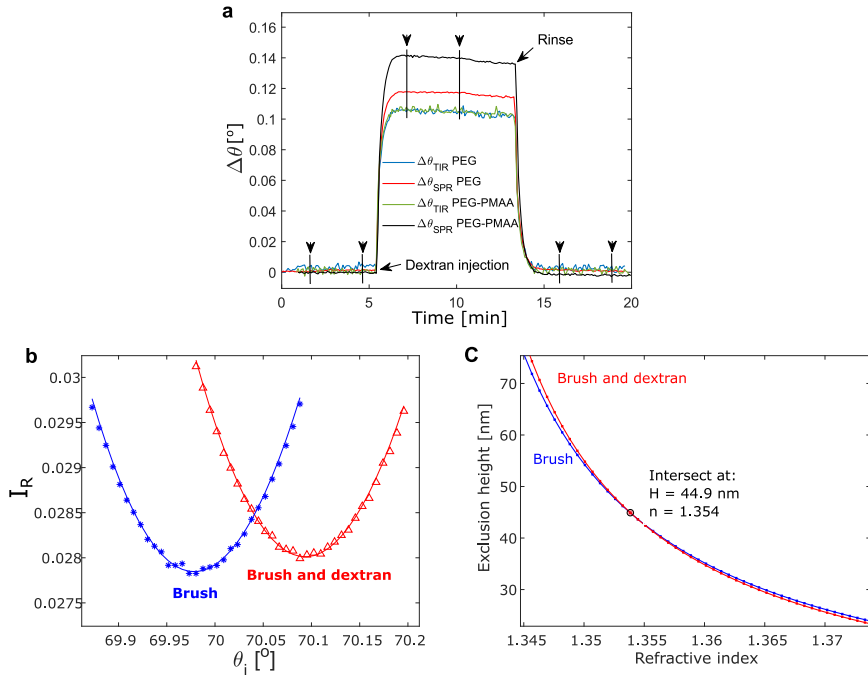


**Figure 3.5:** Examples of: **a** TIR and SPR signals during dextran injection on a PEG brush (blue and red respectively) and on a PEG-PMAA complex (green and black respectively). While the bulk refractive index is the same with and without adsorbed PMAA as shown in the two TIR signals, the SPR response is larger when PMAA is adsorbed. As the adlayer height shrinks from adsorbing PMAA, the probe molecules in the bulk liquid gets closer to the surface, leading to an increase in the SPR response. The arrows with accompanying vertical lines illustrate a typical range selection of the set of reflectivity scans used to acquire pairs of  $[H, n]$  in the Fresnel modelling. **b** Fresnel model fits (solid lines) of averaged reflectivity spectra close to the resonance minimum for a PEG brush without probe (blue stars) and a PEG brush during dextran injection (red triangles). Given a range  $N$  of refractive indices  $n_N$ , the Fresnel model predicts an equal number of possible heights  $H_N$ . In **c** the pairs of  $[H, n]$  are plotted for the brush with and without the dextran probe, resulting in an intersection where a unique solution to the brush  $H$  and  $n$  is found.

In the work presented in **Paper 3**, additional measures were taken to improve the quality of the exclusion height analysis. As exemplified in Figure 3.5a, sets of measurement points before, during and after probe injection were selected and turned into averaged angular reflectivity spectra (Figure 3.5b). Thus, two exclusion height measures are acquired per probe injection. This helps to reduce the influence from measurement noise and to evaluate the reliability of the resulting exclusion heights. For example, in Figure 4B of **Paper 2**, the presented exclusion height corresponds to the mean of a total of 12 exclusion height measures from three probe injections injected in parallel on two different spots on the sample surface ( $2 \times 3 \times 2 = 12$ ).

Note that the exclusion height may not necessarily describe the full extension of an adlayer if its outer portions have too low density to repel the probe. For example, this may be the case for some polymer brushes with a more pronounced parabolic density profile (see section 2.2). Similarly, the refractive index measured using the non-interacting probe method only provides the effective value of an adlayer between the surface and the obtained exclusion height.

## 3.2 Quartz crystal microbalance with dissipation monitoring

Quartz crystal microbalance (QCM) is an acoustic characterisation technique for studying mechanical properties of thin surface layers in real-time. The working principle behind QCM is based on the use of a piezoelectric quartz crystal that is cut along a specific crystallographic plane (AT cut), making it shear when exposed to an electric field (see Figure 3.6a). Applying an AC-voltage will cause shear oscillations in the QCM crystal. If the driving frequency matches the crystal's characteristic resonance frequency a standing wave will form through the crystal and the amplitude of the shear oscillations will be at a maximum.

The resonance frequency of the QCM crystal (and any of its odd numbered harmonics or "overtones") is intricately tied to its mechanical properties and the properties of the medium it oscillates in. If any of these properties change, such as its mass, the resonance frequency will also change[65] (see Figure 3.6b). This property can be utilised to create a microbalance capable of measuring changes in mass of deposited thin films or particles continuously. However, this is only provided that the change can be viewed as an extension of the mass of the crystal itself. In order for that assumption to remain true, the added mass must be rigidly attached to the surface of the sensor and much smaller than the total mass of the crystal[66]. Following these criteria, the Sauerbrey equation[67] provides a linear relationship between the change in areal mass  $\Delta m$  and the response in resonance frequency shift  $\Delta f_n$  according to:

$$\Delta m = \frac{-C\Delta f_n}{n} \quad (3.17)$$

where C is a sensitivity constant dependant on the intrinsic properties of the QCM crystal ( $= 17.7 \text{ ng/cm}^2$  for AT-cut crystal with  $f_0 = 5 \text{ MHz}$ ) and  $n = 1, 3, 5, 7\dots$  is the overtone number. Note that  $\Delta m$  is a total mass change, meaning that the mass of any solvation layer coupled to the oscillation is also included in the frequency response. If the formed layer's density  $\rho$  is known, the areal mass determined from the Sauerbrey equation can be used to derive the layer thickness.

If the layer deposited on the QCM crystal is not rigidly attached to the surface

and instead should be considered "soft", the resonance frequency response will be dampened by the additional energy dissipation caused by the viscoelastic properties of the layer. This means that a non-linear frequency dependency exists and the Sauerbrey equation no longer holds. For studying viscoelastic materials in liquid environments, Quartz crystal microbalance with dissipation monitoring (QCM-D) provides additional useful information by also measuring the dissipation factor  $D_n$  defined as:

$$D_n = \frac{1}{\pi f_n \tau} \quad (3.18)$$

where  $\tau$  is the decay time of the amplitude as the driving AC-voltage is turned off[66]. An increasing viscoelastic behaviour will cause more energy dampening and thus show up as an increase in the dissipation signal (see Figure 3.6 c and d).

Measuring  $\Delta f$  and  $\Delta D$  at several overtones can provide additional insights. While each overtone has the highest sensitivity in the centre of the sensor[68], the sensitive area decreases radially towards the centre with increasing overtone number. For this reason, the fundamental frequency ( $n = 1$ ) can occasionally be prone to noise originating from the edge of the sensor surface, in which case measurements at higher overtones are preferable. The viscous penetration depth  $\delta$  (the height sensitivity) also varies depending on frequency, ranging between 250 to 70 nm between 5 to 65 MHz in water at room temperature[69]. Measuring at several overtones can also reveal if  $\Delta f$  and  $\Delta D$  have a frequency dependence due to viscoelastic influences by looking for increasing or decreasing overtone separation as changes occur in the adlayer[70], [71]. A practical rule of thumb for asserting whether a deposited film can be considered rigid or viscoelastic is to also consider the ratio of change in  $\Delta f$  and  $\Delta D$ , where an adlayer can be considered rigid if  $\Delta D_n / -(\Delta f_n/n) \ll 4e-7 \text{ Hz}^{-1}$ [65].

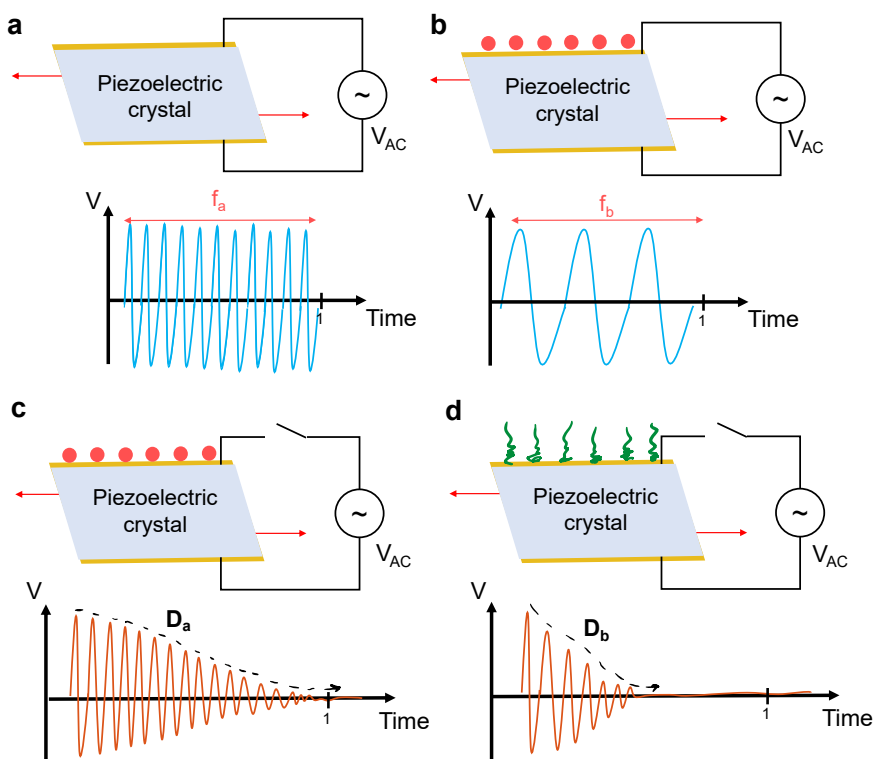


**Figure 3.6:** Basic principles of QCM-D. **a** Clean QCM-D crystal oscillating in shear mode at its resonance frequency,  $f_a$ , when an AC-voltage is applied to the contacts on either side of the piezoelectric material. **b** The same QCM-D crystal with rigid particles adsorbed to the surface yields a lower resonance frequency  $f_b < f_a$  due to the increased mass of the system. **c** When the AC-voltage is turned off, the oscillation eventually dies due to the energy dissipating to the surroundings with a given dissipation factor  $D_a$ . **d** If the adsorbed layer is viscoelastic or "soft", the energy dissipation will be higher due to higher losses in the system, resulting in a higher dissipation factor  $D_b > D_a$  compared to a more rigidly adsorbed surface layer.

### 3.2.1 Voigt model for viscoelastic layers

To better understand the mechanical properties of a viscoelastic layer, another model than the Sauerbrey equation must be used. One model described by Voinova *et al.*[69] is based on a mechanics approach where the viscoelastic layer is viewed as a continuous mass undergoing shear deformation. Mathematically this is achieved by treating the viscoelastic layer as a Voigt element (see Figure 3.7a), i.e. following the behaviour of a dashpot and a spring connected in parallel. Thus, both the viscous and elastic components' contribution to the stress/strain response from a resulting shear deformation is given by:

$$\sigma_{xy} = \mu \frac{\partial u_x(y, t)}{\partial y} + \eta \frac{\partial v_x(y, t)}{\partial y} \quad (3.19)$$

where  $\sigma_{xy}$  is the shear stress,  $\mu$  is the elastic shear modulus,  $\partial u_x(y, t)$  is the displacement in x-direction,  $\eta$  is the shear viscosity and  $\partial v_x(y, t)$  is the displacement velocity. From the wave equation of bulk shear waves we can further describe the displacement that occurs on the QCM-D crystal surface:

$$\frac{\partial^2 u_x(y, t)}{\partial y^2} (\mu + i\omega_d \eta) = -\rho \omega_d^2 u_x(y, t) \quad (3.20)$$

where  $\omega_d$  is the angular frequency of the displacement.

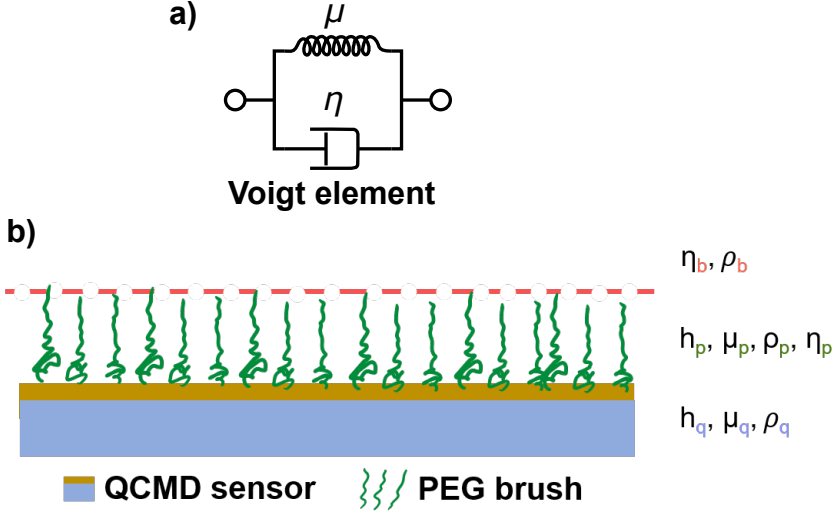


**Figure 3.7:** Schematic illustrations of **a)** Voigt viscoelastic element consisting of a spring and a dashpot connected in parallel. **b)** Parameters considered in Voigt modelling representing the relevant mechanical properties of the QCM-D sensor (**q**), grafted PEG layer (**p**) and bulk solution (**b**).

Combining equation 3.19 and the general solution of  $u_x(y, t)$  to equation 3.20 with no-slip boundary conditions[69] provides a description of  $\Delta f$  and  $\Delta D$  in terms of the mechanical properties of the QCM-D crystal, the viscoelastic adlayer and the bulk medium. In Figure 3.7b the case with a viscoelastic PEG brush in liquid is illustrated along with each layer's relevant parameters. The corresponding relations for  $\Delta f$  and  $\Delta D$  are given in equation 3.21 and 3.22 respectively.

$$\Delta f_n \approx -\frac{1}{2\pi\rho_q h_q} \left\{ \frac{\eta_b}{\delta_b} + h_p \rho_p \omega_n - 2h_p \left( \frac{\eta_b}{\delta_b} \right)^2 \frac{\eta_p \omega_n^2}{\mu_p^2 + \eta_p^2 \omega_n^2} \right\} \quad (3.21)$$

$$\Delta D_n \approx \frac{1}{2\pi f_n \rho_q h_q} \left\{ \frac{\eta_b}{\delta_b} + 2h_p \left( \frac{\eta_b}{\delta_b} \right)^2 \frac{\mu_p \omega_n}{\mu_p^2 + \eta_p^2 \omega_n^2} \right\} \quad (3.22)$$

where  $\omega_n = 2\pi f_n$  and  $f_n$  is the prior frequency value and the viscous penetration depth  $\delta_b$  is described as:

$$\delta_b = \sqrt{\frac{2\eta_b}{\rho_b\omega_n}} \quad (3.23)$$

Equation 3.21 essentially tells us how the interaction of three terms tied to the quartz crystal properties will affect its resonance frequency response to changes in any of the three layers. The first term corresponds to the liquid bulk properties and how far the acoustic wave penetrates into the bulk; the second term corresponds to the total mass loading from the adlayer; and the third term corresponds to the viscoelastic properties of the adlayer and its interactions with the bulk liquid. From the opposing sign of the viscoelastic term the dampening effect due to viscoelasticity also becomes apparent. From equation 3.22 we also see how the energy dissipation is more strongly governed by the viscoelastic properties of the adlayer and the bulk medium than the mass of the adlayer (still, there is some adlayer mass dependence via the frequency dependence that remains).

In order to utilise equation 3.21 and 3.22 for fitting against measurements of  $\Delta f$  and  $\Delta D$ , one would need to know all but two of the four adlayer parameters to determine the remaining unknowns. However, by using data from two or more overtone measurements when  $\Delta f$  and  $\Delta D$  has a significant frequency dependence more than two unknown parameters can be determined. Still, because there is no unique solution to  $\eta_p$  or  $\rho_p$ [71], at least one of these parameters must always be given. Due to the assumptions of the Voigt model, equations 3.21 and 3.22 are only applicable for polymer layers which are far from their glass transition regions, do not flow and conserve their shape[69].

### 3.3 Extinction spectroscopy of plasmonic nanoholes

Surface plasmons are not only found along the surface of thin smooth metal films, as was the case in the Kretschmann configuration discussed in section 3.1, but also waveguides or periodic gratings can be used to excite surface plasmons[58]. Metallic nanoparticles and nanostructures are also known to exhibit *localised* surface plasmon resonance (LSPR)[72]. Similarly to SPR, LSPR originates from collective oscillations of electrons, although, the geometrical limitations make the oscillations fully confined. This confinement leads to enhancement of their associated electric fields at the surface of the particle or structure. However, the sensing volume extending into the surrounding medium is typically one order of magnitude lower than conventional SPR[72]. Coupling to the highly localised plasmons can be achieved optically at a certain resonance wavelength, and for most metals the plasmon resonance is found within the visible spectrum of light. The resonance wavelength is determined by physical properties of the nanoparticles or nanostructures, such as their size, shape, periodicity, and optical and electronic properties. The localised plasmons are also sensitive to the refractive index of matter within their electric field, enabling highly localised refractometric sensing. Extinction spectroscopy can be used to measure how much light is absorbed and scattered (i.e. the extinction) after interacting with the LSPRs, revealing characteristic spectral features that shift upon changes in their properties. For example, plasmonic nanodisks are good examples of a nanostructure that show a refractometrically sensitive peak in the extinction spectrum due to their LSPR behaviour[73].

Plasmonic nanoholes arrays have also been found to demonstrate LSPR-like behaviour[12], [74]. Later developments have presented very similar nanopore array structures with slightly different geometries, such as nanohole arrays extending into the underlying substrate (known as "nanowells")[23], [75], or nanohole arrays spanning through thin membranes to connect different compartments (known as "nanopores")[24], [76]. Like nanodisks, a peak (maximum) in the extinction spectrum can be observed as a function of the periodicity of the holes[74], which was also observed to be refractometrically sensitive[12]. However, later work has pointed out that a secondary spectral

feature, an associated extinction minimum (or "dip") at higher wavelengths, is even more sensitive than the peak[77]. The same work also argue that the peak in the extinction is better described as surface plasmon polaritons excited via grating coupling as Bloch waves (where the nanohole array define the grating structure of the surrounding metal). This has later also been confirmed by others[78], [79]. The field extension of the plasmonic nanopore arrays was found to reach at most 40 nm away from the metal surface, which makes sensing more localised akin to LSPR sensors. At the same time, it is also found that the dip in extinction is more locally sensitive to the insides of the pore and is greatly affected by their properties, like shape and size. Furthermore, the dip is likely not simply due to the presence of the metal, but may rather be described as the result of Fano interference (a general wave phenomenon for certain resonating systems). Figure 3.8 demonstrates the principle of measuring the peak and dip of plasmonic nanoholes using extinction spectroscopy, and how the two spectral features show some differences in what regions they are more or less sensitive (note that this view is simplified). Tracking the peak and dip using centroid fitting algorithms has shown that refractometric performance similar to conventional SPR can be achieved in real-time[80].

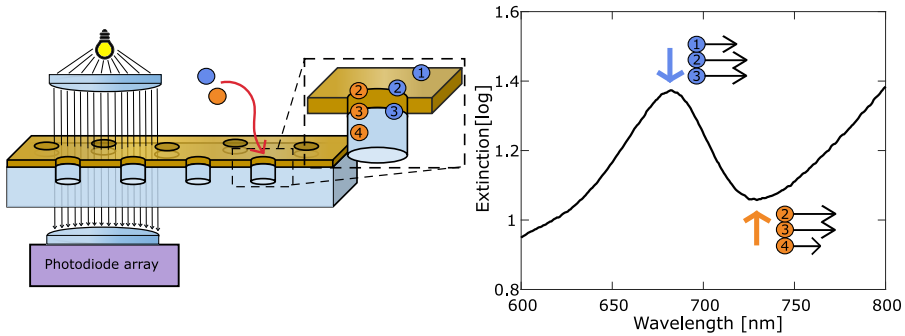


**Figure 3.8:** Principle of refractometric sensing with plasmonic nanoholes (here illustrated with nanowells). The extinction of white collimated light passing through a plasmonic nanowell sample is measured using a linear photodiode array spectrometer. The resulting spectrum gives two characteristic spectral features: a "peak" (blue arrow) and a "dip" (orange arrow). The two spectral features respond a bit differently to local changes in refractive index in the vicinity of the pore (here represented by particles 1-4).

The localised sensitivity of the dip has been experimentally demonstrated using nanowell structures and preferential binding of certain biomolecules to negative curvatures [75], [81]. Two scenarios that demonstrate the sensitivity is given in Figure 3.9, where the resonance shifts from tracking the extinction peak and dip is shown for different molecular binding conditions. Figure 3.9A show the response for 2 kg/mol mPEG-SH binding to the metal film surface outside and inside the nanopore. Shifts of similar magnitude can be observed during the binding process for both the peak and dip, since the molecules are binding where they both are highly sensitive. However, in Figure 3.9B a 20 kg/mol PEG brush has already been grafted to the metal surface and the metal inside the pore, which prevents an injected protein (avidin) from adsorbing close to the metal (and likely even repel most of the proteins outside the bulk sensitivity range). However, because the dip has higher sensitivity along the SiO<sub>2</sub> walls further inside the nanowell, a relatively high shift in the dip can still be observed.

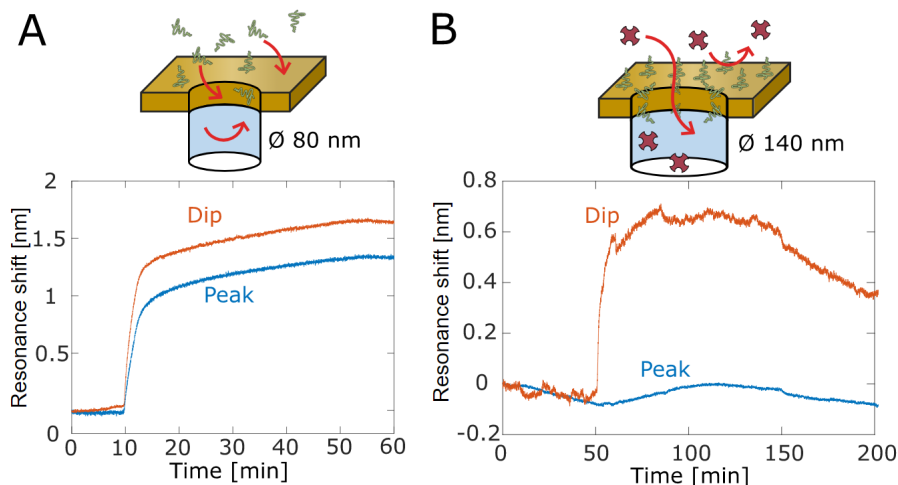


**Figure 3.9:** Tracked resonance shifts for peak and dip while binding molecules in nanowells and on the surrounding metal surface. (A) Binding of 2 kg/mol PEG to Au inside the 80 nm diameter nanowells and on the metal surface. Peak and dip shifts are similar in magnitude. (B) Avidin is injected on nanowells with 140 nm in diameter with pre-grafted 20 kg/mol PEG. The thick protein repelling barrier prevents proteins from being sensed close to the metal, while the dip is still sensitive to avidin adsorbing to the SiO<sub>2</sub> walls in the nanowells.

The main advantage of plasmonic nanostructures is not that they can provide superior sensing performance compared to conventional surface sensing systems, like SPR[82]. Rather, what warrants their use is their specific geometries, which define unique opportunities to answer questions for systems where this is relevant. For instance, independently being able to functionalise the different surface materials in such nanohole structures have been shown useful in understanding how molecules interact with nanoscale geometries[75], [83], [84]. They have also been demonstratively well suited to miniaturisation without losing much performance[85]. Thus, plasmonic nanopore arrays are likely to provide many contributions for understanding biomolecular interactions with nanostructures, and can function as an excellent tool directed towards future lab-on-a-chip and nanobiotechnological applications.



## CHAPTER 4

---

### Functional surface coatings

---

## 4.1 Surface cleaning and preparation

One of the most important things to consider when functionalising a surface is to make sure that the surface chemistry is compatible with the functional group of the attaching molecule of interest. While this may sound trivial in theory, in practice most surface materials will relatively quickly obtain an outer layer of various contaminants with unknown properties (although most of them tend to be organic) when exposed to ambient conditions. Even just nanometer thick contaminant layers may prevent the successful functionalisation of a surface, therefore it is important to use strong cleaning methods immediately prior to functionalisation. However, using too harsh cleaning methods may on the other hand be destructive to certain materials, or may cause lasting changes to the surface's chemistry. It is thus important to consider potential side-effects when choosing surface cleaning methods for all the different materials that are involved and how to mitigate such effects if necessary. This is of course especially relevant for advanced nanobiotechnological devices that potentially can include many different exposed components and materials.

There are some surface cleaning and preparation steps related to the work covered in this thesis that are worth mentioning. An example of a cleaning solution that is commonly used for efficiently removing organic contaminants is the mixture of  $\text{H}_2\text{O}:\text{NH}_4\text{OH}:\text{H}_2\text{O}_2$  at a 5:1:1 volume ratio heated to 75-80 °C, known as RCA-1 or "basic pirahna". While investigating palladium SPR sensors in **Paper 1**, RCA-1 was found to greatly alter the palladium film after cleaning, likely because of forming a palladium oxide layer. Collaborators who had worked with zero-mode waveguides made from Pd[86] suggested instead to use only hydrogen peroxide at a lower temperature of 45 °C followed by immersion in ethanol. This milder treatment performed better and the Pd remained compatible with the grafting of thiol-PEGs on the surface.

RCA-1 cleaning was also incompatible with the thin  $\text{SiO}_2$  film deposited on ordinary Au SPR sensors in **Paper 2**, as the  $\text{SiO}_2$  would delaminate without a dedicated adhesion layer. Instead, sonication in pure ethanol and a final UV/ $\text{O}_3$  treatment was found to be a very effective cleaning protocol, even allowing the  $\text{SiO}_2$  coated samples to be reused multiple times. It also prompted a new approach of cleaning PEG coated Au films. As observed in Figure 4.1,

it was found that UV/O<sub>3</sub> followed by ethanol immersion consistently removed more contamination from the Au surface compared to RCA-1 cleaning. A UV-induced oxidation mechanism of PEG has previously been suggested[87], [88], offering a potential explanation to why it may be more effective than heat induced oxidation. This change in cleaning procedure is likely what led to overall higher exclusion heights with lower variation for 20 kg/mol PEG brushes on Au in Figure 5A in **Paper 2** compared to Figure 1D in **Paper 3**.

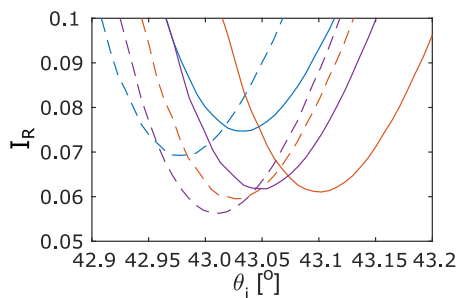


**Figure 4.1:** SPR resonance peaks for three Au sensors (blue, orange, purple traces) after cleaning 20 kg/mol PEG using RCA-1 (solid lines) or UV/O<sub>3</sub> (dashed lines).

## 4.2 Coating noble metals

Coating Au surfaces with functional layers using thiol chemistry has provided a wealth of technological opportunities[15]. The generally applicable grafting-to method of forming PEG brushes on Au surfaces[20] has also proven very useful and of high interest for future nanobiotechnologies[21], [22]. However, other noble metals perform better than Au in certain applications. Platinum has since long been used as a stable counter electrode for electrochemical applications[89]. Palladium is a cornerstone to organocatalysis in the pharmaceutical field[90], which is especially interesting for future lab-on-a-chip drug discovery applications. Palladium has also been identified as particularly interesting for single-molecule and biosensing purposes as the main component of zero-mode waveguides[86]. The possibility of directly characterising adlayer formation on these precious metals using SPR would thus be of great value for many

existing applications and for future nanobiotechnologies. Essentially, this is what was explored in **Paper 1**.

### 4.2.1 SPR characterisation of palladium and platinum coatings

Quantifying the sensor response from SPR measurements of Au sensors usually involves tracking or Fresnel model fitting of the distinct spectral feature of the plasmon resonance minimum. In principle, any part of the spectrum that changes predictably in both the measurement and model when a change is introduced to the system can be used to quantify the change. For example, we found that the region around the inflection point (represented by the minimum in the derivative of the decreasing reflectivity) for Pd and Pt films was sensitive to refractive index changes and could be utilised for fitting and tracking (see Figure 4.2A). Indeed, the same conclusion has previously been made for SPR measurements of Pd in air[91].

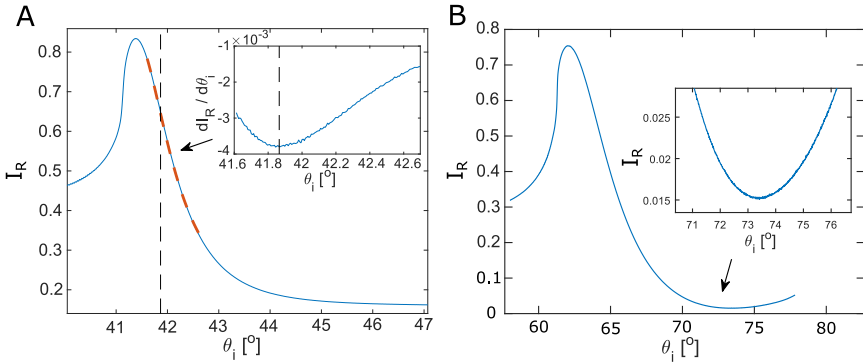


**Figure 4.2:** SPR measurements of a 20 nm Pd sensor in (A) air and (B) liquid.

In liquid, SPR measurements of Pd and Pt produced the more familiar plasmon resonance dip in the reflectivity spectrum similar to conventional Au film sensors (Figure 4.2B). However, the dip was at least 10 times broader for both metals. Regardless, it was still possible to track shifts in the dip with a simple

second-degree polynomial (third-degree also works well) following the response of an adlayer binding to the surface with decent noise levels and sensitivity. On the other hand, we could not get consistent results for the non-interacting probe method (see section 3.1.3), hence why no such results are included in **Paper 1**. One part of the problem may be the significantly lower sensitivities spread over relatively large decay lengths (see Figure 4 in **Paper 1**) and that this gives too low resolution between the two states of presence or absence of the molecular probe. Another reason could be that the Fresnel model fitting procedure would need to be further optimised to ensure more consistent fits with the broad features in the spectra.

### 4.2.2 PEG brushes on palladium and platinum

In complex biological solutions different adsorbates are present that may affect the outcome of electrochemical reactions at an electrode interface[55]. An increasing surface coverage of adsorbates may not only reduce available sites for the desired electrochemical reactions, but may also contribute with parasitic reactions that obfuscate the signal of interest or produce unwanted side-products. Similar reasoning also holds true for using noble metals for organocatalysis applications. Thus, being able to use PEG brushes to prevent non-specific interactions with Pt and Pd can provide significant advantages within many of their liquid applications.

Real-time *in situ* SPR measurements of coating Pd and Pt with a small mPEG-SH (2 kg/mol) at 1 g/L in PBS buffer are demonstrated in Figure 3 in **Paper 1**. After the initial PEG injection, three subsequent injections of high concentration (10 g/L) solutions of the protein bovine serum albumin (BSA) show no sign of detectable adsorption. The difference in responses during PEG grafting between Pd and Pt can at least partly be attributed to differences in sensitivity. Another possible explanation is that partial oxidation after the cleaning procedure may happen to varying degree for the two metals, thus affecting the availability of reduced metal groups when forming metal-thiol bonds. Following later developments in grafting PEG brushes to SiO<sub>2</sub> surfaces in **Paper 2**, comparisons of 2 and 20 kg/mol mPEG-SH grafted in 0.9 M Na<sub>2</sub>SO<sub>4</sub> to four different material surfaces (including Pd and Pt) can be found in Figure 4.6 in section 4.3.2.

### 4.3 Coating silicon dioxide

Silicon dioxide ( $\text{SiO}_2$ ) is a common material choice for micro- and nanofluidic devices towards bioapplications largely because of its compatibility with established silicon-based fabrication technologies, easily modifiable surface properties and high biocompatibility[92]. Chemical functionalisation of  $\text{SiO}_2$  becomes relatively straight forward because of the abundance of  $-\text{OH}$  groups on the surface that can be targeted by other functional groups. Negatively charged  $-\text{O}(-)$  groups can also be utilised to adsorb molecules electrostatically. Silanes are among the most popular anchoring groups because of the formation of strong siloxane bonds ( $-\text{Si}-\text{O}-\text{Si}-$ ), however, they are also known to be highly moisture sensitive and may readily polymerise and form precipitates in solution due to hydrolysis in the presence of water[15]. Recent use of hydrolytically stable *silatrane*s have shown promise as an alternative to silanes, as they are able to form thin and smooth layer binding to  $\text{Si}-\text{OH}$  surfaces directly from solution [93]–[96].

Similarly to metal films, antifouling polymer brush coatings that resist non-specific biomolecule adsorption on silicon dioxide is of wide interest for many biotechnological applications. One of the most successful grafting-to approaches for negatively charged metal oxide surfaces is the use of the block copolymer PLL-g-PEG[97], [98]. The positively charged polyelectrolyte backbone of poly(l-lysine) (PLL) readily adsorbs flatly onto negatively charged surfaces, forcing the grafted side-groups of PEG to stretch out in solution and form a comb-like PEG brush at the surface. However, while the grafting conditions used for PLL-g-PEG is compatible with nanobiotechnological devices, because it is not covalently bound to the surface it becomes more vulnerable to desorption in some cases[99]. For example, we found that PLL-g-PEG partly desorbs from atomic layer deposited  $\text{SiO}_2$  when injecting a surfactant or applying high shear flow rates (see Supporting information in **Paper 2**).

In **Paper 2**, several surface sensitive techniques were used to investigate the potential of 3-aminopropylsilatrane (APS) as a functional anchoring group on  $\text{SiO}_2$  surfaces. Furthermore, the APS layer is used together with an amine-thiol crosslinker to enable covalently click-point grafted PEG brushes using the same mPEG-SH as previously used for metals. The following subsections describe the full functionalisation approach on planar surfaces, and in sec-

tion 5.2 it is also applied to two different nanostructures to demonstrate its nanobiotechnological compatibility.

### 4.3.1 Surface amination using 3-aminopropylsilatrane

Amino-terminated silanes like (3-Aminopropyl)triethoxysilane (APTES) has become the golden standard in functionalising  $\text{SiO}_2$  surfaces for a wide variety of applications[100]. However, as previously discussed, there are some inherent issues with silanes that limits their practical use to anhydrous or humidity-free environments. APS is the silatrane most closely resembling APTES in molecular structure (see Figure 4.3). The presence of the trans-annular bond between the Si and N atoms in silatranes, such as APS, is thought to explain its very low hydrolysis rate in water due to the increase in electronegativity of the Si atom[101].

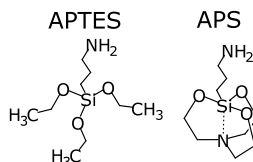


**Figure 4.3:** Molecular structures of APTES and APS.

In **Paper 2**, the functionalisation of  $\text{SiO}_2$  with APS was studied using several surface sensitive techniques. SPR was used to determine the APS layer thickness using Fresnel models (see section 3.1.2) and also to investigate how various incubation parameters affected the thickness. It became clear that the initially adsorbed APS was greatly affected by the polarity of the solvent used for incubation and rinsing. Figure 4.4A shows how the initial APS surface layer thickness (at time 0) is affected by the polarity of the solvent used to rinse off excess APS incubation solution ( $460 \mu\text{M}$  in 99.4 % EtOH). The higher the polarity of the rinsing solvent, the more of the APS layer is rapidly desorbed from the surface at this stage. Immersing the APS coated surfaces in pure MQ-water for different periods of time demonstrates a relatively fast APS surface desorption below monolayer coverage. This effect seems the high-

est if the sample has not been cured after rinsing (orange trace). Curing for only 60 seconds at 75 °C infers a significant stability against surface desorption and/or hydrolysis in MQ-water in comparison to uncured samples. This suggests the adsorption mechanism of APS is similar to that of APTES, whose initial adsorption is mediated via hydrogen-bonding (or electrostatics), followed by slower siloxane bond formation that is rapidly increased while the surface is cured[102]. A step-by-step mechanism for how a similar thiol-terminated silatrane can break up following surface adsorption and undergo hydrolysis to form siloxane bonds has previously been proposed[103].

The effect of concentration and incubation solvent polarity on the APS thickness evolution with incubation time is presented in Figure 4.4B. It is clear that the formation of a monolayer is rapid at 460  $\mu\text{M}$  APS in EtOH, as rinsing away the APS solution with 95 % EtOH already after 3 seconds still gives a 0.8 nm APS layer after curing and rinsing with MQ-water. However, at longer incubation times at this high concentration, multilayers of APS readily start to form. Decreasing the concentration four-fold to 115  $\mu\text{M}$  appears to significantly reduce this effect, and 0.8 nm thick layers are readily formed after 60 second incubation. We can also see that, although the APS is hydrolytically stable in water solutions, it does not completely cover the surface to form complete monolayers even after long incubation times. Liquid real-time SPR measurements of injecting APS on  $\text{SiO}_2$  further reveals that, while the APS is able to barely reach full monolayer coverage during injection, a significant portion desorbs as soon as rinsing with buffer starts (see Supporting information in **Paper 2**). In conclusion, the solubility of APS in water appears too high to allow for adsorbing complete APS layers on the  $\text{SiO}_2$  surfaces used in this study. While this is detrimental to some functionalisation applications, adsorption of lower densities of larger particles or macromolecules should still be feasible (as has been previously shown for other substrates[95], [96], [104]).

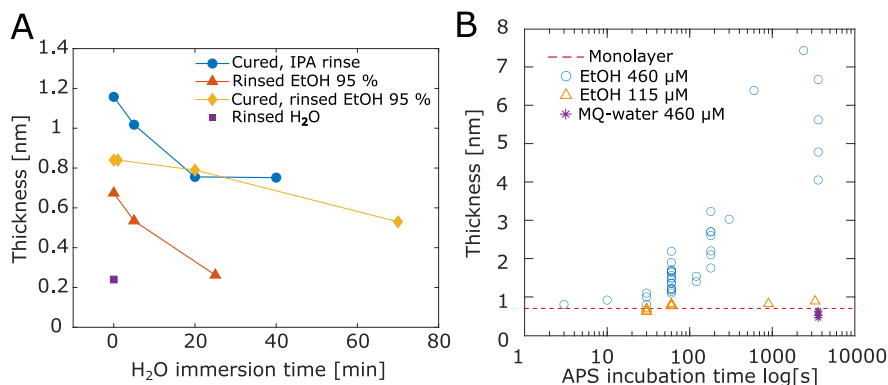


**Figure 4.4:** SPR determined thickness of APS after following different incubation conditions. (A) An initial APS layer was formed by incubation at 460  $\mu\text{M}$  in 99.4 % EtOH for 60 seconds. Different solvents were then used to immediately rinse the excess APS solution (indicated by the different traces) and curing was performed (or not). Surfaces were then dried and an initial thickness was determined in air (at time 0). Finally, the surfaces were immersed in MQ-water for different amounts of time before being dried and re-measured. (B) APS layer thickness as a function of incubation time at different concentrations in 99.4 % EtOH or pure MQ-water. All samples were rinsed in 95 % EtOH, cured then rinsed with MQ-water. The red dashed line corresponds to a theoretical monolayer at 0.7 nm thickness.

Atomic force microscopy (AFM) and X-ray photoelectron spectroscopy (XPS) were also employed to investigate the APS layer's influence on surface roughness and confirm its presence chemically (AFM and XPS measurements were performed by the collaborators Chonnipa Palasingh and Andreas Schaefer respectively). From Figure 2 in **Paper 2** we can observe an interesting difference in the resulting surface roughness between using APTES or APS to functionalise the SiO<sub>2</sub> surface. The slight increase in surface roughness after APTES deposition suggests that the adsorbed molecules follow the roughness of the surface, as expected. Interestingly however, APS coating leads to a *decrease* in surface roughness of the initial substrate, even when adsorbing the same mass as APTES (corresponding to 0.8 nm optical thickness as per SPR measurements). This "smoothing effect" suggest that the cage-like structure of the silatrane with lower degrees of orientational freedom (compared

e.g. to the three ethoxy groups of APTES) preferentially adsorbs in the valleys instead of the peaks of the surface roughness. Immersing a sample in PBS for 10 minutes before curing (Figure 2C in **Paper 2**) desorbs some of the initial APS and the surface roughness decreases even further. This can be explained in terms of the high solubility of APS in a polar solvent, where the APS adsorbed further up on roughness peaks will be exposed to the solvent to a larger extent and are thus the first to desorb. This suggests an interesting application to chemically "polish" a surface without abrasion (avoiding particulate formation) using silatranes with a terminal group matching the functional groups of the substrate surface. Such a polishing method would in principle also be able to polish non-flat geometries in nanostructures.

### 4.3.2 PEG brushes on silicon dioxide

Introducing primary amines to the surface of SiO<sub>2</sub> provides more options for further surface functionalisation. For example, N-hydroxysuccinimide carbonate groups can be used to couple molecules to primary amines via formation of stable amide bonds[105]. In **Paper 2**, the amine-thiol crosslinker sulfosuccinimidyl 4-(N-maleimidomethyl)cyclohexane-1-carboxylate (Sulfo-SMCC) was introduced to APS coated surfaces to enable grafting of the same type of mPEG-SH (both 2 and 20 kg/mol) as was used on metal surfaces in **Paper 1**. The maleimide group that remains free after initially binding Sulfo-SMCC to the primary amines of the APS layers should in principle be able to bind to thiols in aqueous solutions of a pH between 6.5-7.5 (according to the chemical supplier of Sulfo-SMCC). While the solubility of Sulfo-SMCC is relatively low in salt concentrations above 50 mM (as per the supplier), it was hypothesised that surface-bound maleimides could still be compatible with the Na<sub>2</sub>SO<sub>4</sub> cloud-point grafting method described in section 2.2.1. Figure 4.5 describe two similar grafting protocols to graft dense APS-SMCC-PEG polymer brushes to SiO<sub>2</sub> surfaces. Solutions of APS at 115 µM in 99.4 % EtOH, Sulfo-SMCC at 0.5 g/L in 10 times diluted PBS buffer and grafting solutions of 0.9 M Na<sub>2</sub>SO<sub>4</sub> with 2 kg/mol mPEG-SH at 1 g/L or 20 kg/mol mPEG-SH at 0.12 g/L respectively were used.

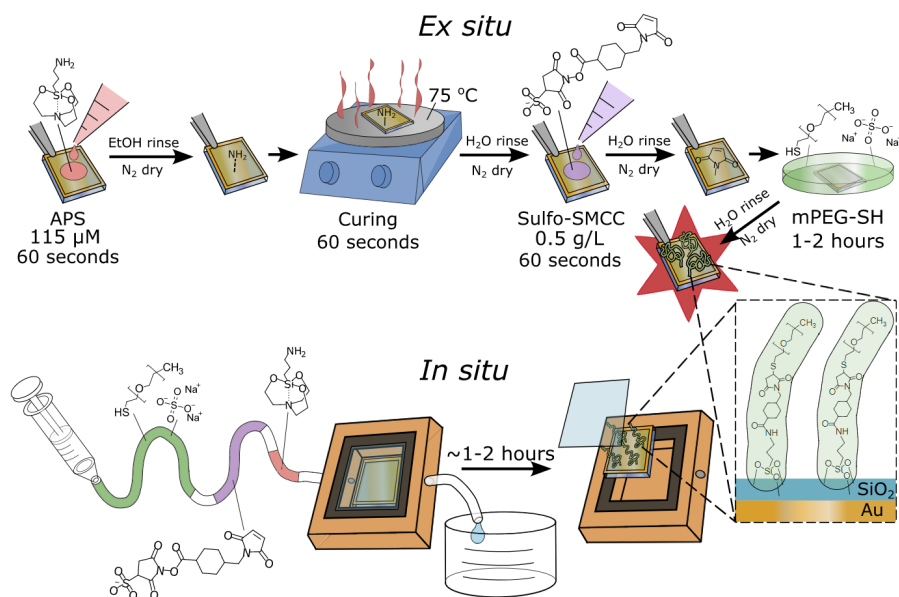


**Figure 4.5:** Schematic illustration of the *ex situ* and *in situ* approaches of producing APS-SMCC-PEG layers on SiO<sub>2</sub>.

The *ex situ* functionalisation approach allowed us to accurately quantify the thickness of each added surface layer in a step-wise manner using Fresnel modelling of SPR measurements (section 3.1.2). Figure 4.6A presents a comparison in measured layer thickness and exclusion heights for the same two PEG batches of 2 or 20 kg/mol, cloud-point grafted from the same prepared solutions to both Au or APS-SMCC functionalised SiO<sub>2</sub>. Firstly, the estimated layer thickness after exposing an APS coated surface to Sulfo-SMCC was closely matching the theoretical length of the amine coupled SMCC spacer arm (0.82 nm), assuming its refractive index is similar to APS. The C 1s and N 1s peaks measured with XPS (Figure 3C of **Paper 2**) also chemically confirmed the presence of an APS-SMCC layer and high degree of reaction inferred from the low sulphonate signal (see Figure S7 in S.I. of **Paper 2**). With regards to PEG, one can see that the dry mass of PEG on SiO<sub>2</sub> is lower compared to Au for both molecular weights. Interestingly however, the exclusion heights appear much more comparable and even higher for 2 kg/mol PEG

on SiO<sub>2</sub> (but essentially equal after subtracting the APS-SMCC thickness). This result suggests that the additional mass of PEG on the Au surface likely does not contribute to forming an extended brush. The additional amount of PEG is instead likely adsorbed or partly entangled along the solid surface. New dry thickness measurements (Figure 4.6B) on Pd and Pt for 2 and 20 kg/mol mPEG-SH grafting in 0.9 M Na<sub>2</sub>SO<sub>4</sub> and a similar cleaning protocol as used in **Paper 2** reveals that similar amounts of dry PEG mass are obtained for all three tested metal surfaces. Essentially, this may put into question the standard way of determining grafting density based on assuming all of the adsorbed dry mass contributes to forming a polymer brush (see equation 3.15). Regardless, the results in Figure 4.6 demonstrates the closely matching properties of PEG brushes on SiO<sub>2</sub> compared to noble metals prepared using the *ex situ* protocol described in Figure 4.5.

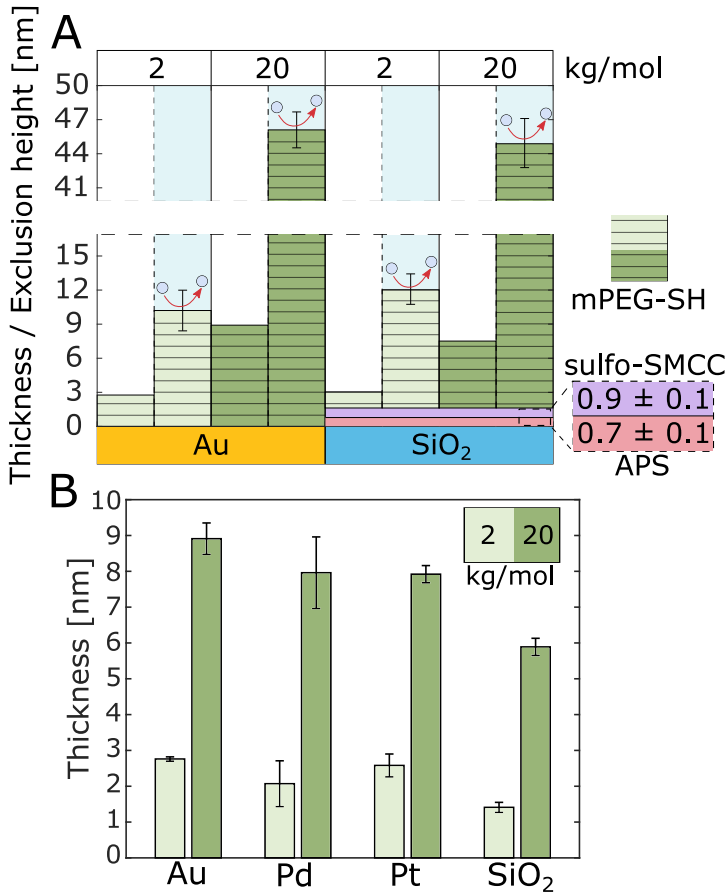


**Figure 4.6:** Comparison of SPR determined thickness values for 2 and 20 kg/mol PEG layers. (A) on Au and SiO<sub>2</sub>, the latter grafted according to the *ex situ* protocol. Both dry layer thickness and exclusion heights determined with the non-interacting probe method in liquid (the latter indicated by the repelling probe) are presented. The standard deviation for dry thicknesses were  $\approx 0.1$  nm and error bars on exclusion heights represent deviation from the measurement mean within a 99 % confidence interval. (B) Including new dry thickness results (outside **Paper 1**) for Pd and Pt, plotted together with the results in (A) on Au and SiO<sub>2</sub>. The same cleaning procedures and PEG grafting solution conditions were used for all four surfaces.

The *in situ* approach of grafting APS-SMCC-PEG brushes on SiO<sub>2</sub> was evaluated using both SPR and QCM-D (see Figure 4.7). The main difference with this grafting approach is that the curing step after APS is skipped, as are all drying steps. After rinsing out an initial injection of APS in EtOH at 460  $\mu$ M, we can see that a multilayer initially formed, since the SPR response in Figure 4.7A is above red dashed line while the TIR response show that the solution has exited the flow cell. Upon rinsing with aqueous buffer rapid desorption of APS can be observed. However, note that after finishing the injection of Sulfo-SMCC the APS-SMCC layer appears stable (see **Paper 2** for further discussion). Thus, curing does not appear necessary as long as Sulfo-SMCC is introduced before too little APS remains. Despite the clear excess of APS-SMCC, cloud-point grafting mPEG-SH still appears viable, as shown by testing the antifouling properties with three injections of 10 g/L BSA. The exclusion height from the experiment in Figure 4.7A was measured to be  $\approx$  1.2 nm larger on average compared the thinnest possible APS-SMCC layer as shown in Figure 4.6, likely due to the excess APS-SMCC that was often obtained when grafting *in situ*.

To test the functionality of the APS-SMCC-PEG grafting approach, two types of properties were further evaluated with SPR: antifouling properties and biomolecular recognition. The full results regarding these aspects are presented in Figure 6 and 7 in **Paper 2**, however, Figure 4.8 essentially also demonstrate them both. The avidin-biotin interaction is commonly used to selectively conjugate biotinylated molecules together using the protein avidin as a linker[106]. This strategy has previously been applied to PLL-g-PEG functionalised metal oxide surfaces to make them selectively protein binding[107], and here we adopt this same approach with biotin-PEG-SH. By mixing biotin-PEG-SH and mPEG-SH such that around 17 % of the polymer chains in the grafting solution are biotinylated, a high selectivity and non-specific binding ability of the surface can be maintained (as shown previously for PLL-g-PEG[107]). Figure 4.8 show injections of 10 times diluted adult bovine serum on a 17 % APS-SMCC-PEG-biotin brush, provoking only a weak response, while injections of the same serum with added avidin (0.1 g/L) show a high amount of selective avidin binding. The higher amount of avidin binding in serum compared to purely avidin (Figure 7B in **Paper 2**) is likely because of non-specific adsorption *to avidin*. This may potentially be avoided by instead using the (more expensive) deglycosylated version known

as NeutrAvidin that is known to exhibit less non-specific adsorption[108].

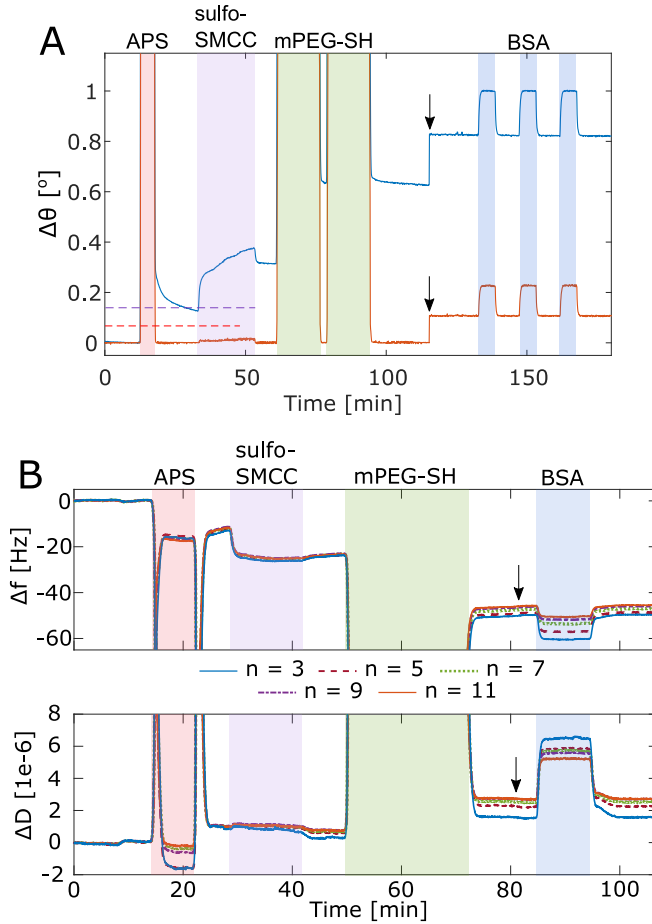


**Figure 4.7:** Examples of the *in situ* grafting approach for 2 kg/mol PEG on (A) SPR and (B) QCM-D. The black arrow denote running buffer switch from 10 times diluted PBS to normal PBS (white parts corresponds to buffer). The following solutions were used: 460  $\mu\text{M}$  APS in 99.5 % EtOH, 2 g/L Sulfo-SMCC in 10 times diluted PBS and 1 g/L 2 kg/mol mPEG-SH in 0.9 M  $\text{Na}_2\text{SO}_4$ . The dashed red and purple lines in (A) corresponds to the theoretical monolayer amount of APS and SMCC respectively.

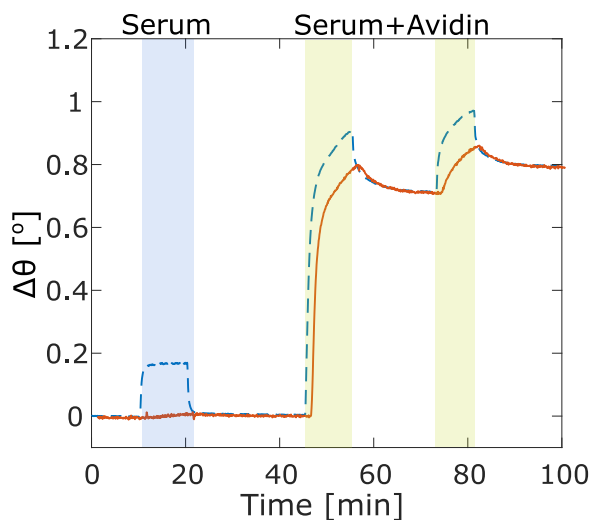


**Figure 4.8:** Serum experiments on a mixed biotin-PEG-SH brush (17 % biotin-PEG, 83 % mPEG-SH, both  $\approx 2$  kg/mol). The blue dashed trace corresponds to the SPR angle shift, while the orange trace shows the bulk compensated response (described in our recent work[62]).

The "elephant in the room" of our protocol for grafting APS-SMCC-PEG brushes on  $\text{SiO}_2$  is perhaps: why not do a one-pot approach and bind the full APS-SMCC-PEG conjugate from solution? We foresee some practical uncertainties that first have to be tested (e.g. will the silatrane group be able to initially adsorb to the  $\text{SiO}_2$  surface in 0.9 M  $\text{Na}_2\text{SO}_4$ ?). There are two main reasons why we opted for a multi-step approach to start with: 1) To evaluate the performance of APS in detail, where step-wise characterisation also provides valuable insight for others interested in conjugating different molecules to APS surfaces. 2) The exact same polymer batch can (in principle) be grafted to both metals and oxides simultaneously, providing matching polymer brush properties between different materials in one approach. To properly put this last point to the test, an interesting future study could look at applying the APS-SMCC-PEG approach to partially oxidised metal surfaces. For example, partially oxidised palladium may be a good system to test this by controlling the degree of oxidation in pre-treatment processes or electrochemically[109].

## 4.4 The pH responsive PEG-PMAA system

While PEG brushes offer a simple solution to reduce non-specific protein adsorption, they are not particularly stimuli-responsive on their own, which limits their functionality for some nanobiotechnologies. However, as discussed in section 2.5, the interpolymer complex formation of PEG with polyacids in low pH solutions provide a possible multivalent interaction mechanism for making a PEG brush respond in a stimuli-responsive manner. In **Paper 3**, the interaction between a cloud-point grafted mPEG-SH brush (see section 2.2.1) and PMAA (5.4 kg/mol, 0.1 g/L) was studied using surface sensitive techniques to investigate whether the PEG brush properties are affected by the interaction, and if so, to what degree.

Studying the PEG-PMAA interaction using SPR revealed a number of interesting things, and in Figure 4.9 a typical experiment is presented. A clear difference is observed in the signal response between injecting PMAA at neutral pH 7.5 or low pH 4.5, which can be explained by the difference in degree of protonation of PMAA at the different pH:s. Indeed, we found a critical pH value around 5 (see Figure S1 in **Paper 3**), below which interactions between a PEG brush and PMAA in solution rapidly grew stronger and lead to more adsorbed PMAA. The adsorption of PMAA was also found to be practically irreversible after rinsing with a pH 4.5 solution, but when switching to neutral pH most of the PMAA desorbs from the surface as indicated by the drop in  $\Delta\theta_{SPR}$  and establishment of a new baseline. Clearly, not all of the adsorbed PMAA leaves the surface, and the amount remaining can most likely be attributed to Au surface adsorption (or part Au part PEG), as indicated by controls on pure Au (see Figure S5 in **Paper 3**). The exclusion height was probed with the non-interacting probe method on the initial PEG brush, on the PEG-PMAA layer at low pH and after rinsing PMAA with pH 7.5. This showed (see Figure 1 D and E in **Paper 3**) that the PEG-PMAA layer shrinks in height continuously by maximum  $\approx 12$  nm, despite that a significant amount of additional mass is being added and that the polymer brush height doesn't seem affected by the remaining amount of PMAA after pH 7.5 rinsing.

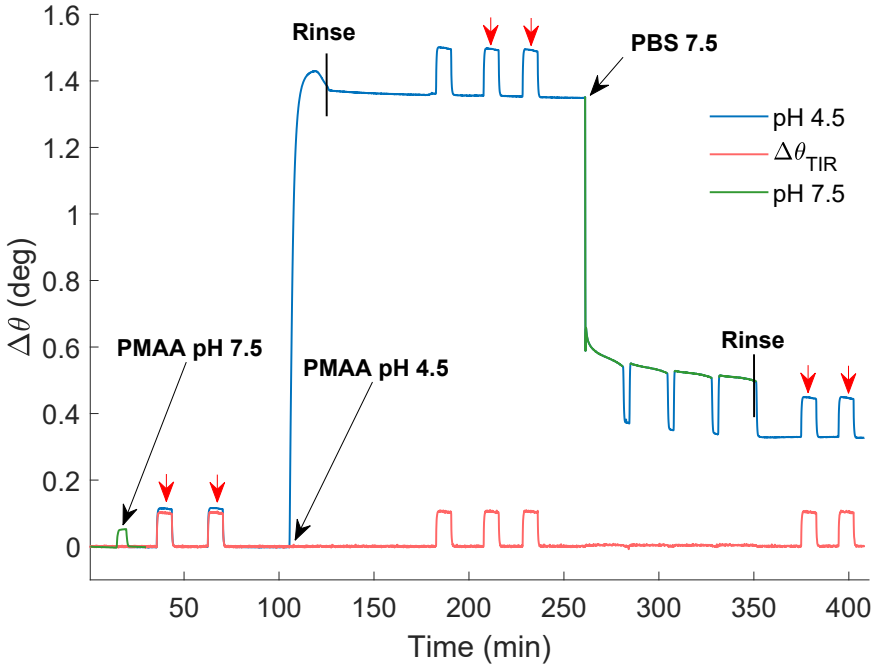


**Figure 4.9:** Typical SPR response when injecting PMAA on top of a PEG brush at neutral (green trace) and low pH (blue trace). The red trace is corresponding to bulk change via  $\Delta\theta_{TIR}$ . Red arrows show non-interacting height probing injections with dextran (a carbohydrate) as probe. Reproduced with permission from the author's Licentiate thesis work[14].

Performing complementary measurements of the same process using QCM-D provided some additional insights to how the PEG brush was affected by the PEG-PMAA interaction, where an equivalent QCM-D experiment to Figure 4.9 is presented in Figure 4.10. Upon adsorbing PMAA to a PEG brush at pH 4.5, the a positive frequency shift is observed for most overtones while the dissipation shift is negative. This suggests that we are *losing* net mass from the adsorbed layer in the form of coupled solvent and that it becomes very rigid ( $\Delta D = 0$  corresponds to an empty QCM-D crystal). The convergence of the overtones is another tell for increased rigidity, as the frequency dependent dampening induced by the presence of a viscoelastic layer is removed for

very high shear modulus, as that of increasingly rigid layers (see third term in equation 3.21). Indeed, modelling the acoustic thickness and viscoelastic properties using the Voigt model reveals that the layer thickness significantly drops and that the viscosity and shear modulus vastly increase during PMAA injection. Therefore, the Sauerbrey equation is a more suitable model while PMAA is adsorbed at low pH. The PEG brush properties are then restored after rinsing with high pH, as also observed in SPR.

During initial non-interacting probe measurements it was clear that the PEG-PMAA layer was binding the typical protein probe for PEG brushes (bovine serum albumin[64]), which is why we instead opted for the carbohydrate dextran as a probe. Additional SPR measurements of adsorbing PMAA in a step-wise fashion (see Figure 4 in **Paper 3**) also revealed that the protein interactions start only after a certain amount of PMAA has adsorbed and that rinsing with pH 7.5 retains the antifouling properties of the PEG brush.

All in all, it was found that the properties of the PEG brush was highly affected by the interactions with PMAA in terms of its morphology, rheology and protein interactions as a function of solution pH in a stimuli-responsive manner. Thus, the PEG-PMAA interaction is highly interesting for potential nanobiotechnological applications, such as molecular recognition of PMAA tagged nanoparticles or turning on and off the protein repulsion of a surface on demand. The height change observed by the layer may be a useful actuating mechanism for gating macromolecules on PEG covered nanopores (see preliminary results in section 5.2.2).

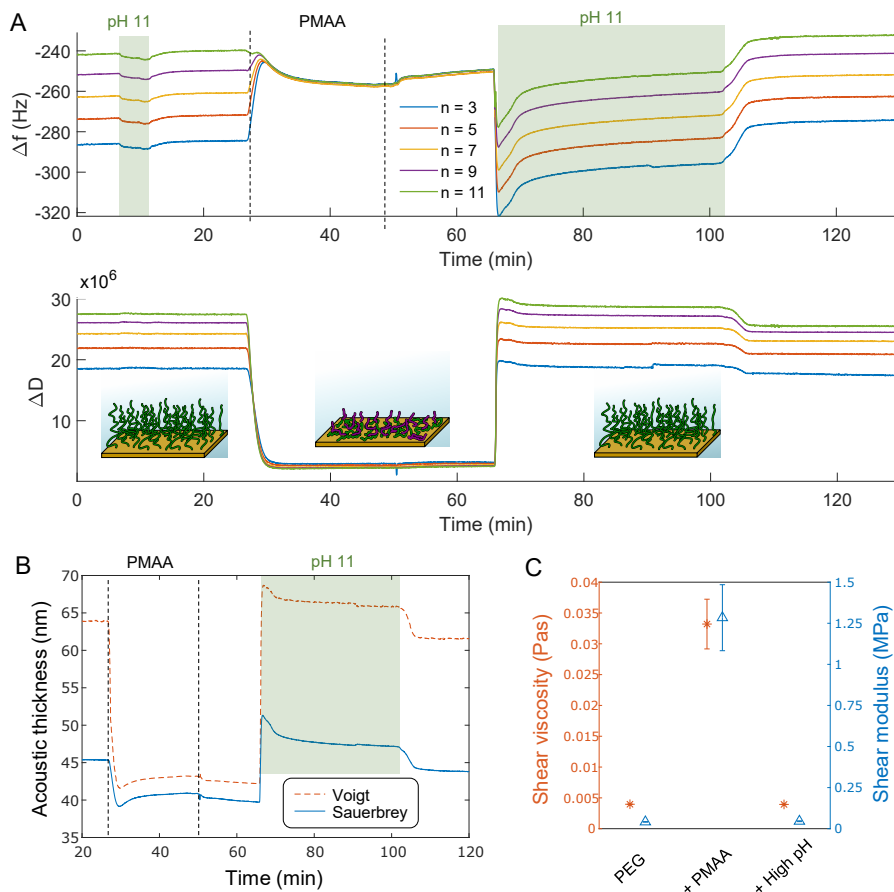


**Figure 4.10:** QCM-D response and change in polymer brush properties during PEG-PMAA interaction at low (4.5) and high (11) pH. (A) Frequency and dissipation shifts relative to an empty QCM-D crystal at 5 different harmonics upon injection of PMAA at low pH and high pH rinsing. (B) Acoustic thickness modelled as a rigid or viscoelastic layer using the Sauerbrey relation or Voigt model respectively (assuming a layer density of  $1100 \text{ kg/m}^3$  in both cases). (C) Viscoelastic change in terms of shear viscosity and shear modulus obtained from the Voigt model. Error bars correspond to doubled standard deviation. Reproduced with permission from the author's licentiate thesis work[14].

## **4.5 Unpublished work: Electrochemically controlled PEG brush actuation**

There are some inherent issues with exchanging the whole bulk liquid pH to change polymer brush properties via the PEG-PMAA interaction. Only biomolecules that are stable at both neutral and slightly acidic pH 4 and above can be involved in a process relying on this system, which limits the application scope. In addition, liquid chambers with complicated geometries may suffer from poor bulk exchange and may have local pockets of prior solutions that linger longer than expected, leading to irregular behaviour. One solution to these issues is to generate a local pH gradient originating at the surface where the PEG-PMAA interaction occurs, minimising the pH change in the buffered bulk solution. This kind of localised pH control has been achieved using electrochemical oxidation of proton-donor molecules in solution[56], [110], [111]. Hydroquinone is one example of a well studied proton-donor, which upon oxidation at positive potentials convert to benzoquinone and release two electrons and two protons[56]. The buffering strength of the solution acts as a counteracting balance to the pH decrease determined from the oxidation rate of hydroquinone (reflected in the measured current), which together tune how localised the pH decrease becomes[56], [111]. Here this concept is applied to the PEG-PMAA interaction discussed in section 4.4 and studied using electrochemical QCM-D (EQCM-D) and electrochemical SPR (ESPR). A schematic illustration of the overall system is presented Figure 4.11).

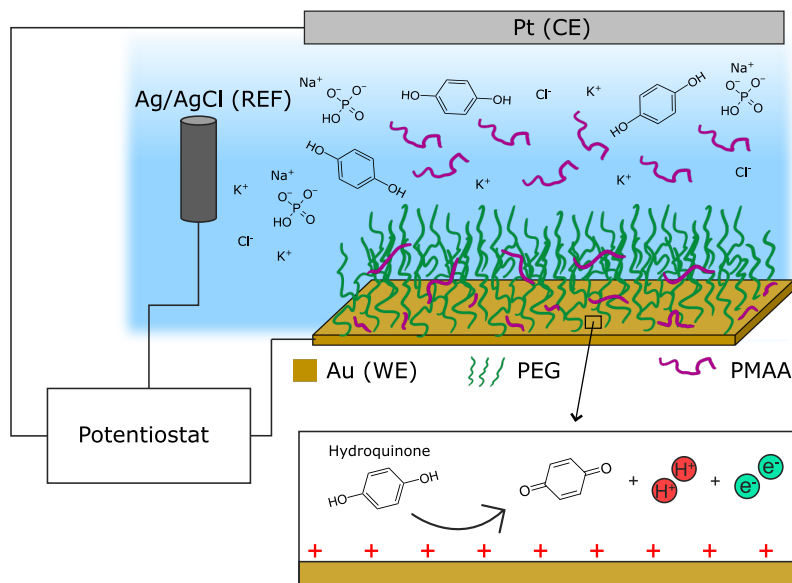


**Figure 4.11:** Schematic illustration of the experimental setup and electrochemical principal for controlling the PEG-PMAA interaction. A local pH decrease can be generated from hydroquinone oxidation at positive potentials in a fully PBS buffered pH 7.5 bulk solution.

The response of a PEG brush to applying positive potentials in the presence of 5 mM hydroquinone, 0.1 g/L PMAA (5.4 kg/mol) and PBS buffer at pH 7.5 was measured with both EQCM-D and ESPR in Figure 4.12. Immediately upon applying a positive potential, the frequency and dissipation responses in Figure 4.12A shift in a way that closely resembles changing the bulk pH in the presence of PMAA (see Figure 4.10). The shift towards smaller acoustic thickness in both the Voigt and Sauerbrey models confirm that the PEG brush properties has changed and that they go back to their original state after turning off the applied potential. We can also note a dependence on the potential difference, confirming that it is possible to vary the rate of proton generation and attain different stable local pH equilibria. ESPR (Figure 4.12B) further confirms the adsorption of PMAA from solution while applying a potential and that a portion of the adsorbed amount sticks irreversibly also at neutral pH, as observed for bulk pH injections in Figure 4.9.

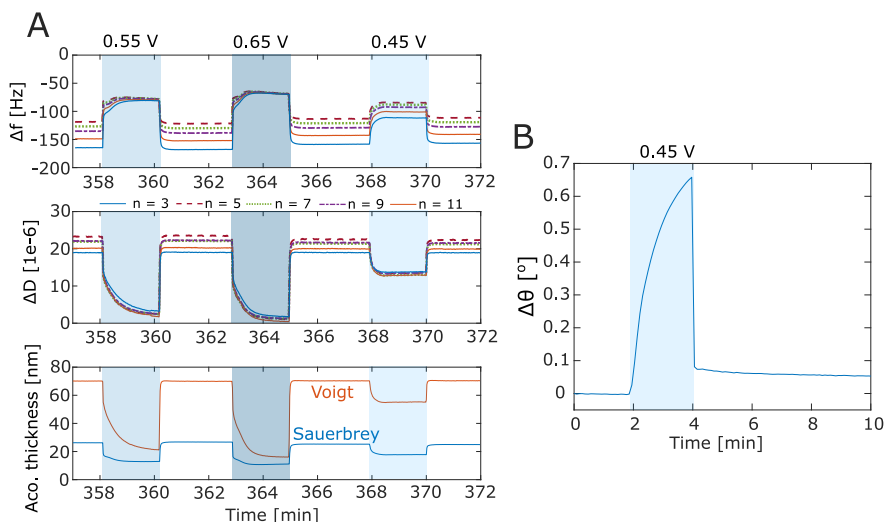


**Figure 4.12:** Signal responses in (A) EQCM-D and (B) ESPR after applying positive potentials with 5 mM hydroquinone and 0.1 g/L PMAA (5.4 kg/mol) in PBS.

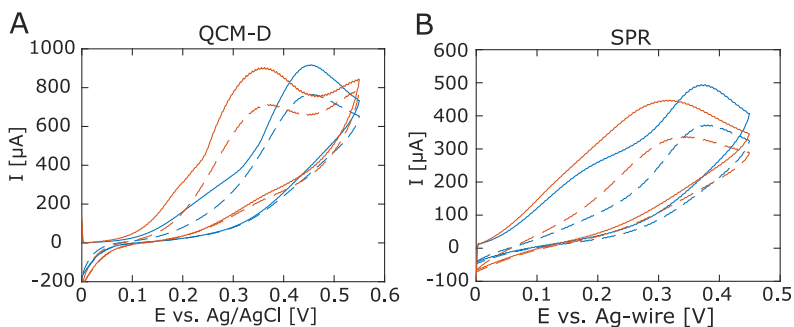


**Figure 4.13:** Cyclic voltammograms with 30 mV/s scan rate during oxidation of 5 mM hydroquinone in PBS on a PEG coated Au surface, performed in electrochemical flow cells for (A) EQCM-D and (B) ESPR. The blue traces correspond to negligible PMAA (5.4 kg/mol) presence in the brush layer and on the surface, while the orange trace denotes after PMAA saturation on the solid surface. The dashed lines corresponds to a secondary sweep immediately after the first one.

Cyclically sweeping the magnitude of the applied potential and measuring the resultant current can provide information about redox reactions occurring at the working electrode. Figure 4.13 present cyclic voltammograms of a PEG brush in the presence of 5 mM hydroquinone in PBS and with or without the presence of irreversibly stuck PMAA on the Au surface at the start of the sweep. Without PMAA on the Au surface, the electrochemical setup of the EQCM-D (Figure 4.13A) gives a peak in the potential around 0.45 V, while for ESPR the equivalent peak potential occurs a bit below 0.4 V. Interestingly, performing the same sweep after adsorbing PMAA to the Au surface (adsorbed previously by applying constant potentials as in Figure 4.12) shifts the peak potential towards lower values in both setups. This suggests the addition of PMAA on the Au surface somehow is lowering the energy barrier for electron transfer in the hydroquinone oxidation reaction (see Figure 4.11), i.e. it is acting like a catalyst.

The irreversibly adsorbed part of PMAA to the Au surface was observed to speed up the initial thickness change upon applying positive potentials. This raised the question whether switching could occur with *only* the PMAA present on the Au surface and no PMAA in solution? Control QCM-D experiments of PMAA behaviour on Au in Figure S5B of the SI of **Paper 3** indicate (from the dissipation response) that the PMAA chains adopts a flatter rigid conformation at low pH and a more swollen extended conformation at neutral to high pH when PMAA gets more charged. Thus, as the swollen surface adsorbed PMAA is protonated and starts to collapse after applying a potential, it could potentially "grab" some PEG chains via hydrogen-bond interactions and partially collapse the brush in the process. This behaviour would greatly depend on the molecular weight of the PMAA, as longer polymer chains would form loops and trains that extend further away from the surface than shorter chains. Indeed, when testing with the smallest PMAA (5.4 kg/mol) we could only observe relatively small dissipation shifts after removing PMAA from solution, even at high applied potentials. However, the response from 74 kg/mol PMAA was slightly higher and for 429 kg/mol the effect was much closer to switching with the same PMAA also in solution. Still, additional ESPR experiments are needed to confirm also the PEG brush changes its properties without PMAA in solution (as would be indicated by changes in exclusion height).

There is an additional use-case for purely surface adsorbed PMAA. In Figure 4.14 the PEG-PMAA interaction of purely surface adsorbed PMAA (429 kg/mol) is utilised as a local pH sensor for the hydroquinone oxidation reaction. Assuming that the dissipation response of the layer is mainly affected by pH (charge interactions should be screened above  $\approx 1$  nm), it should be possible to translate the applied potential to local pH change via the dissipation response of the PEG-PMAA "sensor". Figure 4.14A and B show the dissipation shifts from the same surface when applying five different potentials and five bulk pH injections within the PEG-PMAA layer's dissipation sensitivity window (i.e. the "sensor range"). The linear regression (Figure 4.14C) of the bulk pH and difference in dissipation shifts (here  $\Delta D_{diff} = 0$  corresponds to full extension) can be utilised to translate the difference in dissipation shift from the hydroquinone oxidation tests into local pH change as a function of applied potential within this sensitivity window (see Figure 4.14D). The local pH rate of change with potential increases with higher potentials, which can be explained by the increasing concentration of PMAA monomers at the surface in combination with the catalytic effect of surface adsorbed PMAA the hydroquinone oxidation reaction.

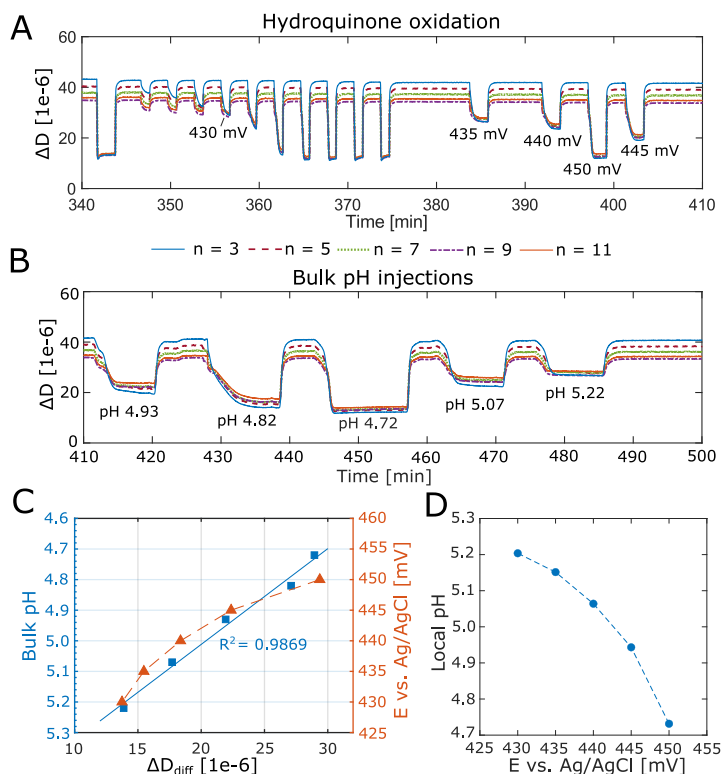


**Figure 4.14:** Utilising the PEG-PMAA interaction and long chains of surface adsorbed PMAA (429 kg/mol) as a local pH sensor by monitoring the dissipation response with EQCM-D to translate hydroquinone oxidation to changes in pH. (A) Measuring dissipation response after applying various potentials. (B) Measuring dissipation response after injecting different bulk pH solutions. (C) Bulk pH and applied potentials from (A) and (B) respectively, as a function of their dissipation responses. The blue line corresponds to the linear regression of bulk pH and dissipation response from (B) only. (D) Local pH as a function of applied potential within the sensitivity window.

Controlling the PEG-PMAA interaction electrochemically has many advantages. The full time evolution from making the decision to switch brush properties to the physical realisation of it can take as little as  $\approx 5$  seconds,

whereas the same action takes minutes by changing bulk solution. Making the pH change more localised is highly beneficial for biomolecule applications, as this minimise environmental changes that effect the biomolecules. Only a PEG brush grafted to the electrode surface will act in a stimuli responsive manner, which means that other surfaces in a nanobiotechnological device can still be coated with PEG brushes and keep their antifouling properties at all times. Such precise spatiotemporal control may provide highly advanced biofunctionality while also keeping the coating process simple, as only a single grafting approach is necessary (see discussion in section 4.3.2). Future work on electrochemical control of the PEG-PMAA system will focus on investigating the effects of different hydroquinone and buffer concentrations. Additionally, more ESPR complimentary measurements and non-interacting height probing of the brush layer while potentials are applied will help in confirming if the brush properties are affected and to what degree.



## CHAPTER 5

---

### Nanobiotechnological devices

---

## 5.1 Plasmonic nanopore arrays

As discussed in section 1, nanopores provide an excellent basis for compartmentalisation of biomolecules in nanoscale volumes, where the biomolecules also can be observed and manipulated. Arrays of nanopores have potential applications as selective biomolecular sieves and filters[112]. To promote further biofunctionality and selectivity, there is an additional advantage to being able to separately functionalise different parts with different types of functional coatings. This would enable filtering against multiple biomolecular properties, like size, hydrophilicity/hydrophobicity and charge[112].

**Paper 4** presents the characterisation and fabrication of nanopore arrays with one or two Au metal films attached to a silicon nitride (SiN) membrane, fabricated with a new electron beam lithography (EBL) fabrication process. Figure 5.1 provide a schematic illustration of the nanostructure and images spanning from the macro scale down to the upper nanoscale. The metal layer provides plasmonic refractometric sensing capabilities that can be accessed via extinction spectroscopy (see section 3.3). Having the centre of the pore's interior fabricated in a material with different surface chemistry compared to its openings provide interesting opportunities to functionalise them separately. This may provide advanced conditional filtering functionality based on multiple environmental stimuli. For example, grafting two different types of stimuli-sensitive polymer brushes, one collapsing at low pH and one collapsing at high temperature, means that the pore opening would only be open to macromolecular translocation when both these conditions apply.

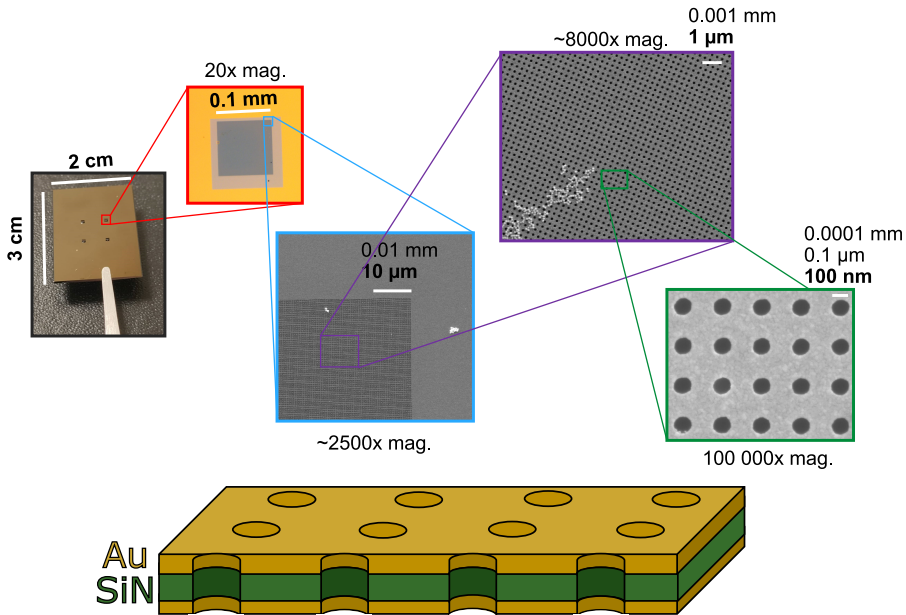


**Figure 5.1:** Schematic of the EBL patterned plasmonic nanopore arrays and illustrating the macro-nano length scale. A sample chip containing four rectangular membranes with arrays of plasmonic nanopores 120 nm in diameter is shown. The first two images are taken with conventional light microscopy while the last three images are taken using a scanning electron microscope.

Figure 5.2 provides an overview of the EBL fabrication process, starting from substrates containing free-standing SiN membranes (the detailed fabrication of which is described elsewhere[113]). Without going into all steps in detail, steps **b** to **e** in Figure 5.2 highlight how a negative resist can be used to eventually define nanoholes on top of a SiN membrane (step **e**) without risking metal contamination on the SiN inside the final nanopore. This approach was not without its challenges, however, since the pillars of resist needed a high aspect ratio (300 nm high and down to 70 nm in diameter) without collapsing during development or after addition of a total of 45 nm deposited metal (see Figure S1 in the supplementary information of **Paper 4**). Careful tuning of the EBL process parameters, in particular finding the right electron dose

was key to success. Later improvements to the adhesion of the hydrophobic resist to the hydrophilic SiN surface were also found to make significant contributions to combat this issue. Essentially, after identifying that the used adhesion promoter (Ti Prime from MicroChemical) in many ways behaved as an organosilane, additional appropriate surface treatment steps were taken. These include: 1) an initial 60 second prior O<sub>2</sub>-plasma treatment at 50 W, 250 mTorr and 80 sccm O<sub>2</sub>(g) to prime the surface with more available Si-OH groups; 2) an additional post-bake step in an oven at 180 ° C for 5 minutes after spinning Ti Prime, to promote siloxane bond formation with the substrate; 3) a final short (10 seconds) O<sub>2</sub>-plasma step before metal deposition, as this was found necessary to avoid metal delamination during RCA cleaning.

While previous work has demonstrated similar plasmonic nanopore arrays fabricated using colloidal lithography[24], a fabrication process with EBL patterning provides clear advantages. EBL allows for largely unrestrained pattern designs and can integrate nanopores with other nanostructure components. Importantly, it opens up the possibility of fabricating single nanopores that can be used for single-molecule trapping with a high degree of spatial control, a concept which would be very impractical using a stochastic patterning process, like colloidal lithography. Future fabrication developments may be able to further elucidate the relationship between resist pillar aspect ratio and maximum allowed deposition thickness before the pillars collapse or lift-off becomes too difficult. This relationship is what determines how many different layers can be included in the interior of the nanopore, which could be interesting to explore further as to provide additional functionality in conditional particle or macromolecular filtering applications.

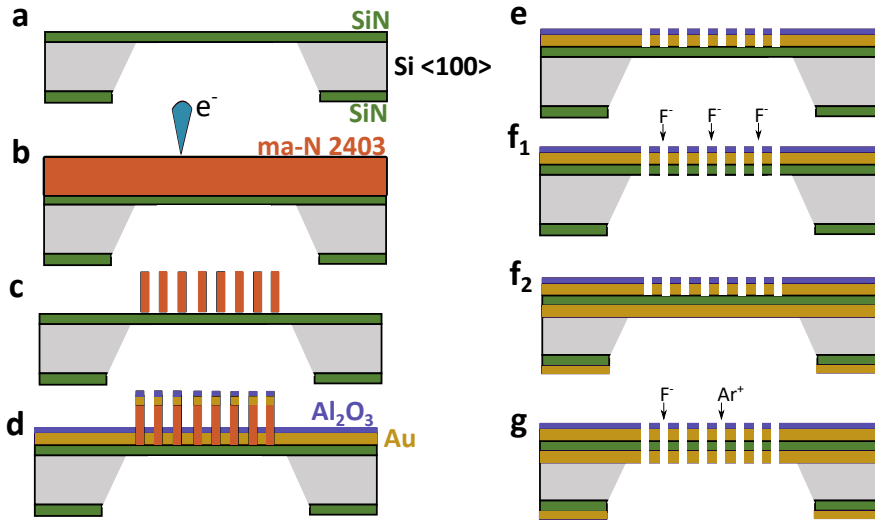


**Figure 5.2:** Fabrication of plasmonic nanopore arrays using EBL. (a) Starting with a thin SiN membrane window in a Si wafer. (b) The surface is primed and coated with negative resist (ma-N 2403), then EBL is used to pattern circles in the resist layer. (c) After development (using developer ma-D 525), non-exposed areas have been dissolved, leaving free-standing cylindrical pillars of crosslinked photoresist. (d) Metal deposition using e-beam physical vapour deposition is performed on top of resist pillars, with an initial adhesion layer of 1-2 nm Cr, followed by 30 nm Au and 15 nm Al<sub>2</sub>O<sub>3</sub>. (e) A lift-off procedure in photoresist remover dissolves the metal-capped pillars, leading to a nanohole array in the deposited films. (f<sub>1</sub>) At this stage, reactive ion etching with CF<sub>4</sub> can be performed to selectively etch the underlying SiN, forming nanopore arrays. (f<sub>2</sub>) Alternatively, a secondary layer of Au can be deposited on the opposite side. (g) Reactive ion etching followed by ion-beam milling with Ar<sup>+</sup> can be used to remove SiN and the secondary Au layer. Reproduced with permission from the author's licentiate thesis work[14].

## 5.2 Functionalisation of nanostructures

The discussion on functional coatings on various surface materials in chapter 4 has exclusively dealt with planar surfaces. For coating nanostructures however, the differing geometries can bring about additional effects that need to be taken into consideration and that may impose certain constraints. For instance, the wettability of a planar surface is less important when being coated, as it can be compensated for by increasing the amount of liquid until the surface is covered. On the other hand, getting liquids through nanoscale openings in a material with poor wettability for the a given liquid can require considerable pressures before overcoming its surface tension[114]. This effect can even be utilised on the microscale to create liquid stop valves in microfluidic systems[115]. It then becomes practically impossible to functionalise the nanostructure past such an opening. The curvature of a surface is also important to consider as an additional effect leading to different behaviour compared to planar surfaces[116], [117]. Thus, it is important to properly evaluate functionalisation procedures and test the functionality of coatings directly in different nanostructures.

### 5.2.1 PEG grafting to nanochannels and nanopores

The approach to grafting dense PEG brushes on  $\text{SiO}_2$  surfaces presented in **Paper 2**, and discussed in more detail in section 4.3.2, was tested directly in two types of nanostructures: nanochannels and a single nanopore.

In collaboration with Sriram Kesarimangalam (affiliations in **Paper 2**), the *in situ* protocol for grafting APS-SMCC-PEG brushes to  $\text{SiO}_2$  (see Figure 4.5) was performed on a microfluidic chip with EBL designed  $\text{SiO}_2$  nanochannels[9] mounted to an inverted epifluorescence microscope. Figure 5.3A shows an overview of the whole microfluidic chip. The nanochannels are connected to two microchannels, that in turn are connected to four liquid reservoirs. Liquid samples can be injected into the reservoirs (each with a capacity of 20  $\mu\text{l}$ ) with a syringe needle. The reservoirs can then be connected to a pressure system that can apply pressurised nitrogen to each reservoir individually. As an example, pressurising only the reservoir labelled  $P_1$  in Figure 5.3 will flow

liquid from  $P_1$  to  $P_2$ . If equal pressure is applied to  $P_1$  and  $P_2$  simultaneously, flow can instead be directed through the nanochannels. During functionalisation with the APS-SMCC-PEG protocol, each solution was loaded and exchanged in both  $P_1$  and  $P_2$ , while only the buffer (10 times diluted PBS) was exchanged in the bottom two reservoirs. During the functionalisation in some initial trials it was noted that pushing liquid through the microchannels became difficult, unless great care was taken to fully replace the APS solution from the reservoirs and channels before loading Sulfo-SMCC. This was likely caused by APS-SMCC precipitation from residual APS in solution phase, which may clog the channels or deposit along the channel walls making them too hydrophobic to let liquid through at the applied pressures. To avoid desorption of APS during extended liquid exchanges with aqueous buffer (curing or heating was not possible as it would ruin the chip or its mounting stage), rinsing with 95 % EtOH followed by purging with nitrogen was performed between the APS and Sulfo-SMCC injection. The issue was not observed again following this change to the *in situ* protocol.

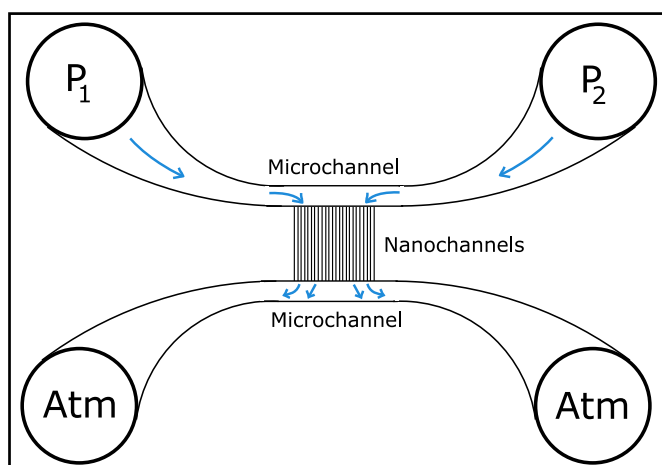


**Figure 5.3:** Overview schematic of the microfluidic chip with nanochannels. The blue arrows indicate how pressure driven flow was directed across the nanochannels during functionalisation.

The antifouling property of the APS-SMCC-PEG (2 kg/mol mPEG-SH) coated chip was evaluated using a fluorescent protein, specifically fluorescein conjugated avidin (Avidin-FITC). Figure 5.4C shows examples of how fluorescence images are taken of the micro- and nanochannel junctions to measure the fluorescence intensity in specified regions around the microchannel and adjacent nanochannels. Clear binding of Avidin-FITC could be detected on the control sample with an initially clean SiO<sub>2</sub> surface since a high fluorescence intensity remained in both the micro- and nanochannels also after rinsing with buffer for 10 minutes. While bulk fluorescence during avidin injection could be observed in the APS-SMCC-PEG coated chip (see Figure S14 in supporting information for **Paper 2**), after rinsing the Avidin-FITC solution with buffer no fluorescence signal could be detected (within a detection limit < 0.1 % of the amount binding in the control). This indicate high protein resistance in both the APS-SMCC-PEG coated micro- and nanochannels.

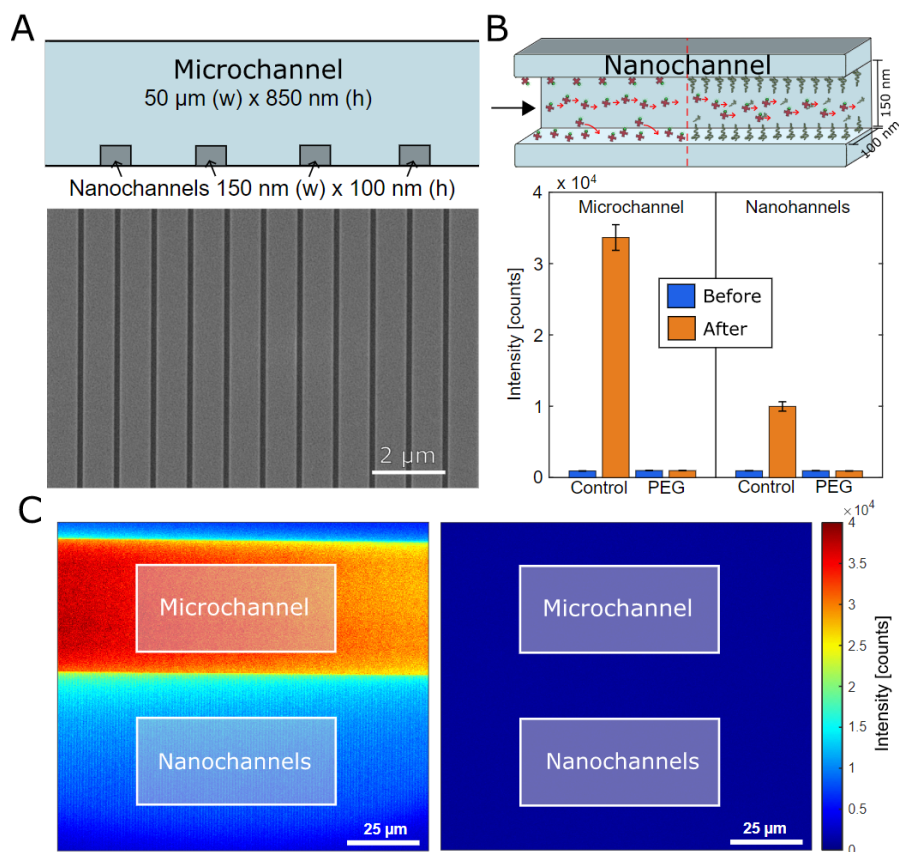


**Figure 5.4:** Investigating the passivation ability of  $\text{SiO}_2$  nanochannels with grafted APS-SMCC-PEG brushes (2 kg/mol mPEG-SH). Avidin-FITC at 0.1 g/L was injected for 20 minutes as a reporter for non-specific protein binding. (A) Schematic of microchannel and nanochannel connections and a SEM image of the nanochannels. (B) After rinsing the Avidin-FITC solution from both channels for 10 minutes with PBS, binding could only be observed to the uncoated control sample for both the top microchannel and nanochannels. (C) Examples of how the fluorescence intensity was measured in the micro- and nanochannels for the control chip (left image) and the APS-SMCC-PEG functionalised chip (right image). Note that the position of the microchannels could always be seen from their faint background fluorescence (not visible in (C) because of the broad intensity scale).

As presented in **Paper 2**, the *in situ* APS-SMCC-PEG approach was also applied to a single nanopore in a free-standing SiN membrane, fabricated using controlled dielectric breakdown[118]. Both the APS-SMCC-PEG functionalisation and characterisation using ion-current measurements were performed by Julia Järlebark (affiliations in **Paper 2**). The SiN membrane is enriched with Si-OH surface groups after oxidation during cleaning in RCA1 (see section 4.1), which allows it to be functionalised with APS. Because continuous liquid exchange is not possible in the flow cell and drying should be avoided to not risk dewetting the pore, the *in situ* protocol was used with an additional ethanol rinsing step between APS and Sulfo-SMCC liquid exchange (APS at 115  $\mu\text{M}$  in 99.4 % EtOH, 0.5 g/L Sulfo-SMCC in 10 times diluted PBS and 1 g/L mPEG-SH 2 kg/mol in 0.9M  $\text{Na}_2\text{SO}_4$ ). Single nanopores are widely used for single molecule sensing using the ion-current measurement technique[11]. When applying a voltage across a non-permeable membrane containing a single nanopore that is immersed in an electrolyte, a current conducting through the nanopore can be detected due to the presence of ions. However, while an object is passing through the nanopore, a drop in the current can be observed since the resistance temporarily increases inside the pore cavity. This way, translocation of objects that occupy a sufficiently large portion of the nanopore cavity can be detected. The conductance of the nanopore can be taken as a direct measurement of the nanopore diameter if its length and the conductivity of the electrolyte is known (see supporting information in **Paper 2**). Figure 5.5 shows a plot of the measured current at different applied potentials of the same nanopore before and after functionalisation with APS-SMCC-PEG. The linear regressions reveal that the conductance of the pore has decreased by a large margin, reducing the effective pore diameter by almost 12 nm. This means a large blockage is present inside the pore, likely due to the presence of APS-SMCC-PEG. However, the same procedure with the larger 20 kg/mol PEG did not reduce the conductance of a similar pore to the same large degree. This indicates that the blockage does not likely come from multilayers of APS-SMCC and that the 20 kg/mol PEG cannot pack as densely in pores of this size.

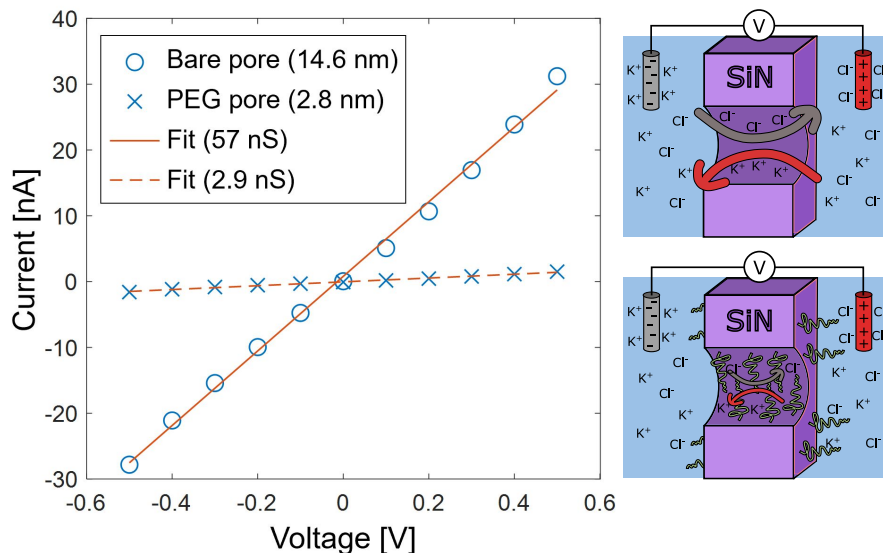


**Figure 5.5:** Conductivity measurements of a single nanopore in SiN before and after functionalisation with the APS-SMCC-PEG (2 kg/mol) in situ protocol. From the linear regression of the current-voltage relationship a reduced conductivity and smaller effective pore diameter can be measured after APS-SMCC-PEG functionalisation.

### 5.2.2 Unpublished work: Macromolecular gating with PEG-PMAA interactions

The observed height change of a protein repelling PEG brush upon interaction with PMAA at low pH (see section 4.4) could potentially be useful as a macromolecular gating mechanism in nanostructures with nanoscale openings. Here this prospect is put to the test, and some preliminary extinction spectroscopy measurements on plasmonic nanowells (see section 3.3) and liquid atomic force microscopy are presented.

A nanowell sample with 80 nm diameter nanoholes through a 30 nm Au metal layer extending roughly 100 nm into an underlying fused silica ( $\text{SiO}_2$ ) sub-

strate[23] was used for this experiment. Figure 5.6 show the resonance shifts for peak and dip for the nanowell samples after 20 kg/mol mPEG-SH brush was grafted in 0.9 M Na<sub>2</sub>SO<sub>4</sub>. The experiment starts in PBS buffer adjusted to pH 4.5 (corresponding to all white regions). A first protein injection of neutravidin at 0.1 g/L in PBS pH 4.5 indicates that no protein binding occurs on the surface or inside the nanowells. Then, a short injection of 0.1 g/L PMAA (5.4 kg/ml) at pH 4.5 leads PMAA binding to the PEG brush. As observed in Figure 1E in **Paper 3**, incremental injections of PMAA should in principle result in a gradual decrease in the exclusion height of the PEG brush. However, at this stage a second neutravidin injection gives no indication of a binding response (there is however some indication that the protein removes a bit of PMAA from the slight decrease in the peak signal). After the third incremental PMAA injection however, the dip's response to injection of neutravidin is suddenly different, where a large amount of protein binding can be observed. At the same time, the response from the peak is mostly unaffected, a scenario which strongly indicates preferential adsorption inside the nanowells, as shown in Figure 3.9B. Injecting PBS at neutral pH rapidly removes the adsorbed PMAA and most of the adsorbed protein, while a final protein injection reveals that the nanowells are indeed closed again without sufficient PMAA present. However, it was not possible to verify in a control experiment if the amount of adsorbed mass at the end of the experiment ( $\approx 1$  nm shift in the dip) corresponds to trapped proteins or PMAA on the surface. Complementary measurements, using for example fluorescence microscopy, are thus needed to confirm whether protein translocation, trapping in solution and SiO<sub>2</sub> adsorption has really occurred.

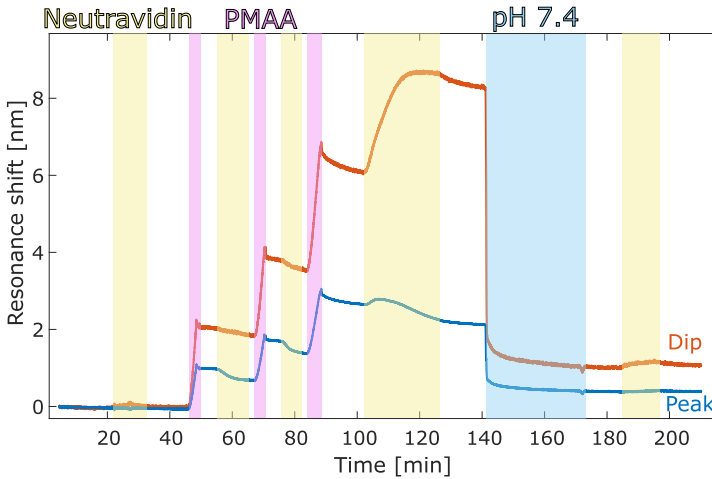


**Figure 5.6:** Macromolecular gating experiment on 80 nm diameter nanowells coated with 20 kg/mol mPEG-SH. White regions corresponds to PBS adjusted to pH 4.5, yellow regions are injections of neutravidin at 0.1 g/L in PBS pH 4.5, pink regions are 5.4 kg/mol PMAA at 0.1 g/L and blue region is normal PBS at pH 7.4. After several incremental injections of PMAA, at the 100 minute mark a large shift in the dip upon injecting neutravidin can be observed, whereas the peak response is low.

Two collaborators, Gustav Ferrand-Drake del Castillo (Chalmers) and Ulrich Ramach (Vienna University of Technology) performed liquid atomic force microscopy measurements of a similar 80 nm diameter nanowell sample coated with 20 kg/mol PEG brushes and subjected to PMAA at low pH. The result is presented in Figure 5.7. The penetration of the AFM tip into the nanowells when the PEG surface was saturated with PMAA at pH 4.5 appears to be deeper in comparison to after PMAA had been rinsed away with PBS pH 7.4. This result further suggests that the PEG brush does not act much as a barrier to a physical probe when it is interacting with PMAA.

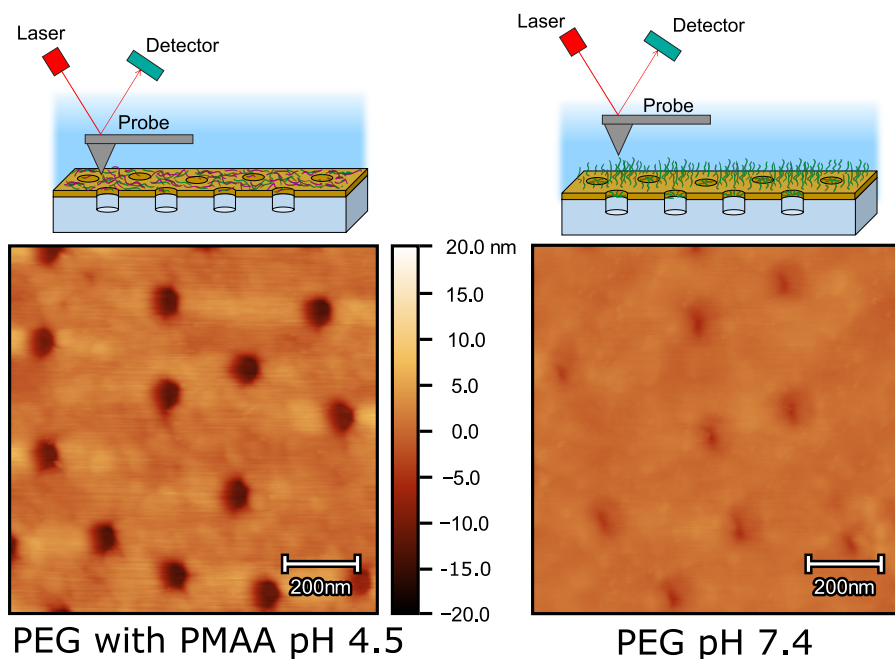


**Figure 5.7:** Liquid atomic force microscopy measurements on 80 nm diameter nanowells coated with PEG brushes. The left measurement corresponds to a PEG-PMAA coating at pH 4.5, and the right measurement is the same sample in PBS pH 7.4 after rinsing away PMAA.

Together, the results presented in Figure 5.6 and 5.7 provide promising indications that the PEG-PMAA interaction can be employed as a mechanism for active macromolecular gating. However, complementary experiments are still needed for verification. Controlling the PEG-PMAA interaction electrochemically (see section 4.5) would also be of great interest for macromolecular gating applications. For instance, it would likely be able to establish more reproducible control of the brush height and faster switching speeds for trapping purposes.

## CHAPTER 6

---

Concluding remarks and future outlook

---

The interdisciplinary field of nanobiotechnology and how it can become useful in advancing our understanding of the complex molecular building blocks of life is becoming increasingly clear. This thesis work has presented new developments in grafting simple, yet effective PEG polymer brushes with high antifouling and biofunctional capabilities on different materials and inside nanostructures.

In **Paper 1** it was found that the surface plasmon resonance phenomenon of thin films of Pd and Pt can be used for sensing purposes in both gaseous and liquid media. Fresnel fitting of a refractometrically sensitive spectral region between the TIR angle and the highly absorbing angles was found to yield quantitative information about adsorbed adlayers in air. In liquid, PEG polymer brushes were grafted to the noble metal surfaces. A solution of proteins injected across the polymer brush coated metals could then be sensed using the broad SPR angle, but proteins were not adsorbed because of the PEG's antifouling property. Using SPR to study chemical modifications of Pd and Pt films can be highly useful when functionalisation of such materials is of interest, such as in organocatalysis, electrochemistry or zero-mode waveguide biosensing.

In **Paper 2** a new grafting-to approach based on coating SiO<sub>2</sub> substrates with PEG brushes possessing biofunctionality is presented. A thorough investigation with surface sensitive techniques concluded that a hydrolytically stable amino-terminated silatrane was well suited as an anchoring group for easy and accessible SiO<sub>2</sub> functionalisation for both open and enclosed systems. The PEG coated SiO<sub>2</sub> surface displayed excellent antifouling ability, could be made highly protein selective by utilising the avidin-biotin interaction and was demonstrated to be fully compatible with both SiO<sub>2</sub> nanochannels and silicon nitride nanopores. Since SiO<sub>2</sub> is a widely used material in many different fields where biomolecules are involved, we believe our simple protocol will be of great benefit for a broad range of applications. Still, as also demonstrated, we emphasise its particular suitability for nanobiotechnological devices.

In **Paper 3** a novel method of making conventional PEG brushes stimuli-responsive was also presented. Introducing PMAA in solution at low pH was found to irreversibly alter the physical properties of a PEG brush grafted on Au at low pH. However, upon increasing the pH of the solution the PMAA

---

desorbed such that the original PEG brush properties were reinstated. These results open the door to new innovative nanobiotechnologies that can be directly applied to many pre-existing PEG technologies.

Unpublished results building upon the work in **Paper 3** were also presented, which showed how the same PEG-PMAA interaction can be controlled electrochemically at neutral solution pH by using a proton donor molecule present in solution. Furthermore, preliminary results where the PEG-PMAA interaction was applied to a plasmonic nanohole array structure suggest the interaction may be used as an active macromolecular gating system for nanostructures.

In **Paper 4** the fabrication of plasmonic nanopore arrays in free-standing membranes using a new electron beam lithography approach was presented. Using a negative resist layer, it is possible to define pillars of high aspect ratio which enable making nanopores with multiple interior materials with distinct boundaries. This opens up the possibility of creating advanced nanobiotechnological pore devices with smart sieving or biofiltering functionality, and paves the way for future single nanopore devices.

Together, these contributions highlight the strength in combining bottom-up self-assembled surface coatings with solid-state nanostructures in providing highly functional nanomaterials for biological applications. In future work, electrochemical control of the PEG-PMAA interaction is of particular interest as a potential active macromolecular gating system that can provide advanced functionality for nanobiotechnological devices. Another future direction involves the nanofabrication of single nanopore reaction chambers using electron beam lithography, where added functional polymer brush barriers can confine single biomolecules within the chamber volume for extended time periods without requiring immobilisation. This would essentially create a "biomolecular living room" where single molecules can be studied at different conditions and in the presence of various molecules that are small enough to pass through the polymer brush barrier. However, it should be recognised that even after obtaining these kinds of nanobiotechnological tools, a substantial amount of work is likely involved in adapting them to the specific needs of a given biomolecular system. Thus, focus should also be put into developing selective coatings to fulfil the needs of the biomolecules by "furnishing the biomolecular living room".



---

## References

---

- [1] G. M. Whitesides, “The right size in nanobiotechnology,” *Nature Biotechnology*, vol. 21, no. 10, pp. 1161–1165, Sep. 2003.
- [2] K. K. Jain, “Nanomedicine: Application of Nanobiotechnology in Medical Practice,” *Medical Principles and Practice*, vol. 17, no. 2, pp. 89–101, Feb. 2008.
- [3] K. K. Jain, “Applications of Nanobiotechnology in Clinical Diagnostics,” *Clinical Chemistry*, vol. 53, no. 11, pp. 2002–2009, Nov. 2007.
- [4] H. Craighead, “Future lab-on-a-chip technologies for interrogating individual molecules,” *Nature*, vol. 442, no. 7101, pp. 387–393, Jul. 2006.
- [5] D. Figeys and D. Pinto, “Lab-on-a-Chip: A Revolution in Biological and Medical Sciences.,” *Analytical Chemistry*, vol. 72, no. 9, May 2000.
- [6] Y. C. Lim, A. Z. Kouzani, and W. Duan, “Lab-on-a-chip: a component view,” *Microsystem Technologies 2010 16:12*, vol. 16, no. 12, pp. 1995–2015, Sep. 2010.
- [7] H. Klefenz, “Nanobiotechnology: From Molecules to Systems,” *Engineering in Life Sciences*, vol. 4, no. 3, pp. 211–218, Jun. 2004.

- [8] M. Feig, I. Yu, P. H. Wang, G. Nawrocki, and Y. Sugita, "Crowding in Cellular Environments at an Atomistic Level from Computer Simulations," *The Journal of Physical Chemistry. B*, vol. 121, no. 34, p. 8009, Aug. 2017.
- [9] F. Persson and J. O. Tegenfeldt, "DNA in nanochannels-directly visualizing genomic information," *Chemical Society Reviews*, vol. 39, no. 3, pp. 985–999, Feb. 2010.
- [10] M. Belkin, S. H. Chao, M. P. Jonsson, C. Dekker, and A. Aksimentiev, "Plasmonic Nanopores for Trapping, Controlling Displacement, and Sequencing of DNA," *ACS Nano*, vol. 9, no. 11, pp. 10 598–10 611, Nov. 2015.
- [11] L. Xue, H. Yamazaki, R. Ren, M. Wanunu, A. P. Ivanov, and J. B. Edel, *Solid-state nanopore sensors*, Dec. 2020.
- [12] J. Prikulis, P. Hanarp, L. Olofsson, D. Sutherland, and M. Käll, "Optical spectroscopy of nanometric holes in thin gold films," *Nano Letters*, vol. 4, no. 6, pp. 1003–1007, Jun. 2004.
- [13] O. M. Eggenberger, C. Ying, and M. Mayer, *Surface coatings for solid-state nanopores*, 2019.
- [14] J. Andersson, *Interpolymer complexation of a polymer brush*, Licentiate thesis. Gothenburg: Chalmers, Nov. 2020, vol. no. 2020:18.
- [15] A. Ulman, "Formation and Structure of Self-Assembled Monolayers," *Chemical Reviews*, vol. 96, no. 4, pp. 1533–1554, 1996.
- [16] R. G. Chapman, E. Ostuni, S. Takayama, R. E. Holmlin, L. Yan, and G. M. Whitesides, "Surveying for surfaces that resist the adsorption of proteins," *Journal of the American Chemical Society*, vol. 122, no. 34, pp. 8303–8304, Aug. 2000.
- [17] E. Ostuni, R. G. Chapman, M. N. Liang, *et al.*, "Self-assembled monolayers that resist the adsorption of proteins and the adhesion of bacterial and mammalian cells," *Langmuir*, vol. 17, no. 20, pp. 6336–6343, Oct. 2001.
- [18] J. T. Heggstad, C. M. Fontes, D. Y. Joh, *et al.*, "In Pursuit of Zero 2.0: Recent Developments in Nonfouling Polymer Brushes for Immunoassays," *Advanced Materials*, vol. 32, no. 2, p. 1903 285, Jan. 2020.

- 
- [19] M. A. Stuart, W. T. Huck, J. Genzer, *et al.*, “Emerging applications of stimuli-responsive polymer materials,” *Nature Materials*, vol. 9, no. 2, pp. 101–113, 2010.
- [20] G. Emilsson, R. L. Schoch, L. Feuz, F. Höök, R. Y. Lim, and A. B. Dahlin, “Strongly stretched protein resistant poly(ethylene glycol) brushes prepared by grafting-to,” *ACS Applied Materials and Interfaces*, vol. 7, no. 14, pp. 7505–7515, 2015.
- [21] G. Emilsson, K. Xiong, Y. Sakiyama, *et al.*, “Polymer brushes in solid-state nanopores form an impenetrable entropic barrier for proteins,” *Nanoscale*, vol. 10, no. 10, pp. 4663–4669, 2018.
- [22] G. Emilsson, Y. Sakiyama, B. Malekian, *et al.*, “Gating Protein Transport in Solid State Nanopores by Single Molecule Recognition,” *ACS Central Science*, 2018.
- [23] B. Malekian, K. Xiong, G. Emilsson, *et al.*, “Fabrication and characterization of plasmonic nanopores with cavities in the solid support,” *Sensors (Switzerland)*, 2017.
- [24] A. B. Dahlin, M. Mapar, K. Xiong, *et al.*, “Plasmonic Nanopores in Metal-Insulator-Metal Films,” *Advanced Optical Materials*, vol. 2, no. 6, pp. 556–564, Jun. 2014.
- [25] M. Rubinstein, R. H. Colby, *et al.*, *Polymer physics*. Oxford university press New York, 2003, vol. 23.
- [26] G. J. Fleer, M. A. C. Stuart, J. M. H. M. Scheutjens, T. Cosgrove, and B. Vincent, *Polymers at Interfaces*, 1. Springer Science & Business Media, 1998, vol. 36, p. 1995.
- [27] R. A. L. Jones, R. A. Jones, R. Jones, *et al.*, *Soft condensed matter*. Oxford University Press, 2002, vol. 6.
- [28] P. De Gennes, “Polymers at an interface; a simplified view,” *Advances in colloid and interface science*, vol. 27, no. 3-4, pp. 189–209, 1987.
- [29] S. T. Milner, “Polymer brushes,” *Science*, vol. 251, no. 4996, pp. 905–914, 1991.
- [30] S. T. Milner, T. A. Witten, and M. E. Cates, “A parabolic density profile for grafted polymers,” *EPL*, vol. 5, no. 5, pp. 413–418, 1988.

- [31] J. O. Zoppe, N. C. Ataman, P. Mocny, J. Wang, J. Moraes, and H. A. Klok, "Surface-Initiated Controlled Radical Polymerization: State-of-the-Art, Opportunities, and Challenges in Surface and Interface Engineering with Polymer Brushes," *Chemical Reviews*, vol. 117, no. 3, pp. 1105–1318, 2017.
- [32] J. S. Suk, Q. Xu, N. Kim, J. Hanes, and L. M. Ensign, "Pegylation as a strategy for improving nanoparticle-based drug and gene delivery," *Advanced drug delivery reviews*, vol. 99, pp. 28–51, 2016.
- [33] U. Wattendorf and H. P. Merkle, "PEGylation as a tool for the biomedical engineering of surface modified microparticles," *Journal of Pharmaceutical Sciences*, vol. 97, no. 11, pp. 4655–4669, Nov. 2008.
- [34] R. E. Holmlin, X. Chen, R. G. Chapman, S. Takayama, and G. M. Whitesides, "Zwitterionic SAMs that resist nonspecific adsorption of protein from aqueous buffer," *Langmuir*, vol. 17, no. 9, pp. 2841–2850, May 2001.
- [35] B. Ensing, A. Tiwari, M. Tros, *et al.*, "On the origin of the extremely different solubilities of polyethers in water," *Nature Communications*, vol. 10, no. 1, pp. 1–8, Dec. 2019.
- [36] L. Nová, F. Uhlík, and P. Košovan, "Local pH and effective pK<sub>A</sub> of weak polyelectrolytes—insights from computer simulations," *Physical Chemistry Chemical Physics*, vol. 19, no. 22, pp. 14376–14387, Jun. 2017.
- [37] R. Arnold, "The titration of polymeric acids," *Journal of Colloid Science*, vol. 12, no. 6, pp. 549–556, Dec. 1957.
- [38] T. N. Nekrasova, Y. V. Anufriyeva, A. M. Yel'yashevich, and O. B. Ptitsyn, "Potentiometric titration of polyacrylic acid, polymethacrylic acid and poly-L-glutamic acid," *Polymer Science U.S.S.R.*, vol. 7, no. 5, pp. 1008–1018, Jan. 1965.
- [39] R. R. Netz and D. Aderlman, "Neutral and charged polymers at interfaces," *Phys. Rep.-Rev. Sec. Phys. Lett*, vol. 380, pp. 1–95, 2003.
- [40] V. V. Khutoryanskiy and G. Staikos, *Hydrogen-bonded interpolymer complexes: formation, structure and applications*. World Scientific, 2009.

- 
- [41] I. Papisov, V. Baranovskii, Y. Sergieva, A. Antipina, and V. Kabanov, "Thermodynamics of complex formation between polymethacrylic and polyacrylic acids and polyethylene glycols. Calculation of temperatures of breakdown of complexes of oligomers and matrices," *Polymer Science U.S.S.R.*, vol. 16, no. 5, pp. 1311–1321, Jan. 1974.
- [42] A. Antipina, V. Baranovskii, I. Papisov, and V. Kabanov, "Equilibrium peculiarities in the complexing of polymeric acids with poly (ethylene glycols)," *Polymer Science U.S.S.R.*, vol. 14, no. 4, pp. 1047–1057, Jan. 1972.
- [43] Y. Osada and M. Sato, "Thermal equilibrium of the intermacromolecular complexes of polycarboxylic acids realized by cooperative hydrogen bonding.," *J Polym Sci Part B Polym Lett*, vol. 14, no. 3, pp. 129–134, Mar. 1976.
- [44] Z. Nurkeeva, G. Mun, V. Khutoryanskiy, A. Zotov, and R. Mangazbaeva, "Interpolymer complexes of poly(vinyl ether) of ethylene glycol with poly(carboxylic acids) in aqueous, alcohol and mixed solutions," *Polymer*, vol. 41, no. 21, pp. 7647–7651, Oct. 2000.
- [45] T. Ikawa, K. Abe, K. Honda, and E. Tsuchida, "Interpolymer complex between poly(ethylene oxide) and poly(carboxylic acid)," *Journal of Polymer Science: Polymer Chemistry Edition*, vol. 13, no. 7, pp. 1505–1514, Jul. 1975.
- [46] R. C. Dougherty, "Temperature and pressure dependence of hydrogen bond strength: A perturbation molecular orbital approach," *The Journal of Chemical Physics*, vol. 109, no. 17, p. 7372, Oct. 1998.
- [47] J. L. Lutkenhaus, K. D. Hrabak, K. McEnnis, and P. T. Hammond, "Elastomeric flexible free-standing hydrogen-bonded nanoscale assemblies," *Journal of the American Chemical Society*, vol. 127, no. 49, pp. 17 228–17 234, Dec. 2005.
- [48] M. Zeghal and L. Auvray, "Structure of polymer complexes in water," *Europhysics Letters*, vol. 45, no. 4, pp. 482–487, Feb. 1999.
- [49] A. J. Bard and L. R. Faulkner, *Electrochemical methods : fundamentals and applications*, Second edition. John Wiley & Sons, Inc., 2001.

- [50] S. M. Oja, Y. Fan, C. M. Armstrong, P. Defnet, and B. Zhang, "Nanoscale Electrochemistry Revisited," *Analytical Chemistry*, vol. 88, no. 1, pp. 414–430, Jan. 2016.
- [51] A. Serrà and J. García-Torres, "Electrochemistry: A basic and powerful tool for micro- and nanomotor fabrication and characterization," *Applied Materials Today*, vol. 22, p. 100939, Mar. 2021.
- [52] F. R. F. Fan, J. Kwak, and A. J. Bard, "Single molecule electrochemistry," *Journal of the American Chemical Society*, vol. 118, no. 40, pp. 9669–9675, Oct. 1996.
- [53] J. Bai, X. Li, Z. Zhu, *et al.*, "Single-Molecule Electrochemical Transistors," *Advanced Materials*, vol. 33, no. 50, p. 2005883, Dec. 2021.
- [54] A. B. Dahlin, B. Dielacher, P. Rajendran, *et al.*, "Electrochemical plasmonic sensors," *Analytical and Bioanalytical Chemistry* 2011 402:5, vol. 402, no. 5, pp. 1773–1784, Sep. 2011.
- [55] M. Welch, A. Rastogi, and C. Ober, "Polymer brushes for electrochemical biosensors," *Soft Matter*, vol. 7, no. 2, pp. 297–302, Jan. 2011.
- [56] N. Fomina, C. A. Johnson, A. Maruniak, *et al.*, "An electrochemical platform for localized pH control on demand," *Lab on a Chip*, vol. 16, no. 12, pp. 2236–2244, Jun. 2016.
- [57] G. F. D. del Castillo, M. Kyriakidou, Z. Adali, K. Xiong, R. L. Hailes, and A. Dahlin, "Electrically Switchable Polymer Brushes for Protein Capture and Release in Biological Environments," *Angewandte Chemie International Edition*, vol. 61, no. 22, e202115745, May 2022.
- [58] H. Raether, *Surface Plasmons on Smooth and Rough Surfaces and on Gratings*. Springer, 1988, vol. 111.
- [59] B. Liedberg, C. Nylander, and I. Lunström, "Surface plasmon resonance for gas detection and biosensing," *Sensors and Actuators*, vol. 4, pp. 299–304, Jan. 1983.
- [60] A. B. Dahlin, *Plasmonic Biosensors - An Integrated View of Refractive Index Detection*. IOS Press BV, 2012, vol. 4.
- [61] L. S. Jung, C. T. Campbell, T. M. Chinowsky, M. N. Mar, and S. S. Yee, "Quantitative Interpretation of the Response of Surface Plasmon Resonance Sensors to Adsorbed Films," *Langmuir*, vol. 14, no. 19, pp. 5636–5648, 1998.

- 
- [62] J. Svirelis, J. Andersson, A. Stradner, and A. Dahlin, “Accurate Correction of the Bulk Response in Surface Plasmon Resonance Sensing Provides New Insights on Interactions Involving Lysozyme and Poly(ethylene glycol),” *ACS Sensors*, vol. 7, no. 4, pp. 1175–1182, Mar. 2022.
- [63] J. Vörös, “The Density and Refractive Index of Adsorbing Protein Layers,” *Biophysical Journal*, vol. 87, no. 1, pp. 553–561, Jul. 2004.
- [64] R. L. Schoch and R. Y. H. Lim, “Non-Interacting Molecules as Innate Structural Probes in Surface Plasmon Resonance,” *Langmuir*, vol. 29, no. 12, pp. 4068–4076, Mar. 2013.
- [65] I. Reviakine, D. Johannsmann, and R. P. Richter, “Hearing what you cannot see and visualizing what you hear: Interpreting quartz crystal microbalance data from solvated interfaces,” *Analytical Chemistry*, vol. 83, no. 23, pp. 8838–8848, Dec. 2011.
- [66] M. Rodahl, F. Höök, A. Krozer, P. Brzezinski, and B. Kasemo, “Quartz crystal microbalance setup for frequency and Q-factor measurements in gaseous and liquid environments,” *Review of Scientific Instruments*, vol. 66, no. 7, pp. 3924–3930, Jul. 1995.
- [67] G. Sauerbrey, “Use of quartz vibration for weighing thin films on a microbalance,” *Physik J*, 1959.
- [68] M. Rodahl and B. Kasemo, “Frequency and dissipation-factor responses to localized liquid deposits on a QCM electrode,” *Sensors and Actuators, B: Chemical*, vol. 37, no. 1-2, pp. 111–116, Nov. 1996.
- [69] M. V. Voinova, M. Rodahl, M. Jonson, and B. Kasemo, “Viscoelastic Acoustic Response of Layered Polymer Films at Fluid-Solid Interfaces: Continuum Mechanics Approach,” *Physica Scripta*, vol. 59, no. 5, pp. 391–396, May 1999.
- [70] F. Höök, B. Kasemo, T. Nylander, C. Fant, K. Sott, and H. Elwing, “Variations in coupled water, viscoelastic properties, and film thickness of a Mefp-1 protein film during adsorption and cross-linking: A quartz crystal microbalance with dissipation monitoring, ellipsometry, and surface plasmon resonance study,” *Analytical Chemistry*, vol. 73, no. 24, pp. 5796–5804, Dec. 2001.

- [71] G. Dunér, E. Thormann, and A. Dedinaite, “Quartz Crystal Microbalance with Dissipation (QCM-D) studies of the viscoelastic response from a continuously growing grafted polyelectrolyte layer,” *Journal of Colloid and Interface Science*, vol. 408, no. 1, pp. 229–234, Oct. 2013.
- [72] S. Szunerits and R. Boukherroub, “Sensing using localised surface plasmon resonance sensors,” *Chemical Communications*, vol. 48, no. 72, pp. 8999–9010, Aug. 2012.
- [73] P. Hanarp, M. Käll, and D. S. Sutherland, “Optical properties of short range ordered arrays of nanometer gold disks prepared by colloidal lithography,” *Journal of Physical Chemistry B*, vol. 107, no. 24, pp. 5768–5772, Jun. 2003.
- [74] T. W. Ebbesen, H. J. Lezec, H. F. Ghaemi, T. Thio, and P. A. Wolff, “Extraordinary optical transmission through sub-wavelength hole arrays,” *Nature* 1998 391:6668, vol. 391, no. 6668, pp. 667–669, Feb. 1998.
- [75] J. Junesch, G. Emilsson, K. Xiong, *et al.*, “Location-specific nanoplasmonic sensing of biomolecular binding to lipid membranes with negative curvature,” *Nanoscale*, vol. 7, no. 37, pp. 15 080–15 085, Sep. 2015.
- [76] M. P. Jonsson, A. B. Dahlin, L. Feuz, S. Petronis, and F. Höök, “Locally functionalized short-range ordered nanoplasmonic pores for bioanalytical sensing,” *Analytical Chemistry*, vol. 82, no. 5, pp. 2087–2094, Mar. 2010.
- [77] T. Sannomiya, O. Scholder, K. Jefimovs, C. Hafner, and A. B. Dahlin, “Investigation of plasmon resonances in metal films with nanohole arrays for biosensing applications,” *Small*, vol. 7, no. 12, pp. 1653–1663, Jun. 2011.
- [78] V. Bochenkov, M. Frederiksen, and D. Sutherland, “Enhanced refractive index sensitivity of elevated short-range ordered nanohole arrays in optically thin plasmonic Au films,” *Optics Express*, Vol. 21, Issue 12, pp. 14763–14770, vol. 21, no. 12, pp. 14763–14770, Jun. 2013.
- [79] M. Schwind, B. Kasemo, and I. Zorić, “Localized and propagating plasmons in metal films with nanoholes,” *Nano Letters*, vol. 13, no. 4, pp. 1743–1750, Apr. 2013.

- 
- [80] A. B. Dahlin, J. O. Tegenfeldt, and F. Hook, “Improving the instrumental resolution of sensors based on localized surface plasmon resonance,” *Analytical Chemistry*, vol. 78, no. 13, pp. 4416–4423, Jul. 2006.
- [81] G. Emilsson, E. Röder, B. Malekian, *et al.*, “Nanoplasmonic sensor detects preferential binding of IRSp53 to negative membrane curvature,” *Frontiers in Chemistry*, vol. 7, no. FEB, p. 1, 2019.
- [82] A. Dahlin, “Biochemical Sensing with Nanoplasmonic Architectures: We Know How but Do We Know Why?,” vol. 14, pp. 281–297, Jul. 2021.
- [83] R. Marie, A. B. Dahlin, J. O. Tegenfeldt, and F. Höök, “Generic surface modification strategy for sensing applications based on Au/SiO<sub>2</sub> nanostructures,” *Biointerfaces*, vol. 2, no. 1, pp. 49–55, Mar. 2007.
- [84] K. Xiong, G. Emilsson, and A. B. Dahlin, “Biosensing using plasmonic nanohole arrays with small, homogenous and tunable aperture diameters,” *Analyst*, vol. 141, no. 12, pp. 3803–3810, 2016.
- [85] A. B. Dahlin, S. Chen, M. P. Jonsson, L. Gunnarsson, M. Käll, and F. Höök, “High-resolution microspectroscopy of plasmonic nanostructures for miniaturized biosensing,” *Analytical Chemistry*, vol. 81, no. 16, pp. 6572–6580, Aug. 2009.
- [86] N. Klughammer and C. Dekker, “Palladium zero-mode waveguides for optical single-molecule detection with nanopores,” *Nanotechnology*, vol. 32, no. 18, Apr. 2021.
- [87] E. O. Machiste, L. Segale, S. Conti, *et al.*, “Effect of UV light exposure on hydrophilic polymers used as drug release modulators in solid dosage forms,” *Journal of Drug Delivery Science and Technology*, vol. 15, no. 2, pp. 151–157, Mar. 2005.
- [88] H. Kaczmarek, L. Lindén, and J. F. Rabek, “Reactions of hydroxyl (HO) and hydroperoxyl (HO) radicals generated chemically and photochemically with poly(ethylene oxide),” *Journal of Polymer Science Part A: Polymer Chemistry*, vol. 33, no. 6, pp. 879–890, Apr. 1995.
- [89] G. Jerkiewicz, “Applicability of Platinum as a Counter-Electrode Material in Electrocatalysis Research,” *ACS Catalysis*, vol. 12, no. 4, pp. 2661–2670, Feb. 2022.

- [90] C. C. Johansson Seechurn, M. O. Kitching, T. J. Colacot, and V. Snieckus, "Palladium-Catalyzed Cross-Coupling: A Historical Contextual Perspective to the 2010 Nobel Prize," *Angewandte Chemie International Edition*, vol. 51, no. 21, pp. 5062–5085, May 2012.
- [91] J. W. Sadowski, J. Lekkala, and I. Vikholm, "Biosensors based on surface plasmons excited in non-noble metals," *Biosensors and Bioelectronics*, vol. 6, no. 5, pp. 439–444, Jan. 1991.
- [92] D. Fine, A. Grattoni, R. Goodall, *et al.*, "Silicon Micro- and Nanofabrication for Medicine," *Advanced Healthcare Materials*, vol. 2, no. 5, pp. 632–666, May 2013.
- [93] T.-J. Lee, L.-K. Chau, and C.-J. Huang, "Controlled Silanization: High Molecular Regularity of Functional Thiol Groups on Siloxane Coatings," *Langmuir*, acs.langmuir.0c00745, May 2020.
- [94] C. J. Huang and Y. Y. Zheng, "Controlled Silanization Using Functional Silatrane for Thin and Homogeneous Antifouling Coatings," *Langmuir*, vol. 35, no. 5, pp. 1662–1671, Feb. 2019.
- [95] K. W. Huang, C. W. Hsieh, H. C. Kan, *et al.*, "Improved performance of aminopropylsilatrane over aminopropyltriethoxysilane as a linker for nanoparticle-based plasmon resonance sensors," *Sensors and Actuators, B: Chemical*, vol. 163, no. 1, pp. 207–215, Mar. 2012.
- [96] S. Hsieh, W. J. Chao, and C. W. Hsieh, "Improved performance of aminopropylsilatrane over aminopropyltriethoxysilane as an adhesive film for anchoring gold nanoparticles on silicon surfaces," *Journal of Nanoscience and Nanotechnology*, vol. 9, no. 5, pp. 2894–2901, May 2009.
- [97] N.-P. Huang, R. Michel, J. Voros, *et al.*, "Poly (l-lysine)-g-poly (ethylene glycol) layers on metal oxide surfaces: Surface-analytical characterization and resistance to serum and fibrinogen adsorption," *Langmuir*, vol. 17, no. 2, pp. 489–498, 2001.
- [98] G. L. Kenausis, J. Vörös, D. L. Elbert, *et al.*, "Poly(L-lysine)-g-poly(ethylene glycol) layers on metal oxide surfaces: Attachment mechanism and effects of polymer architecture on resistance to protein adsorption," *Journal of Physical Chemistry B*, vol. 104, no. 14, pp. 3298–3309, Apr. 2000.

- 
- [99] S. Weydert, S. Zürcher, S. Tanner, *et al.*, “Easy to Apply Polyoxazoline-Based Coating for Precise and Long-Term Control of Neural Patterns,” *Langmuir*, vol. 33, no. 35, pp. 8594–8605, Sep. 2017.
- [100] J. A. Howarter and J. P. Youngblood, “Optimization of silica silanization by 3-aminopropyltriethoxysilane,” *Langmuir*, vol. 22, no. 26, pp. 11 142–11 147, 2006.
- [101] M. G. Voronkov, V. M. Dyakov, and S. V. Kirpichenko, “Silatranes,” *Journal of Organometallic Chemistry*, vol. 233, no. 1, pp. 1–147, Jul. 1982.
- [102] M. Zhu, M. Z. Lerum, and W. Chen, “How to prepare reproducible, homogeneous, and hydrolytically stable aminosilane-derived layers on silica,” *Langmuir*, vol. 28, no. 1, pp. 416–423, 2012.
- [103] W. H. Chen, Y. T. Tseng, S. Hsieh, *et al.*, “Silanization of solid surfaces via mercaptopropylsilatrane: A new approach of constructing gold colloid monolayers,” *RSC Advances*, vol. 4, no. 87, pp. 46 527–46 535, Sep. 2014.
- [104] L. S. Shlyakhtenko, A. A. Gall, A. Filonov, Z. Cerovac, A. Lushnikov, and Y. L. Lyubchenko, “Silatrane-based surface chemistry for immobilization of DNA, protein-DNA complexes and other biological materials,” *Ultramicroscopy*, vol. 97, no. 1-4, pp. 279–287, Oct. 2003.
- [105] M. Morpurgo, E. A. Bayer, and M. Wilchek, “N-hydroxysuccinimide carbonates and carbamates are useful reactive reagents for coupling ligands to lysines on proteins,” *Journal of Biochemical and Biophysical Methods*, vol. 38, no. 1, pp. 17–28, Jan. 1999.
- [106] M. Wilchek and E. A. Bayer, “Introduction to avidin-biotin technology,” *Methods in Enzymology*, vol. 184, no. C, pp. 5–13, Jan. 1990.
- [107] N. P. Huang, J. Vörös, S. M. De Paul, M. Textor, and N. D. Spencer, “Biotin-derivatized poly(L-lysine)-g-poly(ethylene glycol): A novel polymeric interface for bioaffinity sensing,” *Langmuir*, vol. 18, no. 1, pp. 220–230, Jan. 2002.
- [108] A. T. Marttila, O. H. Laitinen, K. J. Airene, *et al.*, “Recombinant Neutralite Avidin: A non-glycosylated, acidic mutant of chicken avidin that exhibits high affinity for biotin and low non-specific binding properties,” *FEBS Letters*, vol. 467, no. 1, pp. 31–36, Feb. 2000.

- [109] M. Grdeń, M. Łukaszewski, G. Jerkiewicz, and A. Czerwiński, “Electrochemical behaviour of palladium electrode: Oxidation, electrodis-solution and ionic adsorption,” *Electrochimica Acta*, vol. 53, no. 26, pp. 7583–7598, Nov. 2008.
- [110] I. Sterin, A. Tverdokhlebova, E. Katz, *et al.*, “Multiple pH waves generated electrochemically and propagated from an electrode surface,” *Chemical Communications*, vol. 58, no. 75, pp. 10 516–10 519, Sep. 2022.
- [111] P. Bollella, A. Melman, and E. Katz, “Operando Local pH Mapping of Electrochemical and Bioelectrochemical Reactions Occurring at an Electrode Surface: Effect of the Buffer Concentration,” *ChemElectroChem*, vol. 8, no. 20, pp. 3923–3935, Oct. 2021.
- [112] J. Fu, P. Mao, and J. Han, “Artificial molecular sieves and filters: a new paradigm for biomolecule separation,” *Trends in Biotechnology*, vol. 26, no. 6, pp. 311–320, Jun. 2008.
- [113] A. W. Grant, Q.-H. Hu, and B. Kasemo, “Transmission electron microscopy windows for nanofabricated structures,” *Nanotechnology*, vol. 15, no. 9, pp. 1175–1181, Sep. 2004.
- [114] M. R. Powell, L. Cleary, M. Davenport, K. J. Shea, and Z. S. Siwy, “Electric-field-induced wetting and dewetting in single hydrophobic nanopores,” *Nature Nanotechnology 2011 6:12*, vol. 6, no. 12, pp. 798–802, Oct. 2011.
- [115] S. Wang, X. Zhang, C. Ma, S. Yan, D. Inglis, and S. Feng, “A Review of Capillary Pressure Control Valves in Microfluidics,” *Biosensors 2021, Vol. 11, Page 405*, vol. 11, no. 10, p. 405, Oct. 2021.
- [116] M. Tagliacuzzi, O. Azzaroni, and I. Szleifer, “Responsive polymers end-tethered in solid-state nanochannels: When nanoconfinement really matters,” *Journal of the American Chemical Society*, vol. 132, no. 35, pp. 12 404–12 411, Sep. 2010.
- [117] C. Wijmans and E. B. Zhulina, “Polymer brushes at curved surfaces,” *Macromolecules*, vol. 26, no. 26, pp. 7214–7224, 1993.
- [118] H. Kwok, K. Briggs, and V. Tabard-Cossa, “Nanopore fabrication by controlled dielectric breakdown,” *PLoS ONE*, vol. 9, no. 3, Mar. 2014.